EXPERIMENTAL INVESTIGATIONS OF ELECTROSPRAY IONIZATION VIA HYDRATED LIKE-CHARGED ION PAIRS AND THE SOLUTION TO THE GAS-PHASE STRUCTURAL TRANSITION AND PROTON TRANSFER OF 4-AMINOBENZOIC ACID

A Dissertation

by

MICHAEL JAMES HEBERT

Submitted to the Office of Graduate and Professional Studies of
Texas A&M University
in partial fulfillment of the requirements for the degree of

DOCTOR OF PHILOSOPHY

Chair of Committee,	David H. Russell
Committee Members,	Simon W. North
	Arthur D. Laganowsky
	Paul D. Straight
Head of Department,	Simon W. North

August 2020

Major Subject: Chemistry

ABSTRACT

The ability to retain and observe solution-phase structures using the gas-phase ion mobility (IM) technique is paradoxical. Although many studies have shown kinetic trapping during electrospray ionization (ESI) can allow IM to observe solution-phase structures, *i.e.* "native" ion mobility-mass spectrometry (IM-MS), there remain many uncertainties as to for how long and to what extent solution-phase structures are retained. Cryogenic IM-MS (cryo-IM-MS) is used to investigate structural characteristics of electrosprayed ions here. The advantage offered by the cryogenic drift cell is the rapid thermalization of "freeze-dried" ions (~130 K) to the ~80 K drift cell temperatures, preserving kinetically trapped solution-phase structures and extensively hydrated ions *i.e.* $[M + xH]^{x+}(H_2O)_n$. With n approaching up to several hundred, cryo-IM-MS offers a unique experimental approach to survey the interactions of water and the late-stages of ESI.

The preservation of an unusual like-charged ion pair interaction between guanidinium ions, which has been observed in protein-protein interactions, is investigated. Charge solvation is imperative for stabilizing these like-charged ion pairs, and without sufficient water molecule adducts bridging between the ions, the like-charged ions repel and break apart. A second like-charged interaction was also isolated, where a proton was stabilized within a hydrated guanidinium cluster. These studies are extended to the peptide bradykinin, which has two arginine residues, and showcases similar charging behavior;

extensive hydration of BK permits an additional charge to be stabilized within the solvated clusters.

A late-stage ESI proton transfer event in dehydrating 4-aminobenzoic acid ions is investigated. Molecular dynamics simulations (MDS) are used to calibrate a theoretical collisional cross section (CCS) with the experimental arrival time distributions (ATD) of sequential water clusters. The structures generated indicate that a proton transfer occurs via a water wire at n = 6, *i.e.* via a Grotthuss mechanism. The structural characterizations provided by the addition of CCS to cryo-IM-MS allow for identification of larger structural families up to ~500 Daltons.

DEDICATION

For all those who tirelessly lead their students, that I may soon replicate your success.

Ms. Vicki Hermsdorf

Mr. Garret "V" Vandenbelt

Ms. Cheryl Glocksien

Mr. Kerry Rock

Ms. Wilma Mysak

Ms. Carribeth Bliem

Dr. Lisa "Mouse" Perez

Dr. Simon North

Dr. Matt Lockett

Dr. Domenic Tiani

Dr. John Papanikolas

Dr. Leslie Hicks

Dr. David Russell

ACKNOWLEDGEMENTS

I thank my graduate research advisor, Professor David H. Russell, who provided guidance, enthusiasm, and inspiration particularly when the instrument did not. The entire Russell Research Group has provided technical and emotional support that was critical to success. In particular, Dr. Michael Poltash made me an expert in electronics and instrumentation, and Dr. Kelly Servage taught me the inner workings of the cryogenic ion mobility-mass spectrometer. Lastly, Dr. Nicole Wagner shared with me an exceptional mastery of ion mobility-mass spectrometry.

I thank my committee members, Professor Simon North, Professor Arthur Laganowsky, and Professor Paul Straight for their time and effort in serving on my committee.

I thank Will Seward of the Texas A&M Machine shop, who helped preserve the integrity of the instrument and provided considerable guidance on machining. I am especially grateful for Dr. Lisa Perez and the Laboratory for Molecular Simulations, who provided an amazing amount of guidance and patience with molecular simulations.

I am grateful for the funding provided by the National Science Foundation-Chemistry program (CHE-1707675).

Finally, I thank my friends and family who have supported me throughout the years.

CONTRIBUTORS AND FUNDING SOURCES

Contributors

This work was supervised by a dissertation committee consisting of Professor David H. Russell (advisor), Professor Simon W. North, and Professor Arthur D. Laganowksy of the Department of Chemistry, and Professor Paul D. Straight of the Department of Biochemistry and Biophysics.

Born—Oppenheimer molecular dynamics simulations were performed on $GdmH^+$-$H^+(H_2O)_{18}$ and $GdmH^+$-$Na^+(H_2O)_{18}$ and a molecular dynamics simulation of a hydrated nanodroplet of ~400 water molecules with two guanidinium ions was performed by Victor Kwan at the University of Western Ontario. All other work conducted for this dissertation was completed by the student independently.

Funding Sources

This work was also made possible in part by the National Science Foundation under grant number CHE-1707675. Its contents are solely the responsibility of the authors and do not necessarily represent the official views of the National Science Foundation.

NOMENCLATURE

AAD	acceptor acceptor donor (referring to hydrogen bonding)
ACN	acetonitrile
ATD	arrival time distribution
BK	bradykinin
CCS	collision cross section
CID	collision induced dissociation
CRM	Charge Residue Model
Cryo-IM-MS	cryogenic ion mobility-mass spectrometry
DC IG	direct current ion guide
e	elementary charge (1.602×10^{-19} Coulombs)
E	applied electric field
E/N	field strength in townsend units
ESI	electrospray ionization
GS	gramicidin S
H-bond	hydrogen bond
IEM	Ion Evaporation Model
IM	Ion Mobility
IMS	Ion Mobility Spectrometry
IM-MS	Ion Mobility-Mass Spectrometry
IR	Infrared Spectroscopy
K	ion mobility parameter

K_0	reduced mobility coefficient
k_B	Boltzmann constant
L	drift tube length
MALDI	Matrix-Assisted Laser Desorption Ionization
MCMM	Monte Carlo Multiple Minimum
MCP	Microchannel Plate
MDS	Molecular Dynamics Simulations
MOBCAL	Mobility Calculator
MS	Mass Spectrometry
m/z	mass-to-charge ratio
N	buffer gas number density
NMR	Nuclear Magnetic Resonance
P	buffer gas pressure
PF IF	periodic focusing ion funnel
QM	quantum mechanics
T	buffer gas temperature
t_d	ion drift time inside the drift tube
t_0	ion drift time outside the drift tube
TOF	time-of-flight (mass spectrometer)
TWIMS	Traveling Wave Ion Mobility Spectrometry
μ	reduced mass of ion-neutral pair
V	voltage

v_d	average drift velocity
z	ion charge state
Ω	collision cross section

TABLE OF CONTENTS

Page

ABSTRACT ii

DEDICATION iv

ACKNOWLEDGEMENTS v

CONTRIBUTORS AND FUNDING SOURCES vi

NOMENCLATURE vii

TABLE OF CONTENTS x

LIST OF FIGURES xii

LIST OF TABLES xviii

1. INTRODUCTION: ION MOBILITY AND MASS SPECTROMETRY 1

1.1. Ion Mobility Spectrometry 1
1.2. Ion Mobility-Mass Spectrometry 3
1.2.1. Electrospray Ionization 5
1.3. Cryogenic Ion Mobility-Mass Spectrometry 7
1.3.1. Instrumentation and Design 7
1.3.2. A Novel Way to Study Water Adduction 11
1.3.3. Protonated Water Clusters: $H^+(H_2O)_n$ 14
1.3.4. Hydration of Polar Molecules 17
1.4. Thesis Structure 20

2. HYDRATION OF GUANIDINIUM IONS: AN EXPERIMENTAL SEARCH FOR LIKE-CHARGED ION PAIRS 22

2.1. Background 22
2.2. Methods 25
2.2.1. Experimental 25
2.2.2. Computational 25
2.3. Results and discussion 26
2.3.1. Hydration of Guanidinium Ions 26
2.3.2. Cryo-IM-MS of Doubly Charged Clusters 32

2.3.3. Stabilizing Interactions of Doubly Charged Droplets 36
2.3.4. Multiply Charged Water Clusters in Larger Peptide Systems 40
2.4. Conclusions 41

3. ACCESSING COLLISSION CROSS SECTION ON THE CRYO-IM-MS TO TRACK THE SOLUTION TO GAS-PHASE STRUCTURAL EVOLUTION OF 4-AMINOBENZOIC ACID 45

3.1. Background 45
3.2. Methods 47
3.2.1. Experimental 47
3.2.2. Computational 47
3.2.3. CCS Calibration in Helium 48
3.3. Results and Discussion 50
3.3.1. Hydration of $ABAH^+$ 50
3.3.2. Effects of Solution and Source Conditions 54
3.3.3. Effect of N_2 Drift Gas 57
3.3.4. Cryogenic Collisional Cross Section Calibration 58
3.4. Conclusions 63

4. HYDRATION OF AMMONIUM IONS: WATER STRUCTURES FLUCTUATE BASED ON THE POLAR ENVIRONMENT 66

4.1. Background 66
4.2. Methods 67
4.2.1. Experimental 67
4.2.2. Computational 68
4.3. Results and Discussion 68
4.3.1. Comparison of Hydrated Ammonium-Containing Molecule Structures 68
4.3.2. Collisional Cross Section of the 4-$ABAH^+$ Magic Number Cluster 70
4.3.3. Hydration Dynamics of Dehydrating Droplets 72
4.4. Conclusions 73

5. FUTURE DIRECTIONS, SUMMARY, AND OUTLOOK 75

5.1. Increasing Mass Resolution and IM Duty Cycle 75
5.2. Charge Carrier Effects on ESI 83
5.3. Osmolyte Effects on Peptide/Protein Structure 85
5.4. Hydration of Insulin 89
5.5. Project Summary and Outlook 94

REFERENCES 96

LIST OF FIGURES

Page

Figure 1.1. A model of the mobility experiment, showing separation based on molecule size (green/orange) and charge (red/orange). The green ion has the highest mobility, K, and the fastest arrival time. 1

Figure 1.2. Droplets undergo many coulombic fission and evaporation events prior to reaching a ~10 nm diameter, where either the (a) charged residue model or (b) ion evaporation model likely become operative. The red circle represents the analyte in a droplet. 5

Figure 1.3. An overview of the cryo-IM-MS instrument. Hydrated ions generated in the source region are "freeze-dried" and kept cool within the cryogenically cooled (~80 K) drift cell. Ions are then transferred to the ToF source repeller plate and "pushed" to the ToF for mass analysis. 7

Figure 1.4. An expanded view of the source region. Each label is color coded to a section of the instrument. There are is an additional, unlabeled ring electrode after the DC Ion Guide and before the Gate. This lens is segmented into four quadrants and used as a deflector lens to guide the ions to the IM drift cell aperture. 9

Figure 1.5. Mass spectra of protonated water clusters at (a) variable heated capillary temperatures and (b) variable IM field strengths. The field strength in (a) is 9.12 V/cm and the heated capillary temperature in (b) is 340 K. Adapted with permission from ref. 60. Copyright 2013 American Chemical Society. .. 14

Figure 1.6. Mass-selected ATD for $H^+(H_2O)_n$ (n = 6); peak fitting was performed using Origin 7.5 software. The faster conformer population shown in red corresponds to Eigen (H_3O^+-centered) structures, while the population falling at longer drift times shown in blue is attributed to the Zundel ($H_5O_2^+$-centered) structures solvated by four water monomers. Structures shown are schematic representations of the two lowest energy isomers for the $H^+(H_2O)_n$ (n = 6) cluster determined by Jiang et al. via ab initio calculations.[76] Reprinted with permissions from ref. 91. Copyright 2014 American Chemical Society. 16

Figure 1.7. ATD vs m/z plot for $H^+(H_2O)_n$ (n = 15 to 35) produced at an electric field of (a) 9.1 V cm^{-1} and (b) 15.1 V cm^{-1} in the drift tube at a heated capillary temperature of 340 K. Panels c–e contain the mass-selected ATDs for (n = 20 to 22) at 9.1 V cm^{-1}. The black line is the result of boxcar averaging of the data points (gray ■). The vertical dashed line was inserted to guide the

eye across the centroid of the IM-MS trendlines shown. Reprinted with permissions from ref. 60. Copyright 2013 American Chemical Society.....17

Figure 1.8. ATD vs m/z plot of substance P detailing the conversion of a hydrated conformation, A, to an extended gas-phase conformation, labelled B. The conversion occurs after near complete dehydration. 19

Figure 1.9. ATD vs m/z plot of 10 μM ubiquitin in 0.1% formic acid (FA) and heated capillary temperature of 363 K. Note the monomer is observed without significant hydration. Adapted with permission from ref. 101. Copyright 2015 American Chemical Society. 20

Figure 2.1. Blown up view of an evaporating droplet at 350 K containing 408 water molecules and two guanidinium ions, separated by ~3.5 Å. These ions separate and approach several times throughout the ~200 ns simulation.....24

Figure 2.2. ATD vs m/z plots of (a) $GdmH^+(H_2O)_n$, (b) $ArgH^+(H_2O)_n$, and (c) $ArgH^+(H_2O)_n$ ions for n = 1–13 were obtained from solutions of 200 μM GdmHCl or 300 μM arginine solutions in 18.2 MΩ H_2O. Structure I shows a proposed structure populated by $GdmH^+(H_2O)_n$ ions where n = 6. (adapted from ref. 142 . Structures II, III, and IV are proposed structures for the ions that fall on the respective ATD trendlines in (c) (adapted from ref. 140. The peak labeled with an asterisk denotes a fragment carbocation. 28

Figure 2.3. ATD vs m/z plot of $MeRH^+(H_2O)_n$ ions for n = 1-13 obtained from a solution of 300 μM methyl ester arginine in 18.2 MΩ H_2O and a tip with an outer diameter of ~3-5 μm. A dashed line shows a single transition in the hydrogen bonding network, similar to what is observed for the $GdmH^+(H_2O)_n$ series.....29

Figure 2.4. Two-dimensional contour plots of ATD vs *m*/*z* of (a) $GdmH^+(H_2O)_n$ and (b) $ArgH^+(H_2O)_n$ ions obtained from solutions of 400 μM GdmHCl in 0.1% formic acid or 300 μM arginine in 18.2 MΩ H_2O. A proposed structure of $GdmH^+$–$GdmH^+(H_2O)_{12}$ like-charged complex is shown in the inset; N–H---O and water–water hydrogen bonds are shown with orange and blue dashed lines, respectively. This structure is similar to that reported by Vazdar et al. in ref. 123. (c) Mass spectrum extracted from the region between *m*/*z* 340 and 485 showing hydrated like-charged ion pairs ($GdmH^+$–$GdmH^+(H_2O)_n$, red) and ($GdmH^+$–$H^+(H_2O)_n$, black).....31

Figure 2.5. ATD vs m/z plot of $NH_4^+(H_2O)_n$ ions obtained from a solution of 400 μM NH_4Cl in 18.2 MΩ H_2O and a tip with an outer diameter of ~15 μm. All ions contained in this plot carry a charge of +1. Ions that carry a +2 charge would fall on a different trendline. See Figure 2.4 for comparison. The same experiment in 0.1% formic acid was performed, with similar results, but the

spectrum becomes difficult to resolve due to the presence of $H^+(H_2O)_n$ clusters. Notably, no 2^+ clusters were detected in either case. Magic number clusters at n = 20 and 27 are marked. 33

Figure 2.6. The electric fields at (a and b) the C+, (c and d) the hydronium ion O^+, and the Na^+ atom locations, resulting from the (a and c) surrounding water network and (b and d) opposite ion were determined. The green atom represents the location the electric field was calculated at, and the arrow shows the unit vector of the electric field. Black atoms were excluded from the electric field calculation.....37

Figure 2.7. Van der Waals and H-bonding interactions are shown for $GdmH^+$-$H_3O^+(H_2O)_{18}$ by green and teal surfaces, respectively. 39

Figure 2.8. (a) ATD vs m/z plot of bradykinin (BK) and (b) an extracted ATD vs m/z plot of the highlighted region, revealing m/z peaks separated by 6 m/z, corresponding to hydrated BK^{3+} ions. The mass spectrum is above each plot and the number of water molecules adducted to BK^{3+} is above each peak.....41

Figure 3.1. ATD vs m/z plots of 4-$ABAH^+(H_2O)_n$ sprayed from 0.1% formic acid with helium drift gas at a heated capillary temperature of 330 K. Panel (b) is an expanded plot of panel (a). Asterisk denotes 94 *m/z* (CO_2 loss) and double asterisk denotes 120 *m/z* (H_2O loss) fragments (refs. 78, 96-99, 156). The mass spectrum is located above each plot. 51

Figure 3.2. ATD vs m/z plots of (a) 2-$ABAH^+(H_2O)_n$ and (b) 3-$ABAH^+(H_2O)_n$ sprayed from 0.1% formic acid with helium drift gas at a heated capillary temperature of 330 and 303 K, respectively. * denotes 94 m/z (CO_2 loss). The mass spectrum is located above each plot. Trendlines drawn on each plot highlight the non-spherical growth of the 2-$ABAH^+(H_2O)_n$ water clusters. That is, 2-$ABAH^+(H_2O)_n$ does not form a solvent bridge connecting both ends of the benzene, since the functional groups of 2-ABA are adjacent, resulting in the linear ATD trendline observed in (a). 2-ABA and 3-ABA do not display proton transfer behavior via ATD inflections in the n = 5-9 region but are included here for completeness.....52

Figure 3.3. MCMM of 2-$ABAH^+(H_2O)_n$ where (a) n = 10 and (b) n = 20. Note that the proton is located classically on the carboxylic acid in the simulation, but the proton H-bonds with the amine group. Additionally, the hydration does not bridge the rest of the molecule as observed for 3-$ABAH^+(H_2O)_{10}$ and 4-$ABAH^+(H_2O)_{10}$, instead preferring to form a droplet surrounding the hydrophilic region.....53

Figure 3.4. ATD vs *m/z* plots of 4-$ABAH^+(H_2O)_n$ at a heated capillary temperature of (a) 371 and (b) 330 K sprayed from 1:1 ACN:H_2O solutions with 0.1%

formic acid with helium drift gas. $H^+(H_2O)_n$, 4-$ABAH^+(H_2O)_n$, and $NH_3^+C_6H_5(ACN)_1(H_2O)_n$ are labeled in blue, black, and red, respectively. Asterisk denotes 94 *m*/*z* (CO_2 loss), and double asterisk denotes 120 *m*/*z* (H_2O loss) fragments. The $(4\text{-}ABA)_2H^+(H_2O)_n$ proton-bound dimer and its *n* = 1 species are observed at 275 and 293 *m*/*z*, respectively. The dimer experiences the same hydrated, ACN-bound adduct as the monomer at 272 and 290 *m*/*z*. The mass spectrum is located above each plot. 54

Figure 3.5. ATD vs m/z plot of 4-$ABAH^+(H_2O)_n$ with a heated capillary temperature of 330 K sprayed from 1:1 ACN:H_2O solutions with 0.1% formic acid. 4-$ABAH^+(H_2O)_n$ peaks display the same behavior (inflections at n = 5-9 and n = 20) as clusters obtained in 0.1% formic acid. See Figure 3.4 for comparison. The mass spectrum is located above the plot. 55

Figure 3.6. (a) ATD vs *m*/*z* plot of 4-$ABAH^+(H_2O)_n$ sprayed from 0.1% formic acid with N_2 drift gas. The mass spectrum is located above the plot. (b) ATDs of 4-$ABAH^+(H_2O)_{0,4,5,6}$ are labeled. Gaussian peaks were fit with MATLAB. Blue dots correspond to the unfitted data. Orange peaks indicate the O-protomer, while gray peaks indicate the N-protomer. The drift times are both longer and broader for N_2 drift gas than He drift gas due to the increased size and interaction potential with N_2. The ion gate is also 50% larger (36 μs) for N_2 than for He drift gas (24 μs), which increases the breadth of the peaks. 57

Figure 3.7. Calculated lowest energy structures and relative 83 K Gibbs free energies for 4-$ABAH^+(H2O)_{1\text{-}6}$. Relative energies were calculated at the B3LYP/6-311++G** level of theory and ωB97X-D functional in Gaussian 16. The n indicates the numbers of water molecules adducted to 4-$ABAH^+$. 60

Figure 3.8. Calibration plot of 4-$ABAH^+(H_2O)_{0\text{–}6}$ based on CCS of calculated lowest energy structures in Figure 3.7. O-protonated CCSs were used for n = 0-5 (blue diamonds). The N- and O-protonated values for *n* = 6 are denoted by a green triangle and red square, respectively. Error bars represent the standard deviation of the *y* value. The slope of the line corresponds to the gas density in units of parts per m^{-3}, which corresponds to ~0.25 torr at 83 K. 61

Figure 3.9. The trans (Z) and cis (E) forms of 4-$ABAH^+(H_2O)_2$ are shown. The trans structure is favored by only 0.27 kcal/mol. 63

Figure 4.1. ATD vs m/z plots of (A-B) heptylammonium$^+(H_2O)_n$, (C-D) anilinium$^+(H_2O)_n$, and (E-F) 4-$ABAH^+(H_2O)_n$ sprayed from 0.1% formic acid. The mass spectrum is located above each plot. Lines are shown only to guide the eye and do not necessarily represent linearity of the ATDs. 69

Figure 4.2. Representative lowest energy structures of (top) Heptylammonium$^{+}(H_2O)_{20}$, (middle) 4-ABAH^{+}(H2O)$_{20}$, and (bottom) anilinium$(H_2O)_{20}$. Hydration favoring primarily the $–NH_3^{+}$ (right) are compared to more compact structures that do not favor hydration of only the $–NH_3^{+}$ (left). Relative energy values are labelled. The hydrophobic hydration was calculated to be favored by ~2.72 kcal/mol. 71

Figure 5.1. (top) A 3-D rendering of the R. M Jordan ToF. Comparison of the isotopic mass spectra of SP^{2+} from (middle) the first generation ToF with ~500 mass resolution and (bottom) the R. M. Jordan ToF with ~3500 mass resolution. ...76

Figure 5.2. Hydration of the peptide 10 µM AEK_4 in 0.1% FA. Hydration of only the more highly charged peptide indicates that the lower charge state is formed after nearly complete dehydration of the $AEK_4^{4+}(H_2O)_n$ ion. 77

Figure 5.3. ATD vs m/z plot of 50 µM SP in 1 µM trimethylammonium oxide and water reveals hydrated $2SP^{4+}$ ions. 78

Figure 5.4. ATD vs m/z plot of 100 µM ubiquitin in 0.1% FA, sprayed at a heated capillary temperature of 355 K. This spectrum shows the dehydration of dimers that dissociate to form monomers (M^{7+}/M^{8+}), but also reveals other overlapping hydrated charge states. A potential hydrated 15^{+} trimer (T^{15+}) is labelled.....79

Figure 5.5. ATD vs m/z plot of 30 µM cytochrome c in 18.2 MΩ H_2O. The charge state is marked above each hydration trendline. The number of water molecules adducted to the 8^{+} charge state are labelled.....80

Figure 5.6. (a) A typical IM gating (blue) and signal collection (red) event are compared to two multiplexing methods, (b) a correlation IMS method that opens the gate with increasing frequency and (c) a Hadamard Transform that opens the gate many times per cycle. The two multiplexing methods result in many signal outputs that must be deconvoluted. The gate is open at 321 V and closed at 400 V.....81

Figure 5.7. (a) Mass spectrum of SP and (b) ATD of SP accumulated under a 1 second correlation multiplexed gate. Note the increasing frequency of the observed signal. 82

Figure 5.8. ATD vs m/z plots of SP water clusters. Sprayed solutions contain (a) 50 µM SP in water, (b) 50 µM SP in 1 µM TMAO, (c) 50 µM SP in 1 µM TMAO and 1 µM urea, and (d) 50 µM SP in 50 µM urea. Dashed lines show the hydration trendlines of different charge states. 87

Figure 5.9. ATD vs m/z plots of 25 µM bovine insulin electrosprayed at a heated inlet temperature of (a) 349 K and (B) 355 K. Dehydrated protomer (M^{z+}), diprotomer (D^{z+}), and triprotomer (T^{z+}) ions are labelled. 90

Figure 5.10. (a and b) ATD vs m/z plots of 100 µM bovine insulin in (a) 100% H_2O and (b) 20% ethanol and 80% H_2O. (c and d) ATD of the 1434 m/z peak showing the diprotomer (D^{8+}) and protomer (M^{4+}) IM peaks. The diprotomer is abundant in (c) 100% H_2O solutions and diminished in (d) 20% ethanol 80% H_2O. 92

LIST OF TABLES

Page

Table 2.1. The electric field originating from the bolded portion of each complex is determined for each column of atoms. The electric field is only determined in these cases for the field in the axis between the two ions in each complex and is lower than the total field exhibited. The letter code for each case corresponds to the letter code in Figure 2.6. Positive numbers represent electric fields directing an ion away from the opposing ion (outwards/away from the droplet), while negative numbers represent fields directing an ion towards the opposing ion (inwards/towards the droplet). 38

Table 3.1. Trajectory method CCS values and standard deviations of 4-ABAH$^+$(H$_2$O)$_{0\text{-}6}$ in helium at 83 K. 59

1. INTRODUCTION: ION MOBILITY AND MASS SPECTROMETRY

1.1. Ion Mobility Spectrometry

Thomson and Rutherford originally studied the mobility of ions in different gases.[1] Shortly after, Zeleny used a counterflow drift gas for ions to traverse, a staple of modern ion mobility spectrometry (IMS) instrumentation.[2] IMS grew slowly as an analytical technique, primarily as a measure of small ion motion in gases.[3] The low cost, portability, and speed of the IMS instrumentation has made the technique accessible to field applications; IMS devices are now typically employed for rapid detection hazardous chemicals, like explosives[4-6] or illicit drugs.[7]

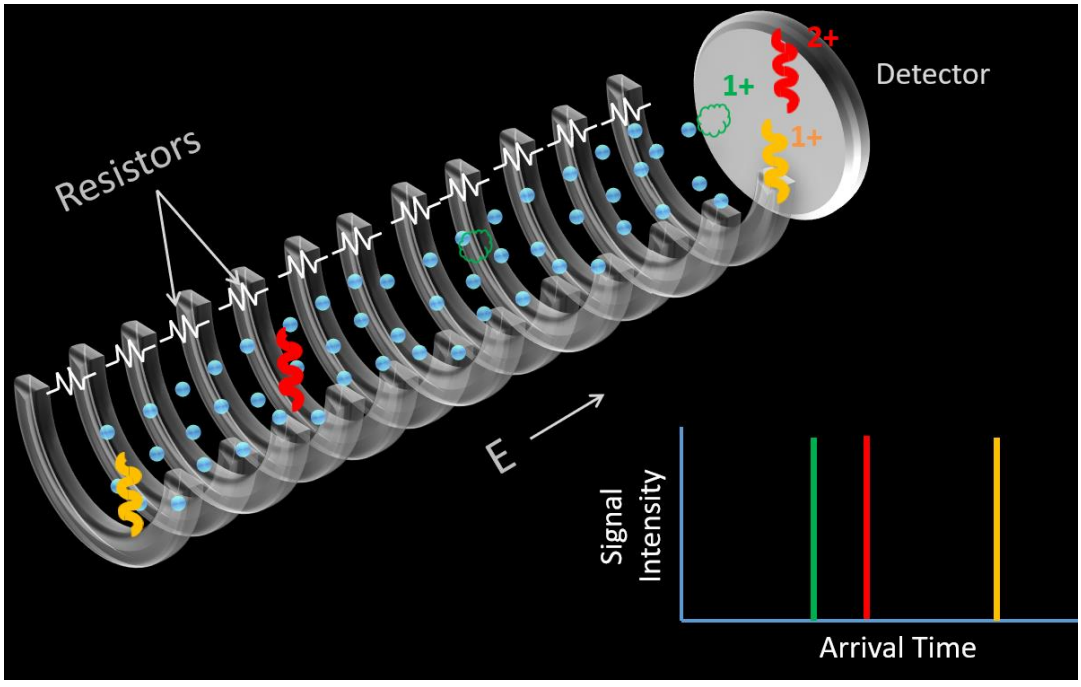

Figure 1.1. A model of the mobility experiment, showing separation based on molecule size (green/orange) and charge (red/orange). The green ion has the highest mobility, K, and the fastest arrival time.

IMS is most analogous to a capillary electrophoresis experiment that occurs in the gas-phase. An applied electric field directs ions through a background buffer gas, usually helium or nitrogen, allowing separation based on total charge, size, and shape of the ion, shown in **Figure 1.1**. There is some dependency on the interaction potential of the ion with the background gas; polarizable buffer gases can separate isomers by polarity. Dopants can increase separation in a similar manner without largely changing the background gas.

Ions are assigned a mobility parameter (K), shown by **equation 1.1**,

$$K = \frac{3\sqrt{2\pi/\mu k_B T}}{16} Q N^{-1} \Omega^{-1} \quad (\mathbf{1.1})$$

where μ is the reduced mass of the drift gas and analyte, k_B is the Boltzmann constant, T is the temperature, Q is the charge of the ion, N is the number density of the drift gas, and Ω is the collision cross section (CCS) of the ion. Typically, direct correlation to gas-phase CCS is a benefit of uniform field spectrometers, as K can be described experimentally by **equation 1.2**,

$$K = \frac{L^2}{U(t_{obs} - t_0)} \quad (\mathbf{1.2})$$

where L is the length of the drift tube, U is the applied voltage drop between the front and back of the drift tube, t_{obs} is the arrival time of an ion packet, and t_0 is the time the ion packet spends outside of the drift tube. CCS can subsequently be determined by substituting K in for **equation 1.1**.

The variables t_0 and P are often unknown and must be experimentally determined by setting equations 1 and 2 equal to each other. Because K is dependent on T and P, a

reduced mobility (K_0) is often reported under standard temperature (T_0) and pressure (P_0) so that values may easily be compared under any T and P conditions, described by **equation 1.3**.

$$K_0 = K\frac{T_0 P}{T P_0} \quad (\mathbf{1.3})$$

Although **equation 1.3** does considerably ease inter-laboratory reproducibility, K_0 is still temperature dependent, and large temperature differences from T_0, as in the case of the cryo-IM-MS result in different K_0 values.

1.2. Ion Mobility-Mass Spectrometry

Coupling IM and MS provides a rapid two-dimensional technique (IM-MS) that can characterize both analyte structure and the analyte mass-to-charge (m/z) for exact mass information. In 1961, Barnes *et al.* coupled an IMS and magnetic sector MS to create the first IM-MS instrument.[8-9] Shortly after, McAfee and Edelson coupled an IM to a time of flight (ToF) MS.[10] With IM-MS, structural information gained by IM could now separate isomers and multimers, which share the same m/z and are otherwise inseparable by MS alone. Structural isomers can be observed for small molecules.[11] However, Clemmer *et al.* showed that structural IM-MS techniques can be used to identify compact and extended biological structures, providing structural information about native-like proteins and protein complexes.[12] Thus, IM-MS began to gain traction as a structural technique, and currently there are ~250-300 papers published on IM-MS each year.[13] As mass resolution and sensitivity have increased, these studies have extended to even larger protein complexes and membrane proteins (up to several 100s kDa), providing a wealth

of information about biologically relevant quaternary structures,[14-15] post-translational modifications (PTMs),[16-17] ligand-protein interactions,[18] metal-binding interactions,[18] oxidation,[19] and protein-lipid interactions[20-23] and thermodynamics.[24]

Molecules must be ionized and submitted to the gas-phase prior to analysis by IM-MS. Several ionization techniques are suitable for IM-MS analyses, but by far the two most common ionization techniques are matrix assisted laser desorption ionization (MALDI)[25-26] and electrospray ionization (ESI).[27-29] MALDI operates with timed laser shots, which naturally makes MALDI amenable to the intermittent duty cycle of IM-MS. Although MALDI is a soft (non-activating) ionization technique, MALDI is limited to singly charged ions. With the rise of "native" IM-MS, which aims to kinetically trap solution-phase protein structures during ESI, an ionization technique that produced multiply charged biomolecules (and therefore smaller m/z) under non-activating conditions became necessary. These requirements are well satisfied by ESI.[30-32]

1.2.1. Electrospray Ionization

A considerable amount of work has been performed to understand the mechanism by which ions are generated via ESI, and two models have gained major traction: the ion evaporation model (IEM)[33-35] and the charged residue model (CRM).[28, 35-37] The CRM and IEM are modelled in **Figure 1.2**. Both models initiate in the same way: a large voltage is applied to the tip of a glass capillary, generating Taylor cone. From the Taylor cone, droplets containing many ions are generated. These droplets subsequently shrink due to evaporation. As the droplets shrink, the charge inside the droplet is naturally concentrated, increasing coulombic repulsion until the Rayleigh limit is reached, another Taylor cone is formed on the droplet, and the droplet spontaneously fissions. Droplets cool rapidly during

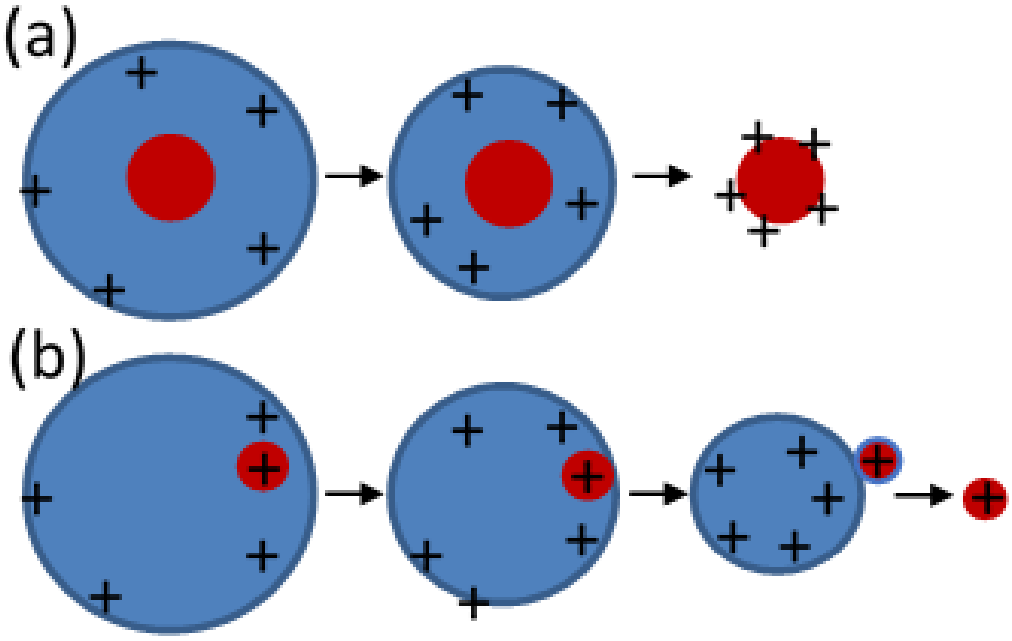

Figure 1.2. Droplets undergo many coulombic fission and evaporation events prior to reaching a ~10 nm diameter, where either the (a) charged residue model or (b) ion evaporation model likely become operative. The red circle represents the analyte in a droplet.

this evaporation cycle, and Beauchamp *et al.* coined the "freeze-drying" effect of ESI on biomolecules.[38] Droplets continue to fission in this way until droplets are in the size range of ~10-20 nm in diameter. At this point, the IEM states that the electric field generated by the ions becomes large enough to eject ions, with some number of water molecules, from the droplet. The CRM states that the ion instead is well-hydrated and remains in the center of the droplet, even if the charge is propagated to the surface. The dehydrated ion is generated by continued Rayleigh limited fission events followed by dehydration when there are very few water molecules remaining. At this point, the charges reside on the surface of the protein. By 2000, the consensus was that for ions smaller than ~1 kDa, the IEM is active, while for ions larger than ~6 kDa, the CRM is active.[37] However, several intermediate cases remain unclear. For the mass region between ~1-6 kDa (and even this region itself is uncertain), it is uncertain which, if either, of these two mechanisms is dominant.[37, 39-40] For instance, salt clusters, like $Na_nCl_m^{(n-m)+}$, can form very large clusters, with n+m > 100. The clusters easily extend into the 1-6 kDa region, and their mechanism of formation is still contested.[41-45] Some other models have since been proposed, including a combined model where CRM is first informed by the ions that undergo the IEM.[46-47] Additionally, a chain ejection model (CEM) was recently proposed for nonpolar polymer chains and unfolded proteins.[48-50] The basic tenets of CEM are similar to IEM, except that polymers are much larger and hydrophobic. Due to their very nonpolar nature, the polymers tend to reside near the surface of the droplet, and when one terminus is ejected, the rest of the chain follows, accumulating charges residing on or near the surface of the droplet as the chain is ejected. At this time, molecular dynamics simulations (MDS) have

unfortunately outpaced experimental investigations, and there is now a paucity of experimental evidence for the intricate nuances involved in ESI theory.[41, 49-58]

1.3. Cryogenic Ion Mobility-Mass Spectrometry

1.3.1. Instrumentation and Design

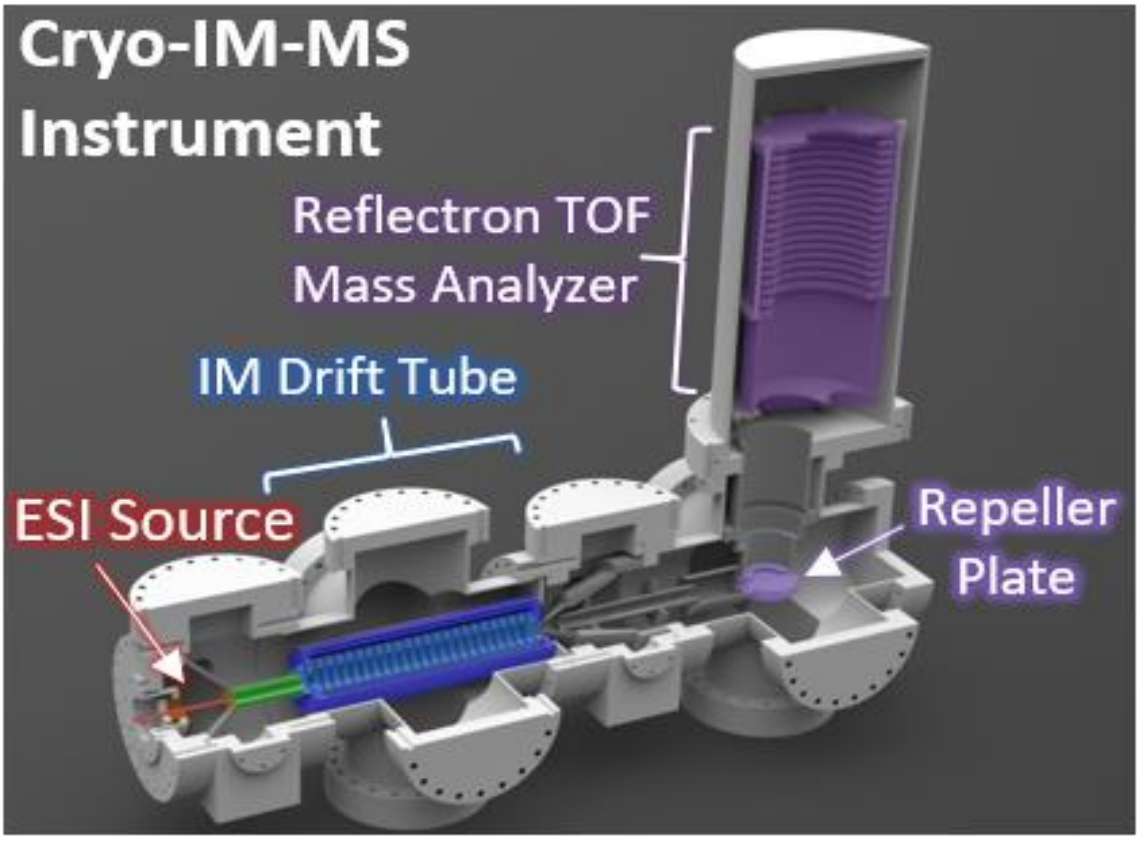

Figure 1.3. An overview of the cryo-IM-MS instrument. Hydrated ions generated in the source region are "freeze-dried" and kept cool within the cryogenically cooled (~80 K) drift cell. Ions are then transferred to the ToF source repeller plate and "pushed" to the ToF for mass analysis.

The cryogenic ion mobility-mass spectrometer (cryo-IM-MS), shown in **Figure 1.3** and **Figure 1.4**, has a cryogenic jacket surrounding the IM cell, to cool ions to 83 ± 2

K. Originally, the cold, uniform field IM was used to enhance the resolving power (R_P) of the drift cell, since IM R_P is affected by the temperature, as shown in **equation 1.4**,

$$R_P = \frac{t_D}{\Delta t_D} = \sqrt{\frac{LEQ}{16 k_B T ln2}} \quad (\mathbf{1.4})$$

where t_D is the ion drift time, Δt_D is the full width at half maximum of the drift time, L is the drift cell length, E is the electric field strength, Q is the ion charge, k_B is Boltzmann's constant, and T is the drift gas temperature. As shown in **equation 1.4**, R_P is proportional to $(1/T)^{1/2}$, resulting in a ~1.9-fold increase in R_P when decreasing the temperature from 300 to 80 K. Additionally, improved sensitivity and resolution result from freezing out impurities by pre-cooling the helium buffer gas to 80 K before use in the drift cell.

A description of specific instrumental details and typical operating conditions are detailed in the rest of this section.[59-60] Hydrated ions are produced via static spray, which uses <1 µL/hr, and has a tip outer diameter (OD) between 3-15 µm into the source region, shown in **Figure 1.4**. The change to static spray from direct infusion (~1 µL/min) has

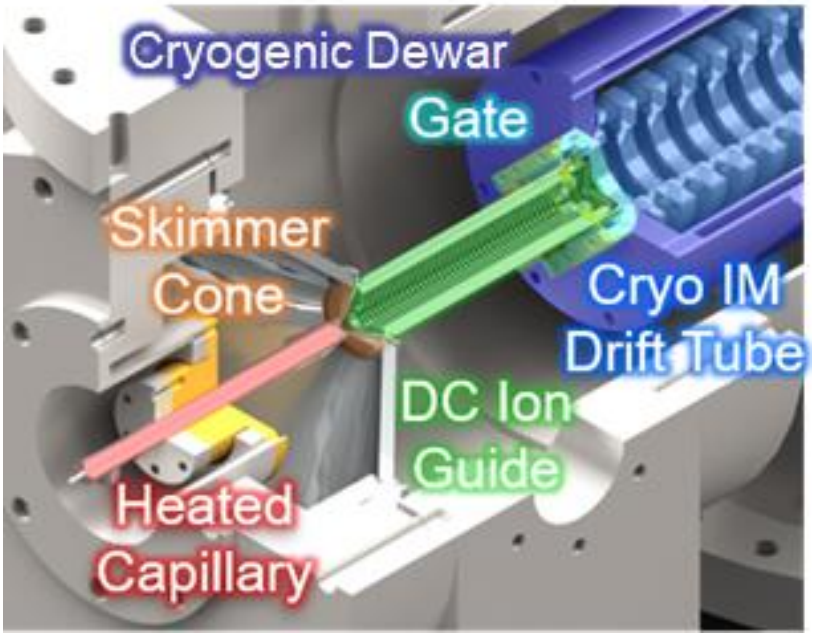

Figure 1.4. An expanded view of the source region. Each label is color coded to a section of the instrument. There are is an additional, unlabeled ring electrode after the DC Ion Guide and before the Gate. This lens is segmented into four quadrants and used as a deflector lens to guide the ions to the IM drift cell aperture.

considerably reduced the amount of solvent sprayed into the instrument, reducing the effects of icing inside the instrument. The reduced solvent load has allowed for longer experiment times with little or no effect on the number of ions that reach the detector, and less sample (~1/60th) is used. Generated ions are transmitted at atmospheric pressure through the heated capillary (11.4 cm, 400 µm inner diameter (ID)). The heated capillary is usually maintained between 334-336 K, and the temperature is closely tied to the

distribution of water clusters. Decreasing the temperature shifts the distribution of hydrated ions $[M+xH]^{x+}$ to larger values of n. However, the temperature necessary also depends on the analyte. Peptides require higher temperatures (~340K), and proteins require even higher temperatures for good ionization and signal (~345-355 K). If dehydrating conditions are desired, temperatures can be raised to >363 K. After exiting the heated capillary, ions are focused through a skimmer cone separated by 2 mm and at ~1.0 Torr to a DC ion guide region at $\sim 2.0 \times 10^{-4}$ torr. The DC ion guide consists of 43 lenses with an ID of 6.35 mm, thickness of 1.27 mm, and 1.27 mm spacing between lenses. Each lens potential is alternated by the same voltage. Lower alternating voltages (~20 V) are selected for focusing smaller ions (less than 1 kDa), while larger voltages (~40 V) are selected for larger ions (more than 1 kDa). Ions are focused by the oscillatory radial electric field, which acts as an RF to the fast motion of the ions. Ions are focused through a segmented deflector lens and a gating lens. The gating lens is pulsed for ~24 μs at ~800 Hz from 400 V to 321 V, allowing for discrete packets that may be temporally separated in the drift cell. Collisions with helium drift gas provide for IM separation as described in section **1.1**. The IM drift cell is 30.2 cm long, and the entrance and exit apertures are 800 μm in diameter. The drift cell contains 24 stainless steel stacked ring lenses with 6.35 mm width and spacing and an ID of 28.6 mm. Each lens is spaced by alumina nonporous ceramic balls (8 mm diameter, McMaster-Carr, Aurora, OH) and is serially connected by 1 MΩ resistors (front to back resistance is 23.0 MΩ). The lens elements are sealed and compressed using 0.060” indium wire seals (Indium Wire Extrusion, Ellicot City, MD). The cryogenic dewar is electrically isolated from the stacked ring lenses by an insulating

spacer. The dewar is filled with liquid nitrogen, cooling the drift cell and the 99.999% ultra-high purity helium gas to ~83 ± 2 K. The temperature is measured by a 100 Ω resistance ceramic wire wound platinum resistive temperature detector (RTD, part 1PT100KN3026, Omega Engineering Inc. Norwalk, CT) platinum thermocouple. The temperature of the drift cell is very sensitive to air leaks, and it is emphasized here that leakage can easily be detected by increased drift tube temperatures (>~84-85 K). Previous calibrations have suggested the drift cell pressure is at ~1.6 Torr,[59] but more recent calibrations suggest the drift cell pressure may be closer to ~0.25 Torr (see section **3.2.3**). After separation by the IM drift cell, ions traverse a 5-einzel lens region, a field free region, and are then collimated into the ToF source region. Ions are then orthogonally pulsed into the reflectron ToF MS. This ToF was adapted from a commercial instrument (Vestec Mariner ToF) and is maintained at ~$1x10^{-7}$ Torr. The ToF push/repeller plate is maintained at 3.52 kV and pulsed 7-15 kHz based on ion flight times. The reflectron back ring is maintained at 4.5 kV. A 40 mm dual microchannel plate (Photonis, Surbridge, MA) detects impacting ions.

1.3.2. A Novel Way to Study Water Adduction

Water has many important biological roles, *e.g.* the hydrophobic effect, resource transport, and chemical reactions. Structural investigations of water could lead to insights in proton transfer, protein folding and aggregation, and how ions can order the surrounding water network. Each of these roles is performed within a confined cellular environment, and the ESI-generated nanodroplets provide a useful, analogous mode to study such

confinement. However, water is very weakly bound to most ESI-generated ions and is lost in typical IM-MS experiments; hot source conditions can remove the water, while IM drift cells maintained at room temperature rapidly thermalize "freeze-dried" ions, also removing water clusters. Silveira *et al.* designed an ESI source for the cryo-IM-MS, which evaporatively pre-cools ions to ~130-150 K,[61] allowing water clusters to be retained or "freeze-dried" on generated ions. The 80 K drift tube subsequently kinetically traps the "freeze-dried" ions, preserving large distributions of water clusters.[60] Notably, the degree of hydration is dependent on the activation of the ions, leading to dependencies on the field strength, heated capillary temperature, and all the voltage drops within the instrument. Tuning these conditions away from desolvating/heating conditions necessarily reduces the ionization efficiency, and all analytical values of merit that depend on signal strength. However, such losses must be accepted to perform the unique experiments that follow.

Several studies have associated water molecules with peptides inside a drift tube by doping water vapor into the drift gas or using water vapor as a drift gas.[62-68] Just a few water molecules are often sufficient to cause significant re-arrangement or folding of peptides in these studies.[62-63] However, condensed water molecules may behave differently than evaporating molecules. For instance, solution-phase states cannot be kinetically trapped and observed; gas-phase favored hydration sites will be selected first. Subsequent hydration will preferentially H-bond with that site until the droplet is large enough to hydrate both sites. However, the size and structure of the droplet required to search the structural space for the reverse transition (gas-to-solution phase) may be

considerably removed from the structure that forms in the solution-to-gas phase transition. The latter transition is also of considerable interest, because the solution-to-gas-phase transition describes unresolved questions of the final stages of ESI. It is again emphasized that cryo-IM-MS preserves solution-phase states by slowly *dehydrating* ESI-generated droplets, rather than condensing water molecules onto a fully dehydrated gas-phase analyte. Furthermore, due to the cryogenic cooling of the drift gas prior to entry into the drift cell, the drift gas is dry, ensuring there is no condensation. It is noted that in both scenarios, extremely cool operating conditions are required to maintain hydrated ions. For instance, **Figure 1.5** describes the sensitivity of the observed structures to (a) the heated capillary temperature and (b) electric field strength.[60] However, there are many other

sensitive parameters, including the vacuum, the pressure inside the drift tube, and the drift gas composition.

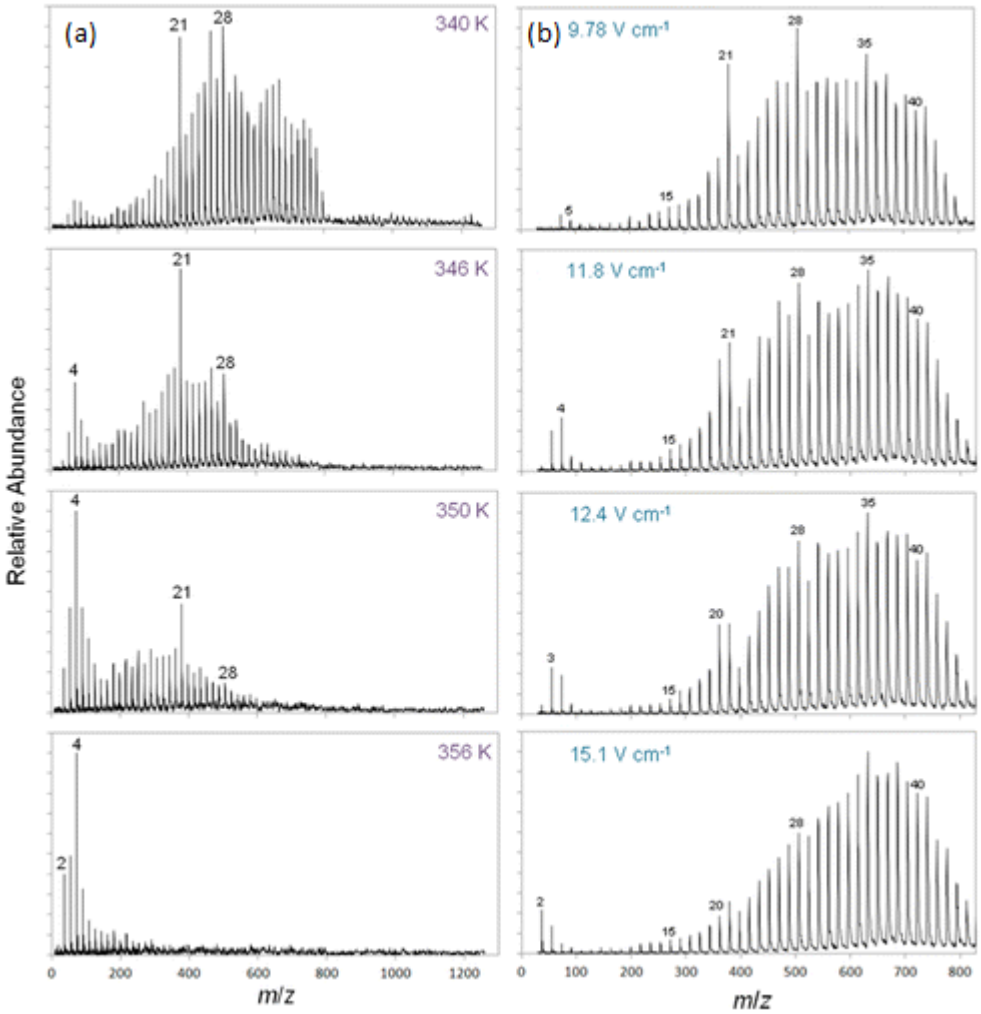

Figure 1.5. Mass spectra of protonated water clusters at (a) variable heated capillary temperatures and (b) variable IM field strengths. The field strength in (a) is 9.12 V/cm and the heated capillary temperature in (b) is 340 K. Adapted with permission from ref. 60. Copyright 2013 American Chemical Society.

1.3.3. Protonated Water Clusters: $H^+(H_2O)_n$

Spectroscopic experiments that study the free-OH spectral region (~3700 cm^{-1}) have dominated the experimental study of hydrogen bonded (H-bond) networks, which

detail the H-bonding environment each water molecule is in, *i.e.*, whether a water molecule is accepting (A) or donating (D) H-bond(s). These studies have detailed hydrated structures, including magic and anti-magic number clusters,[69-73] H-bond coordination,[73-76] H-bond re-arrangement as a function of the analyte and numbers of waters,[77-79] the formation of amino acid zwitterions,[80-82] clathrate structures,[73, 75, 83-85] the location and nature of the charge/proton,[78, 83, 86] and the temperature dependence of the structures.[76, 87-88] These studies heavily rely upon MDS to assign the free-OH region bands, but this can be computationally expensive due to the large expanse of computational space required, and lack of other experimental structural parameterizations to reduce that computational space. In addition, spectroscopy is not structurally dispersive, meaning that all present structures are simultaneously acquired, making large, structurally heterogeneous water clusters particularly difficult to analyze.[89]

Ion mobility is structurally dispersive, separating each present structure according to its size, shape, and charge and provides an additional limiting parameter, CCS, for MDS. For instance, identifying Eigen (H_3O^+) and Zundel ($H_2O_5^+$) structures with spectroscopy can be difficult even at relatively low water cluster sizes due to the mixing H-bonding bands from each water cluster type. Jiang *et al.* predicted the coexistence of Eigen and Zundel structures as low as $H^+(H_2O)_6$ by comparing ab initio calculated spectra to their experimental spectroscopic data.[76] Fujii *et al.* showed that the smallest water cluster to contain both Eigen- and Zundel-centered structures existed at n = 6.[90] Servage *et al.* used cryo-IM-MS to separate these $H^+(H_2O)_6$ structural isomers, as shown in **Figure 1.6**.[91] The CCSs of the Eigen- and Zundel-centered structures were estimated to be 46.46

Å^2 and 47.97 Å^2, respectively, with MOBCAL.[92] Jiang *et al.* determined the Zundel-centered structure to be ~1 kcal/mol more stable than the Eigen-centered structure, in agreement with the greater relative abundances observed at the longer ATD in **Figure 1.6**.[76] Similarly, Silveira *et al.* describe two distinct populations of $H^+(H_2O)_{21}$ water clusters, shown in **Figure 1.7**.[60] One population follows the trendline of water structures. A second, more compact, population appears at a faster ATD. The former population forms with more dangling H-atoms and fewer total H-bonds than the latter, causing its increased size relative to the closed clathrate cage structure that describes the faster ATD. The sensitivity of the water structure to the electric field is also exemplified in **Figure 1.7b**, where the cage structure dissipates in favor of more open structures at higher field

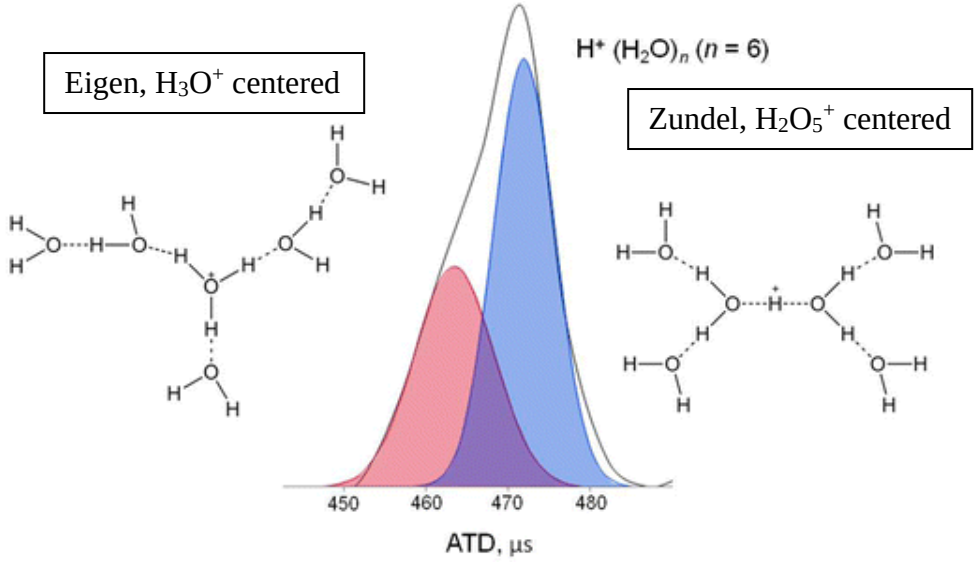

Figure 1.6. Mass-selected ATD for $H^+(H_2O)_n$ (n = 6); peak fitting was performed using Origin 7.5 software. The faster conformer population shown in red corresponds to Eigen (H_3O^+-centered) structures, while the population falling at longer drift times shown in blue is attributed to the Zundel ($H_5O_2^+$-centered) structures solvated by four water monomers. Structures shown are schematic representations of the two lowest energy isomers for the $H^+(H_2O)_n$ (n = 6) cluster determined by Jiang et al. via ab initio calculations.[76] Reprinted with permissions from ref. 91. Copyright 2014 American Chemical Society.

strengths. This sensitivity to the field strength represents one of the major hurdles to the determination of CCS for this technique and is addressed in more depth in **Chapter 3**. These examples lay the foundation for studying changes in proton location and structures that depend on the proton location. An analysis of how a proton is transferred is pursued for the molecule 4-aminobenzoic acid (4-ABAH$^+$) in **Chapter 3**.

1.3.4. Hydration of Polar Molecules

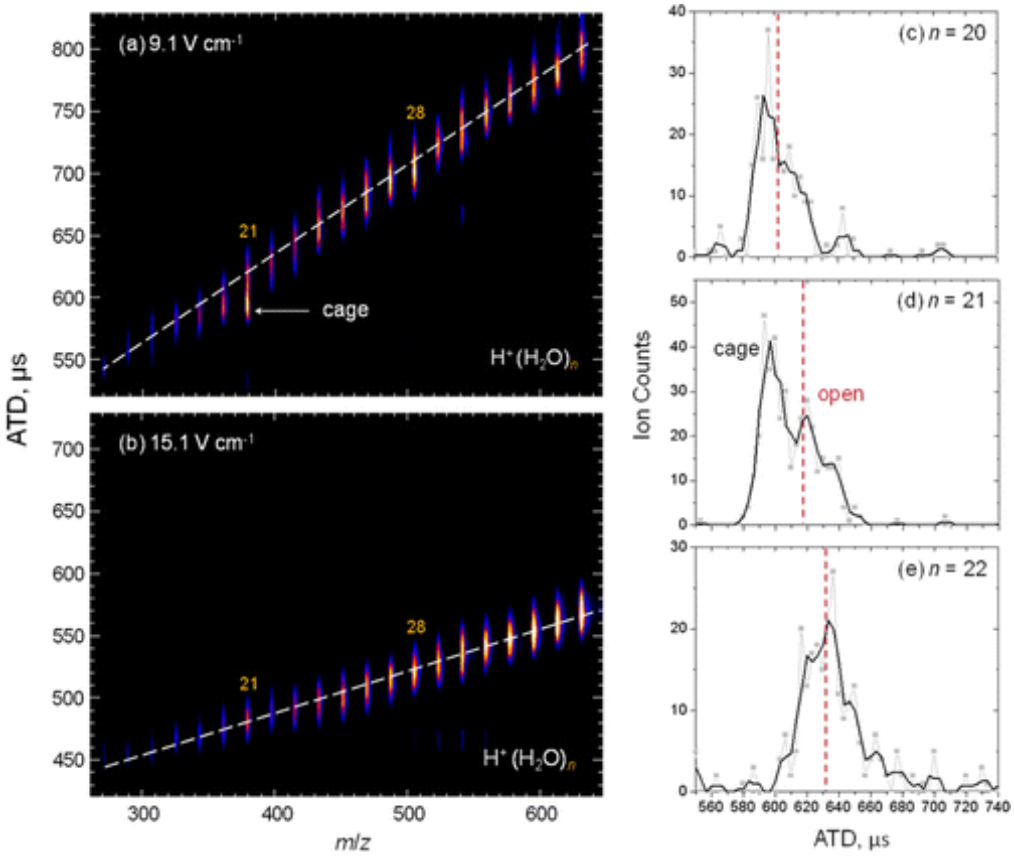

Figure 1.7. ATD vs m/z plot for $H^+(H_2O)_n$ (n = 15 to 35) produced at an electric field of (a) 9.1 V cm^{-1} and (b) 15.1 V cm^{-1} in the drift tube at a heated capillary temperature of 340 K. Panels c–e contain the mass-selected ATDs for (n = 20 to 22) at 9.1 V cm^{-1}. The black line is the result of boxcar averaging of the data points (gray ■). The vertical dashed line was inserted to guide the eye across the centroid of the IM-MS trendlines shown. Reprinted with permissions from ref. 60. Copyright 2013 American Chemical Society.

Charge carriers are capable of profound structuring effects on the local environment, especially nearby H-bonding water molecules.[38, 60, 62, 78, 93-99] Water molecules also have key roles in defining the structures of polar molecules. Understanding the interplay between these two forces is important for developing a more thorough understanding of how the presence or absence of water influences the structures of biomolecules,[95, 100-101] as well as how polar molecules alter the structure of water.[38, 60, 91, 93, 95, 102] While examples were provided in section **1.3.3**, it is again noted that at 80 K, cryo-IM-MS of protonated water clusters has revealed increased relative abundances of "magic" number clusters that orient water to form very stable geometric structures.[38, 60, 73, 91, 93, 102-103] The water network is even sensitive to different protomer states.[95] Alternatively, for the model peptide substance P (SP; RPKPQQFFGLM), a compact conformation is favored when the ions are dehydrated slowly, whereas an extended gas-

phase conformation is the most stable gas-phase conformer, as shown in **Figure 1.8**.[100] The two charged groups in diammonium alkyl ions are stabilized within a single cluster for n > ~20 by hydrating water molecules.[95, 104] Similarly, solvent-free monomer ions of the protein ubiquitin were detected only after near-complete desolvation of the dimer ions, as shown in **Figure 1.9**.[101] It appears that hydrated dimer ions are stabilized by formation of a water bridge involving the hydrophilic side chains that surround the I44 hydrophobic patch of each monomer.[105-107] These studies represent the first steps to answering a recurring question in this work: how do soluble, polar molecules alter the surrounding

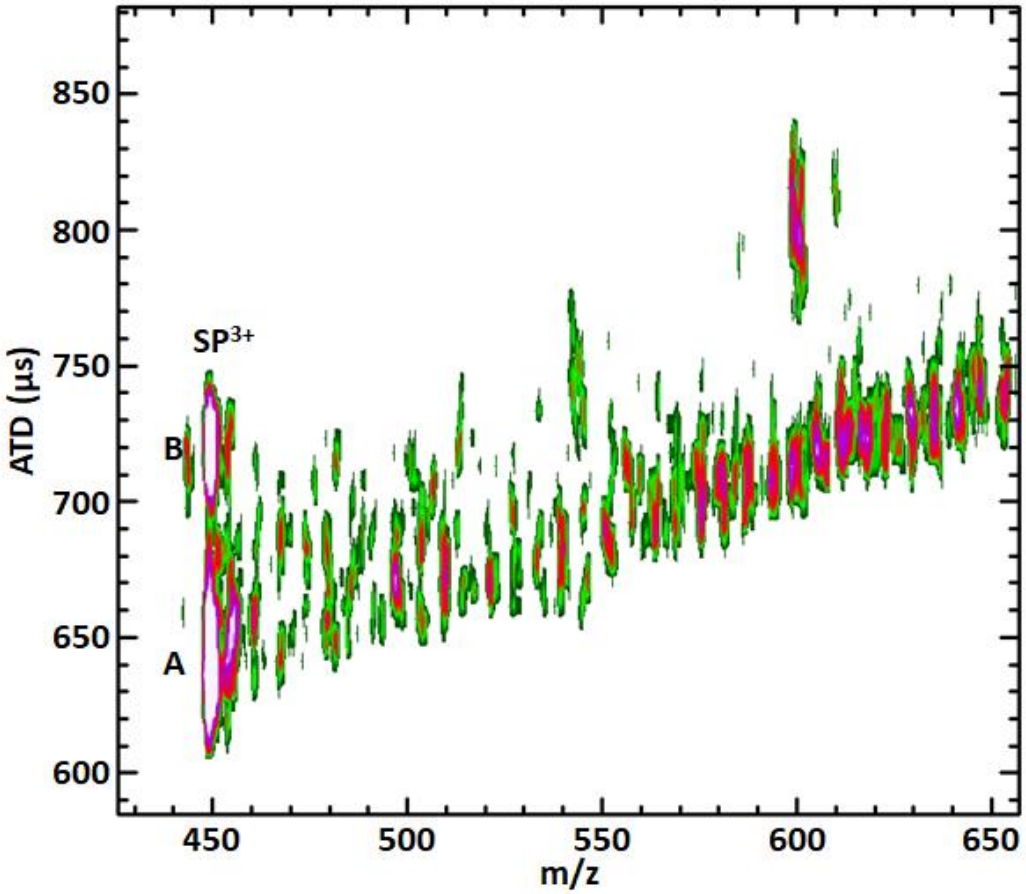

Figure 1.8. ATD vs m/z plot of substance P detailing the conversion of a hydrated conformation, A, to an extended gas-phase conformation, labelled B. The conversion occurs after near complete dehydration.

water structure and how does the presence of water alter the structure of the polar molecule?

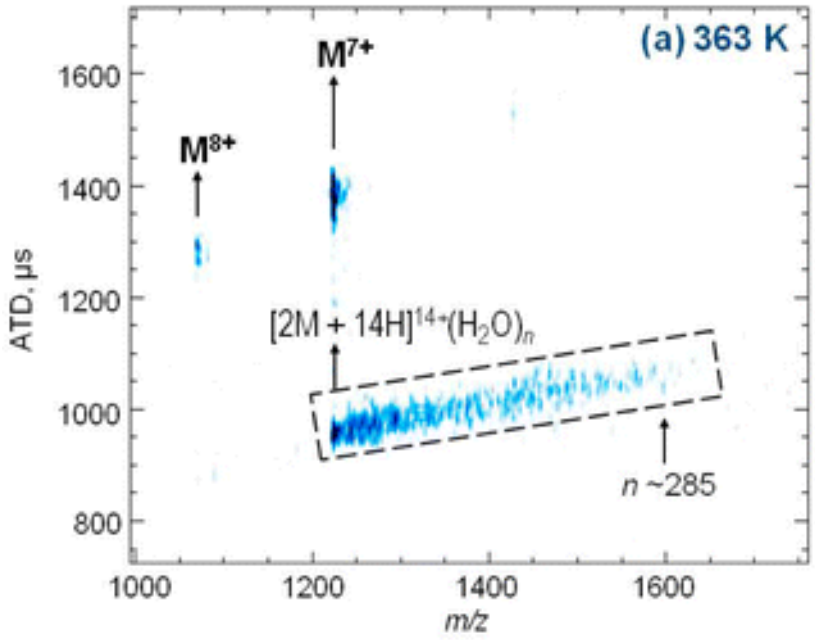

Figure 1.9. ATD vs m/z plot of 10 µM ubiquitin in 0.1% formic acid (FA) and heated capillary temperature of 363 K. Note the monomer is observed without significant hydration. Adapted with permission from ref. 101. Copyright 2015 American Chemical Society.

1.4. Thesis Structure

In **Chapter 2**, the hydration of guanidinium ($GdmH^+$) and arginine ($ArgH^+$) ions with cryo-IM-MS is described. $GdmH^+$ ions are reported to form stable complexes ($GdmH^+$-$GdmH^+$) in aqueous solutions despite strong repulsive interactions from each charge. These complexes are thought to play important roles in protein folding, membrane penetration, and the formation of protein dimers. In this chapter, cryo-IM-MS results for hydrated guanidinium ion pairs, *i.e.* ($GdmH^+$-$GdmH^+(H_2O)_n$ are reported. The binding

interactions leading to formation and stability of these ion pairs are discussed in the context of theoretical work and the observation of another unlikely, and previously unstudied, ion pair, $GdmH^+$-$H^+(H_2O)_n$.

In **Chapter 3,** an intracluster proton transfer reaction is investigated via the hydrated ion 4-aminobenzoic acid (4-$ABAH^+(H_2O)_n$), which is known to undergo a late-stage ESI proton transfer from its solution-phase location on the $–NH_3^+$ group to form a $–COHOH^+$ group. Presented evidence suggests that the proton transfer occurs at n = 6 through a water bridge, probably via a Grotthuss-type mechanism. CCS calculations are performed to calibrate cryo-IM-MS for CCS for the first time and determine structural families that are present for the proton transfer. Solvents and background collision gases influence the proton transfer reaction, and the effects of acetonitrile and nitrogen drift gas are investigated.

In **Chapter 4**, CCS calibrations are extended to larger water clusters of 4-$ABAH^+(H_2O)_n$. The formation of magic number clusters is well-described, but these structural phenomena usually entail small restructurings of dodecahedral cages. Here, the formation of the magic number cluster n = 20 requires a significant transformation relative to the clusters n = 19 and 21; the 4-$ABAH^+(H_2O)_{20}$ magic number cluster forms a dodecahedral cage structure, whereas 4-$ABAH^+(H_2O)_{19,21}$ clusters form a water bridge between the two hydrophilic groups.

Upcoming studies, instrument developments, and a final outlook for the project and instrument are detailed in **Chapter 5**.

2. HYDRATION OF GUANIDINIUM IONS: AN EXPERIMENTAL SEARCH FOR LIKE-CHARGED ION PAIRS*

2.1. Background

Many of the binding forces that typically affect solvated molecules are generally well-understood. Briefly, the hydrophobic effect is an important folding effector that has been extensively studied.[108-111] Interactions between hydrophilic groups and water, which include both short- and long-range interactions, strongly influence the structures of both the hydrated ion as well as the hydrating waters.[94] The influence of hydration is probably strongest for polar amino acid side chains that are located on the protein surface, but the solvation of polar side chains within the protein core can also be an important determinant for protein folding.[111] Electrostatic interactions involving basic and acidic amino acid side chains have been extensively studied, especially those involving the side chain of arginine, *i.e.* guanidinium ($GdmH^+$), with aspartic and glutamic acid,[112] although interactions of $GdmH^+$ with Trp, Arg, and Gln (pi-stacking interactions)[113-114] and with hydrophobic amino acid side chains have also been reported.[115]

The interactions involving like-charged $GdmH^+$-$GdmH^+$ has been studied as well; semiempirical calculations provide evidence for like-charged guanidinium-guanidinium ($GdmH^+$-$GdmH^+$) complexes stabilized by water molecules.[101] Two papers by Scheraga

---

* Reprinted with permission from Hebert, M. J. and Russell, D. H., Hydration of Guanidinium Ions: An Experimental Search for Like-Charged Ion Pairs. *J. Phys. Chem. Lettrs,* **2019,** *10* (6), 1349-1354 DOI: 10.1021/acs.jpclett.9b00268.

et al. revealed that pairing of positively charged $GdmH^+$ ions on arginine side chains forms stable complexes in aqueous solutions, *seemingly unlikely considering potentially effects of strong Coulombic repulsion*.[116-117] Dimers of $GdmH^+/GdmH^+$ involving two arginines have also been implicated in several structure/function relationships, including the enhancement of passive cell-membrane penetration.[118-120] While Scheraga's evidences for the like-charged ion pair was derived from database searches,[116, 121] strong evidence was also recently obtained from X-ray absorption spectroscopy experiments.[122] Higher level quantum mechanical calculations also underscore the important role of water in stabilizing these like-charged $GdmH^+/GdmH^+$ dimers,[117, 123] and ab initio MDS suggest that the like-charg ion pairs are stabilized by amphiphilic behavior and van der Waals interactions.[124] Notably, cryo-IM-MS offers an unique technique that can report *direct* experimental evidence for hydrated, like-charged $GdmH^+/GdmH^+$ interactions.[122-125]

Recent cryo-IM-MS investigations of diammonium alkyl cations are most analogous to these studies.[104] Servage *et al.* showed evidence of a distinct unfolding transition that occurs over a small range of hydrating water molecules. For example, the transition from hydration by a single droplet to one droplet for each ammonium ion of 1,7-diammonium alkyl ion (H_3N^+-$(CH_2)_n$-NH_3^+;n= 7, 8, and 10) occurred over the range of 16-18 water molecules, whereas the transitions for 1,8- and 1,10-diammonium alkyl ions occurred at 18-20 and 21-24 water molecules respectively.[104] The unfolding transition occurs as a result of increasing Coulombic repulsion during the dehydration process. While it is surprising that the ions can be maintained within ~1 nm by so few water molecules, it is notable that the diammonium alkyl ions cannot escape each other, bound

by the carbon chain. Furthermore, the chain is hydrophobic and will protrude from the nanodroplet, while the hydrophilic -NH_3^+ groups remain within the droplet; it is unclear if the intermolecular interactions of the chain affects the stability of the ions in the droplets.

Although like-charged ions repel each other in vacuum, considerable theoretical work has shown that in bulk solution, two like-charged ions form distinct contact ion pairs (CIP) and solvent-separated ion pairs (SSIP).[126-128] CIPs have been observed in simulations in nanodroplets (which do not resemble bulk solution) with ~400 water molecules (**Figure 2.1**). These like-charge interactions have been identified between alkali

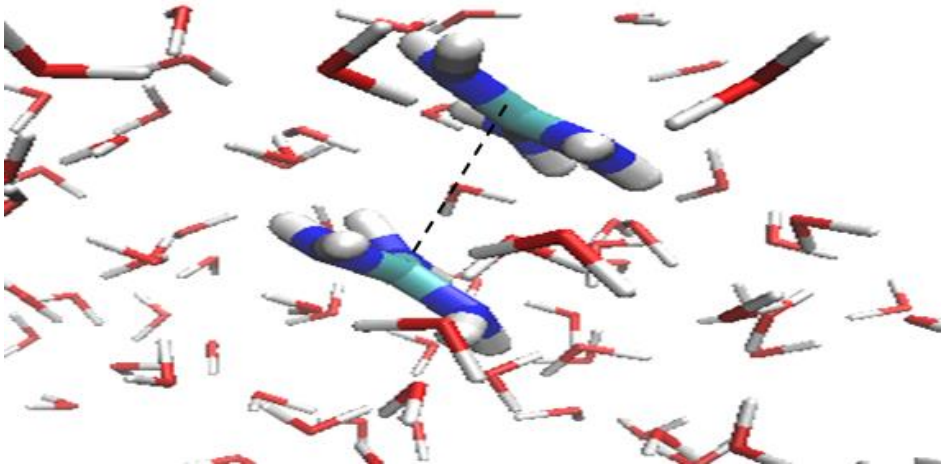

Figure 2.1. Blown up view of an evaporating droplet at 350 K containing 408 water molecules and two guanidinium ions, separated by ~3.5 Å. These ions separate and approach several times throughout the ~200 ns simulation.

metal ions and halogen ions and between active sites of biological macromolecules. As examples of solvent-separated ion pairs, Tabushi *et al.* showed a water-bridged, cation-cation pair in trypsin-inhibitor complex, while Brünger *et al.* presented evidence that water stabilized the positively charged active site of bovine pancreatic ribonuclease A.[129-130] Scheraga *et al.* detailed contact ion pairs in the like-charged interaction between surface

arginine residues.[116-117] Despite an abundance of theoretical and indirect experimental evidence of like-charged interactions, there has been little direct experimental evidence for isolated contact ion pairs of like-charged ions in water clusters or bulk water.[117-118, 121-124, 131]

In this section, it is interesting to compare the hydration structures of guanidinium and arginine. These hydration structures differ considerably given the flexibility of the hydrophilic regions of the arginine compared to the rigidity of the guanidinium ion. Furthermore, experimental evidence obtained by cryo-IM-MS of *hydrated* like-charged ion pairs of $GdmH^+$-$GdmH^+(H_2O)_n$ and $GdmH^+$-$H^+(H_2O)_n$ are detailed. The stabilizing interactions of these two complexes are discussed in the context of MDS.

2.2. Methods

2.2.1. Experimental

The instrumentation has been described in section **1.3.1**. Briefly, solutions of 200-400 µM GdmHCl, GdmHI, Guanidinium acetate, or 300 µM arginine were prepared in 18.2 MΩ, unless otherwise stated. Freeze-dried ions were generated by static ESI emitter tips (~3-5 µm outer diameter) and guided to a cold (80 ± 2 K) ion mobility drift tube.

2.2.2. Computational

Born—Oppenheimer MD simulations were performed on $GdmH^+$-$H^+(H_2O)_{18}$ and $GdmH^+$-$Na^+(H_2O)_{18}$ with the MD module of ORCA version 4.2.0,[132] equations of motion of the system were integrated with the velocity-Verlet algorithm at timestep of 0.5 fs by

collaborators Victor Kwan at the University of Western Ontario. The temperature of the system was maintained at 80 K with the Berendsen thermostat. The energy of the system at each timestep was calculated at the ωB97X-D3/def2-TZVP level with RIJCOSX approximation.[133-135] Geometric counterpoise method (gCP) was used to correct basis set superposition error.[136] Three runs were performed for each system and each run is 20 ps long.

VMD version 1.9.3 was used to analyze simulation trajectories and calculate hydrogen bonds.[137] Snapshots from VMD were optimized at the ωB97X-D /6-311++G** level of theory in Gaussian 16. Electric fields reported here were determined using Gaussian 16, using the DFT density, unless as specified as follows. A separate electric field calculation was performed to determine specific contributions from specified atoms, in **Figure 2.6**. For this calculation, partial charges were assigned according to the Merz-Singh-Kollman scheme, which were implemented in a MATLAB code to determine electric field strengths resulting from specific molecules or groups of molecules.

Noncovalent interactions were calculated with NCIPlot and visualized with VMD version 1.9.3.[137-138] Default parameters for wavefunction-generated NCIPlots fit the noncovalent interactions qualitatively well.

2.3. Results and discussion

2.3.1. Hydration of Guanidinium Ions

Figure 2.2 contains mobility arrival-time distribution (ATD) vs m/z plots of hydrated $GdmH^+(H_2O)_n$ and $ArgH^+(H_2O)_n$ ions. Abundant $GdmH^+(H_2O)_n$ cluster ions

range from n ~1-30, whereas $ArgH^+(H_2O)_n$ cluster ions for n > 50 are observed. Beauchamp *et al.* showed evidence that the hydrated ions are formed by stepwise elimination of single H_2O molecules from larger hydrated ions,[38, 61] and this appears to also be the case for $GdmH^+(H_2O)_n$ and $ArgH^+(H_2O)_n$ ions. In a recent study, Kim *et al.* reported MDS results that suggest that some water loss occurs by ejection of small neutral clusters from the nanodroplet.[139] For both $GdmH^+(H_2O)_n$ and $ArgH^+(H_2O)_n$ the ATD decreases as the number of water molecules decreases, forming smaller droplets with no change in the existing ion or droplet structure. This is the expected behavior for hydrated ions, where loss of H_2O is purely an evaporative process and is most apparent in the regions n = 1-3 for both ions. Regions of discontinuity, as observed for n = 5-10, are indicative of either changes in the size of hydrated ions owing to a change in the structure of the ion or changes in the orientation of the hydrating H_2O molecules. Because of the rather rigid structure of $GdmH^+$, these changes are attributed to the latter process. The water network transitions from a dome-like structure to a planar -like structure (structure **I**) for n = 6-9, as there is insufficient H-bonding to maintain the hemispherical network above the carbon atom. Instead of an abrupt transition from the interstitial NH_2 bonding to single-H-bonding with NH_2 at n = 9, it is more likely that the first hydration shell rearrangement occurs over the same dome-like to planar-like H-bond network transition. It appears H-bonding with the interstitial sites only becomes energetically favorable upon sufficient dehydration.

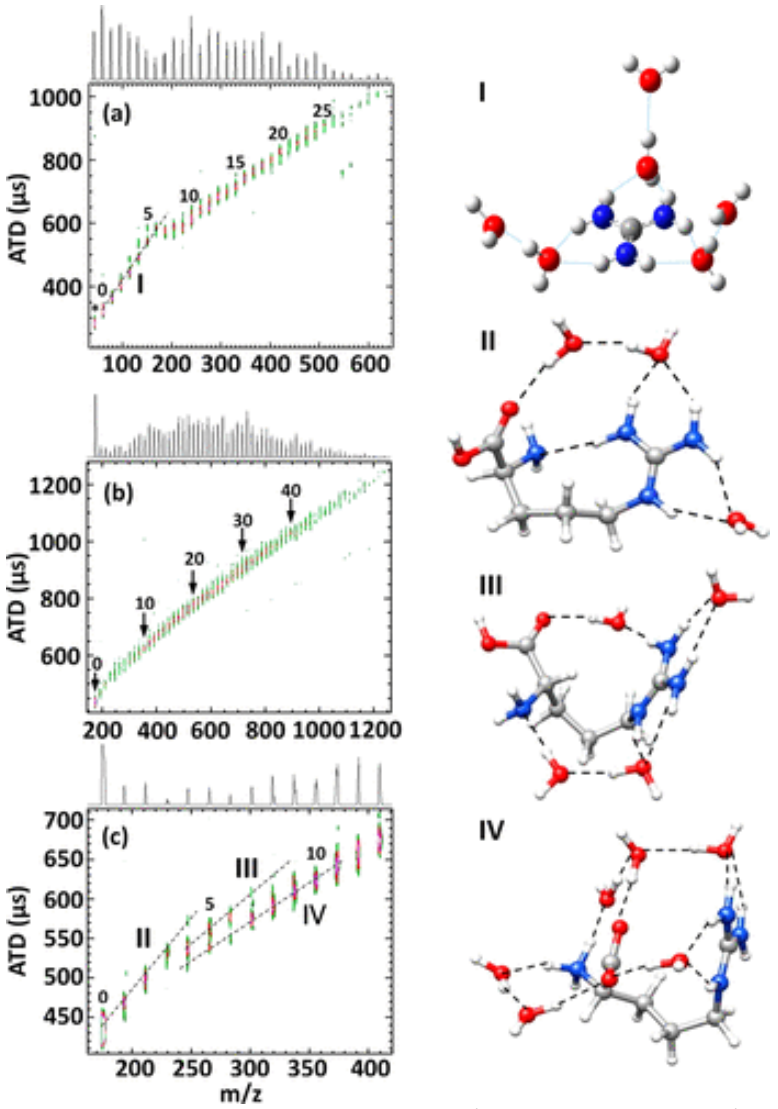

Figure 2.2. ATD vs m/z plots of (a) $GdmH^+(H_2O)_n$, (b) $ArgH^+(H_2O)_n$, and (c) $ArgH^+(H_2O)_n$ ions for n = 1–13 were obtained from solutions of 200 μM GdmHCl or 300 μM arginine solutions in 18.2 MΩ H_2O. Structure **I** shows a proposed structure populated by $GdmH^+(H_2O)_n$ ions where n = 6. (adapted from ref. 142) . Structures **II**, **III**, and **IV** are proposed structures for the ions that fall on the respective ATD trendlines in (c) (adapted from ref. 140. The peak labeled with an asterisk denotes a fragment carbocation.

It is interesting to compare the ATD vs m/z plots of $GdmH^+(H_2O)_n$ and $ArgH^+(H_2O)_n$. The ATD vs m/z in the regions n > 10 follow a single trendline, but the ATD for n = 4 is shifted downward relative to that for n = 5. Multiple ATD signals are detected for n = 4, 5, and 6; these shifts are highlighted by the dashed lines in **Figure 2.2c**.

These differences represent greater conformational diversity for the $ArgH^+(H_2O)_n$ ions, as previously suggested by Gao *et al.*[140] There is a salt bridging (SB) structure (**IV**) that is more compact and a charge solvated structure (CS) that is more extended (**III**). In addition, a third conformer family (**II**) was observed at n = 4 where limited hydration causes intramolecular charge solvation to dominate, and structure **III** transitions to **II**. Gao *et al.*

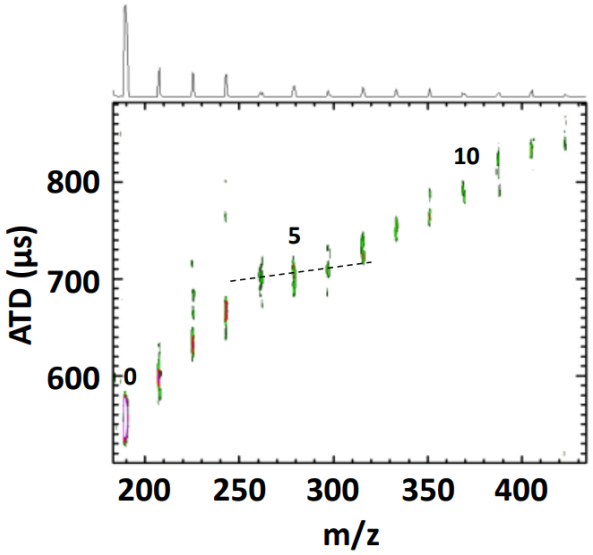

Figure 2.3. ATD vs m/z plot of $MeRH^+(H_2O)_n$ ions for n = 1-13 obtained from a solution of 300 µM methyl ester arginine in 18.2 MΩ H_2O and a tip with an outer diameter of ~3-5 µm. A dashed line shows a single transition in the hydrogen bonding network, similar to what is observed for the $GdmH^+(H_2O)_n$ series.

comment that the SB and CS structures become nearly isoenergetic at n = 7.[140] However, our data suggest the CS structure becomes dominant at n = 4, the CS and SB forms are nearly equal in abundance at n = 5-6, and the SB structure becomes dominant for clusters with 7 or more water molecules. To test the hypothesis that a proton is transferred from the N- to C- terminus, the pathway by which **IV** transitions to **III**, the methyl ester arginine ($MeRH^+(H_2O)_n$) was examined (**Figure 2.3**). The ATD vs m/z plot for $MeRH^+(H_2O)_n$ resembles that of $GdmH^+(H_2O)_n$, suggesting successful inhibition of the proton transfer.

Previous studies have described $GdmH^+$ ions as weakly hydrating owing to the low charge density; *i.e.*, the positive charge is delocalized over each of the $–NH_2$ groups.[141] Sharp *et al.* described $GdmH^+$ as having amphiphilic character, where the partially positively charged hydrophilic $–NH_2$ bind water strongly, but the carbon atom possesses hydrophobic character.[141] Heiles *et al.* argued that the strongest hydration occurs at small water cluster sizes, such as when $GdmH^+$ might be approaching or already in close contact with another molecule. They report the formation of the second hydration shell and a rearrangement of the first shell upon the addition of a fourth and ninth water molecule, respectively.[142] Understanding these strongly hydrated structures is important to the description of the binding interactions of $GdmH^+(H_2O)_n$; the solvation of $GdmH^+$ can be

altered by interactions from other groups such as in ion pair formation. Structure **II** shows how the $GdmH^+$ ion can be intramolecularly solvated while structure **IV** shows how the ion forms a solvent bridge with the C-terminus. The methyl ester arginine inhibits the latter interaction and does not form the more compact ion conformation in structure **IV**.

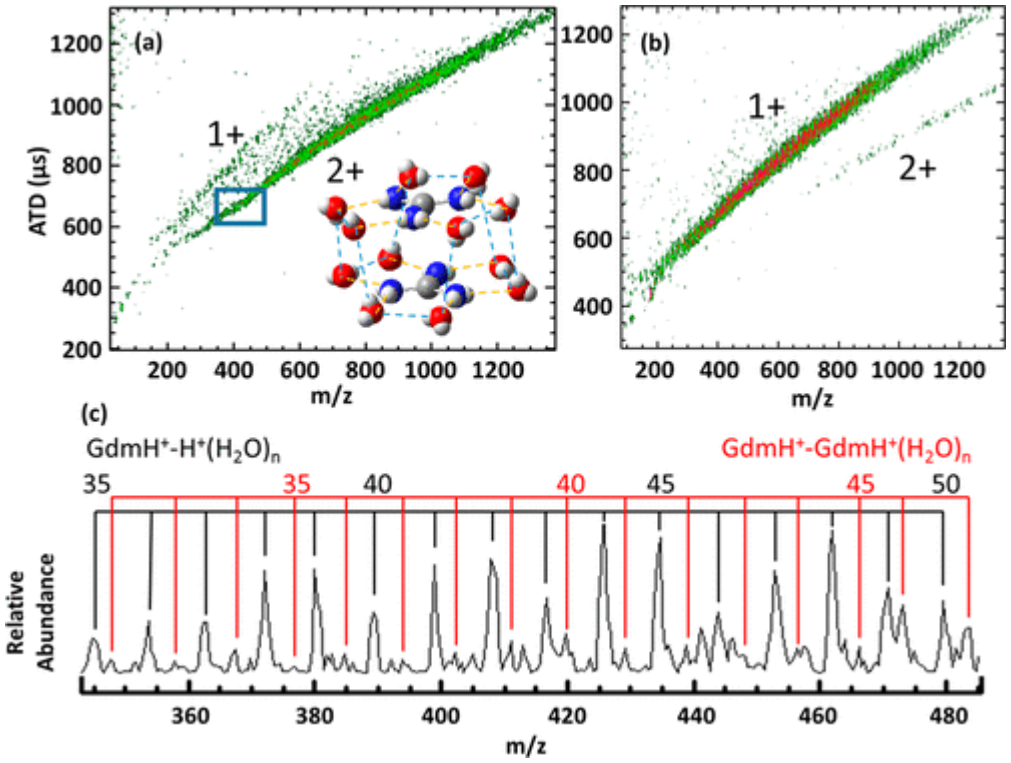

Figure 2.4. Two-dimensional contour plots of ATD vs *m/z* of (a) $GdmH^+(H_2O)_n$ and (b) $ArgH^+(H_2O)_n$ ions obtained from solutions of 400 μM GdmHCl in 0.1% formic acid or 300 μM arginine in 18.2 MΩ H_2O. A proposed structure of $GdmH^+$–$GdmH^+(H_2O)_{12}$ like-charged complex is shown in the inset; N–H---O and water–water hydrogen bonds are shown with orange and blue dashed lines, respectively. This structure is similar to that reported by Vazdar et al. in ref. 123. (c) Mass spectrum extracted from the region between *m/z* 340 and 485 showing hydrated like-charged ion pairs ($GdmH^+$–$GdmH^+(H_2O)_n$, red) and ($GdmH^+$–$H^+(H_2O)_n$, black).

2.3.2. Cryo-IM-MS of Doubly Charged Clusters

Figure 2.4 contains ATD vs m/z plots for 2^+ ions formed from solutions of (a) GdmHCl and (b) arginine. Because the abundances of doubly charged ions were low using small ESI emitter tip sizes (~3-5 µm outer diameter), these data were obtained using larger ESI emitter tip sizes (~15 µm outer diameter) and slightly higher drift tube pressures. These conditions favor formation of larger droplets, which increases the abundances of doubly charged droplets. The doubly charged ion region in **Figure 2.4a** contains both hydrated $GdmH^+$-$GdmH^+(H_2O)_n$ and $GdmH^+$-$H^+(H_2O)_n$. The individual ion signals in the mass spectrum (**Figure 2.4c**) are sufficiently resolved to allow for assignment of the hydrated 2^+ ions, ranging from approximately 15 to over 130 (165-1200 m/z) water molecules. The signal for 2^+ ion clusters for both $GdmH^+$- $GdmH^+(H_2O)_n$ and $GdmH^+$-$GdmH^+(H_2O)_n$ begins to decrease in abundance at n = ~55 and have completely dissociated to 1^+ clusters by n = 15-20. While peaks with m/z corresponding to $ArgH^+$-$ArgH^+(H_2O)_n$ and $ArgH^+$-$H^+(H_2O)_n$ complexes were observed, the 2^+ ion abundances in the spectrum for the arginine solution are very weak, and the exact masses were not able to be assigned. Kubíčková *et al.* showed that the stabilizing interactions of $GdmH^+(H_2O)_n$ that favor formation of $GdmH^+$-$GdmH^+$ complexes are not detected for other positively charged ions.[131] Similarly, doubly charged ions in ESI mass spectra of solutions of ammonia, specifically NH_4^+-$NH_4^+(H_2O)_n$ clusters, were not observed (**Figure 2.5)**. Thus,

this data provides additional evidence that the like-charge guanidinium ion pairs are not artifactual, and the ion pairing behavior observed is specific to the guanidinium ions.

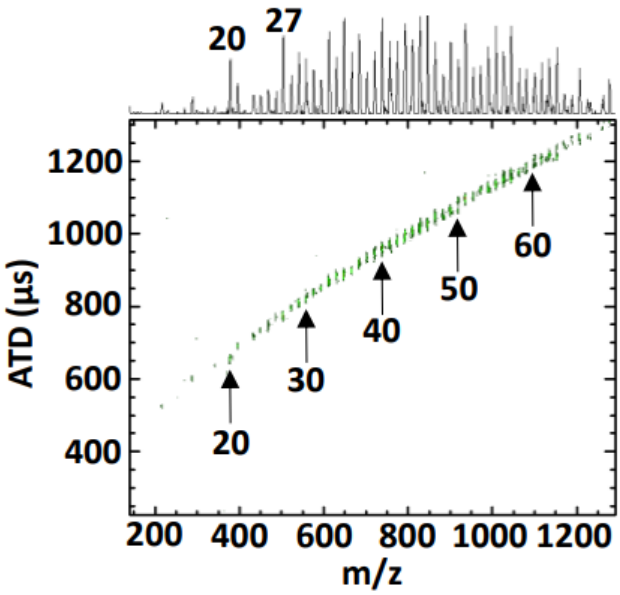

Figure 2.5. ATD vs m/z plot of $NH_4^+(H_2O)_n$ ions obtained from a solution of 400 µM NH_4Cl in 18.2 MΩ H_2O and a tip with an outer diameter of ~15 µm. All ions contained in this plot carry a charge of +1. Ions that carry a +2 charge would fall on a different trendline. See **Figure 2.4** for comparison. The same experiment in 0.1% formic acid was performed, with similar results, but the spectrum becomes difficult to resolve due to the presence of $H^+(H_2O)_n$ clusters. Notably, no 2^+ clusters were detected in either case. Magic number clusters at n = 20 and 27 are marked.

The dehydrated (n = 0) $GdmH^+$-$GdmH^+(H_2O)_n$ like-charged ion pair is not observed in **Figure 2.4a**; however, low abundance signals for the like-charged ion pair are observed for $n \geq 15$. This observation is consistent with results reported by Vazdar *et al.*[123] Vazdar *et al.* used ab initio calculations to show that the formation of parallel, stacked $GdmH^+$- $GdmH^+$ like-charged ion pairs requires at least 12 water molecules, and that the stability of the complex increases as the number of water molecules increases.[123] The surrounding water molecules provide essential enthalpic benefits through an extended H-

bonding network, which affords charge solvating interactions that overcome entropic costs and reduce Coulombic repulsion. In addition, chloride anions located on the periphery of the like-charged ion pair have been predicted to stabilize the complex,[143] but chloride adduct ions were not observed experimentally. To test whether Cl^- ions are involved in the formation of the ion pair and being lost as HCl,[144] investigations of the hydration of guanidinium sprayed from guanidinium acetate solution observed similar like-charged ion pairs starting at n > 11. Vazdar *et al.* also predicted a T-shape complex as a local minimum; while the 2^+ water clusters display considerable heterogeneity in their mobilities, no confident structural assignments can be made currently.[123] However, given that 6-7 water molecules per $GdmH^+$ hydrates in a nearly planar fashion (structure **I**),[77] it is likely that the $GdmH^+$-$GdmH^+(H_2O)_n$ like-charged contact ion pair exists in a stacked, parallel structure similar to that reported by Vazdar *et al.* for low levels of hydration.[123] Regardless, typical studies on $GdmH^+$-$GdmH^+$ have suggested the complex is stable due to favorable intermolecular interactions between the $GdmH^+$ ions acting as a counterforce to Coulombic repulsion, but it is apparent that solvent bridging water must be accounted for in the stabilization of the ion pair.

A similar 2^+ trendline was observed for arginine solution, but the relative abundances of the ions are very low and the peak resolution is not sufficient for high confidence assignments. These differences probably arise owing to alternative mechanisms for hydrating the $ArgH^+$ ions. Specifically, as the numbers of hydrating water molecules increase, *i.e.* for n >6, the C-terminus of the molecule can take on a negative charge by forming an ion pair, COO^--$(H^+(H_2O)_n$, or through formation of a salt bridge

with the N-terminus. In either case, these competing mechanisms of hydration might disrupt the arrangements of water molecules that favor formation of the hydration network necessary to bridge two nearby $GdmH^+$ moieties. These interactions may explain why $ArgH^+$-$ArgH^+(H_2O)_n$ complexes are only observed at larger water cluster sizes ($n > \sim25$).

The dependence for formation of the like-charged ion pair on a solvent bridge is supported by recent results invoking solvent bridges in the solvation of both charge groups in alkyl diammonium cations and the noncovalent ubiquitin dimer.[79, 101, 104] Additionally, the $GdmH^+$ solvent bridging provides insight into how two arginine residues come together to form solvation ion pairs.[116-117] The observation of a solvent bridge that forms around the hydrophobic region of $GdmH^+$ is similar to results reported for the hydrated, noncovalently bound ubiquitin dimer, where dimer dissociation does not occur until late in the desolvation process. The formation of the noncovalent ubiquitin dimer was attributed to interactions involving the I44 hydrophobic patch and to solvent bridging involving the positively charged arginine side chains located near the I44 hydrophobic patch.[101] The similar hydrophobic core and hydrophilic peripheral sites in both ubiquitin and guanidinium ion pairs underscore the potential importance of such binding "hot spots" and provide a simple model system to gain additional insight into these effects on the peptide/protein scale. While it is well-known that hydrophobic patches provide the thermodynamic impetus for dimerization, these data support substantial binding forces resulting from solvent bridges which must be disrupted prior to dissociation.

2.3.3. Stabilizing Interactions of Doubly Charged Droplets

To further probe the stabilizing interactions within the ESI droplet, which for small molecules is largely dependent on the electric field strength, MD were performed. The IEM (described in **1.2.1**) generally ejects ions in droplets when the field strength at the surface of the droplet exceeds 1-3 V/nm.[30] Field strength can be determined by **equation 2.1**,

$$\mathbf{E^* = ne/(4\pi\epsilon_0 r^2)} \qquad \mathbf{(2.1)}$$

where n is the number of charges, *e* is the charge of a proton, $\boldsymbol{\epsilon_0}$ is the free permittivity of space, and r is the radius of the droplet, or distance between point charges. The field strength resulting from two guanidinium ions is ~9 V/nm, considerably above the IEM critical limit. However, it is worth noting several assumptions of this value. The distance between the ions is merely a static representation of the electric field, which is more realistically experiencing very large fluctuations (due to the very small distance between ions and the field dependency on distance) over time. It is also necessary to consider the nearby water interactions.

The electrostatic potential (ESP) fitted partial charge and electric fields on $GdmH^+$-$H^+(H_2O)_{18}$ and $GdmH^+$-$Na^+(H_2O)_{18}$ droplets were calculated *ab initio.* One proton was localized on the guanidine due to its high basicity. Similarly, Brugé *et al.* have shown that a proton is localized on the ammonium, rather than delocalized as ammonia and H_3O^+.[145] These electric field calculations represent simplified *static* structures. There also is no multipole expansion, which may be necessary to consider. Nonetheless, these crude calculations qualitatively demonstrate both the high electric field generated by the cations and the opposite electric field generated by the high dielectric water molecules. The water plays a critical role in opposing the high electric fields generated by each cation.

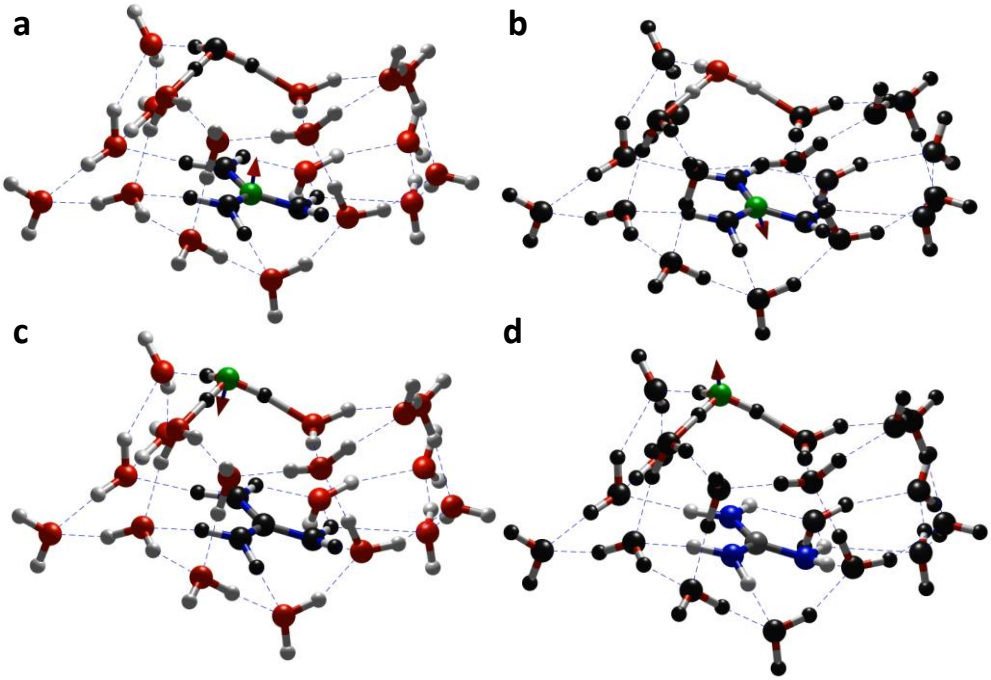

Figure 2.6. The electric fields at (a and b) the C+, (c and d) the hydronium ion O^+, and the Na^+ atom locations, resulting from the (a and c) surrounding water network and (b and d) opposite ion were determined. The green atom represents the location the electric field was calculated at, and the arrow shows the unit vector of the electric field. Black atoms were excluded from the electric field calculation.

Table 2.1. The electric field originating from the bolded portion of each complex is determined for each column of atoms. The electric field is only determined in these cases for the field in the axis between the two ions in each complex and is lower than the total field exhibited. The letter code for each case corresponds to the letter code in **Figure 2.6**. Positive numbers represent electric fields directing an ion away from the opposing ion (outwards/away from the droplet), while negative numbers represent fields directing an ion towards the opposing ion (inwards/towards the droplet).

Field of \On	C^+	H_3O^+	Na^+
$GdmH^+H_3O^+$**$(H_2O)_{18}$**	-7.24[a] V/nm	-10.9[c] V/nm	-
$GdmH^+$ $H_3O^+(H_2O)_{18}$	-	4.48[d] V/nm	-
$GdmH^+$**H_3O^+(**$H_2O)_{18}$	7.02[b] V/nm	-	-
$GdmH^+Na^+$**$(H_2O)_{18}$**	0.23 V/nm	-	-6.08 V/nm
$GdmH^+$ $Na^+(H_2O)_{18}$	-	-	2.11 V/nm
$GdmH^+$**Na^+**$(H_2O)_{18}$	3.04 V/nm	-	-

Since $GdmH^+$-$H^+(H_2O)_n$ does not have any hydrophobic interactions to stabilize it, it was surprising to observe it in such high abundance relative to the GdmH-$GdmH^+(H_2O)_n$ ions; it was hypothesized that the proton was better able to delocalize the charge amongst the water network in the former ion pair. However, it is not straightforward to compare the two complexes, since $GdmH^+$ has several additional hydrogens available for delocalization via H-bonding. Instead, H_3O^+ was compared to a point charge with no H-bonding opportunities, Na^+. The number of H-bonds maintained in $GmdH^+$-$H^+(H_2O)_{18}$ was compared to $GdmH^+$-$Na^+(H_2O)_{18}$. The hydronium complex maintained an extra ~3.6 H-bonds over 5 ps relative to the sodiated complex, corresponding to a ~1 eV more stabilizing H-bond environment. The additional H-bonding delocalizes the charge better than in the case of sodium, and may explain the much higher relative abundance of the $GdmH^+$-$H^+(H_3O)^+$ complex relative to $GdmH^+$-$GdmH^+(H_2O)_n$.

Van der Waals interactions have also been used in support of the $GdmH^+$-$GdmH^+(H_2O)_n$ complex.[123] In **Figure 2.7**, attractive van der Waals interactions are shown as green surfaces for $GdmH^+$-$H_3O^+(H_2O)_{18}$ using NCIPlot. Additionally, the water network forms quadrupolar interactions in response to $GdmH^+$, stacking opposite charges. Unlike the $GdmH^+$-$GdmH^+$ complex, there is no way to bury the hydrophobic region, and it appears that it does not play an important role in stabilizing the $GdmH^+$-$H_3O^+(H_2O)_n$ complex here.

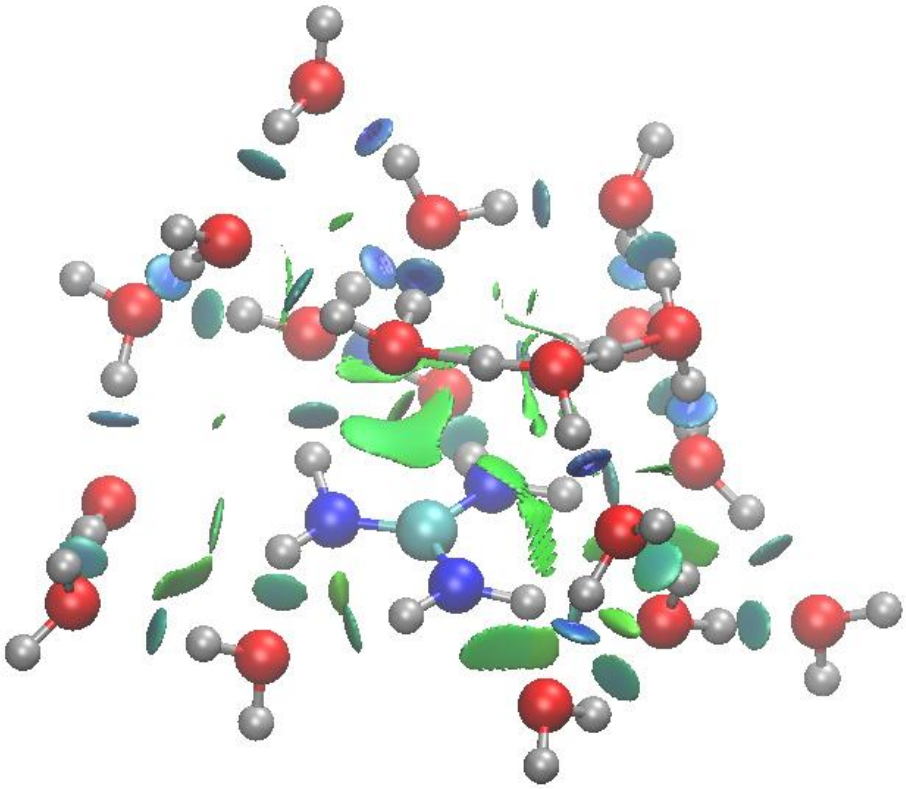

Figure 2.7. Van der Waals and H-bonding interactions are shown for $GdmH^+$-$H_3O^+(H_2O)_{18}$ by green and teal surfaces, respectively.

2.3.4. Multiply Charged Water Clusters in Larger Peptide Systems

The formation of charged droplets with excess charge has also been observed for bradykinin (RPPGFSPFR; BK), which contains two, separated arginine residues, which may increase the ability to support the extra charge. It is clear from the mass spectrum in **Figure 2.8** that the BK^{2+} species dominates, and it is well within the expected charged droplet limits. However, there is an extra hydrated species that falls below the BK^{2+} trendline. Extraction of part of that species is shown in **Figure 2.8b**, revealing that there is a hydrated BK^{3+} species. This $BK^{3+}(H_2O)_n$ series does not exhibit fewer than about 40 molecules of water adducted. Although this suggests that the proton is mobile, and part of the water network, rather than isolated on one of the three possible basic sites, the presence of dehydrated BK^{3+} does clearly indicate that the proton can be isolated on a basic site. Note that the proton location and ion size (numbers of waters adducted) are key to understanding the formation of this ion, and in turn the late-stage ESI mechanism. Recall that in CRM, described in **1.2.1**, the charge a droplet can maintain depends on the size of the droplet, the number of charges, and the surface tension of the droplet. The charge remaining in an evaporating droplet then eventually settles onto the analyte. The Rayleigh limit of a droplet can be determined with a few assumptions: (i) the droplet is spherical, (ii) the density of the peptide and water molecules are 1 g/L, and (iii) the surface tension is that of water, ~0.72 N/m. Although these are not very good assumptions for a nanodroplet at 80 K, it is notable that the failure in these assumptions should only serve to increase the Rayleigh limit and therefore the amount of charge a droplet can maintain. The BK^{3+} ion with 40 water molecules adducted corresponds to approximately 90% of the

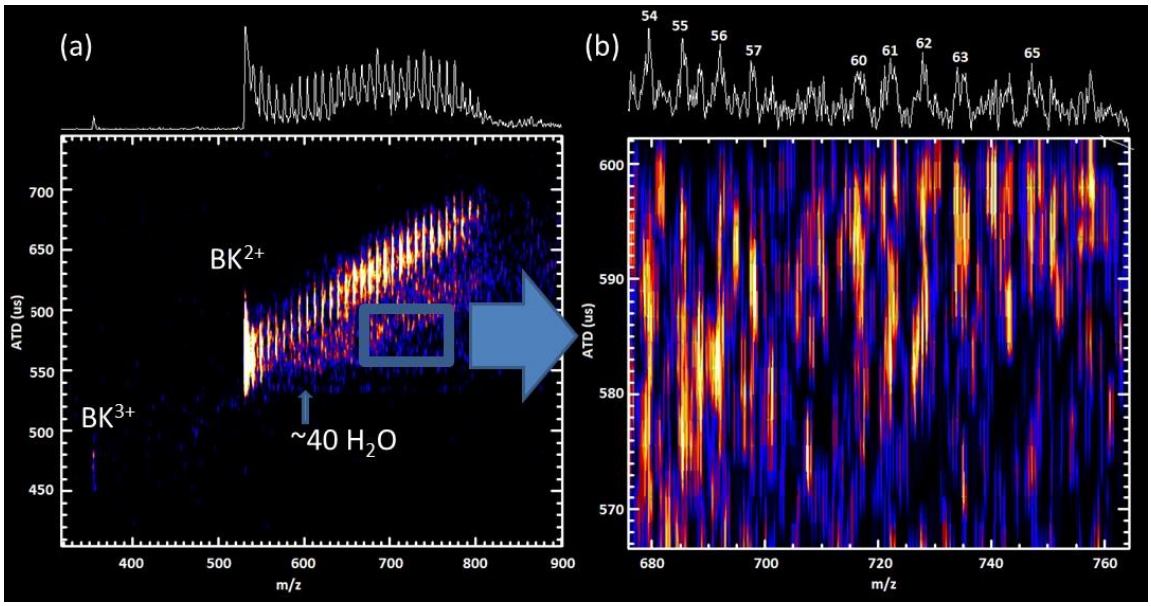

Figure 2.8. (a) ATD vs m/z plot of bradykinin (BK) and (b) an extracted ATD vs m/z plot of the highlighted region, revealing m/z peaks separated by 6 m/z, corresponding to hydrated BK^{3+} ions. The mass spectrum is above each plot and the number of water molecules adducted to BK^{3+} is above each peak.

Rayleigh charge predicted under the given assumptions; BK^{3+} hydrates appear to follow the Rayleigh limit and CRM. Furthermore, the $BK^{2+}(H_2O)$ trendline grows in abundance at n ~ 30-33 waters, supporting the charge reduction of the droplet in this size regime. The ability for a droplet to take on extra charge appears limited to guanidinium-containing analytes, but future work that can delineate between charge effects on the droplet, and specific charged residue effects will be necessary. Briefly, mutant studies of R1K, R9K, and R1,9K would be good initial analytes of interest, but this future direction is expanded on in section **5.2**.

2.4. Conclusions

The $GdmH^+(H_2O)_n$ H-bonding network undergoes a structural transition from n = 6-9, in agreement with the transition from a dome-shaped cluster to a more planar cluster.

Conversely, the structure of $ArgH^+ (H_2O)_n$ behaves quite differently; at large values of n, these ions have a more solution-like structure that is best described as a zwitterionic salt-bridging structure. The charge sites on the zwitterionic termini of the arginine residue remain stable until only 5-6 water molecules remain, at which point the ion transitions to a gas-phase charge-solvating structure. A second transition was observed, which was attributed to a transition towards intramolecular solvation of the $GdmH^+$ moiety by the N-terminus. This intramolecularly solvated ion conformation becomes favored when there is very little hydration, $n < 5$.

The first direct experimental evidence for solvated like-charged guanidinium complexes ($GdmH^+$-$GdmH^+(H_2O)_n$) were reported; these complexes were stabilized by exceptionally few numbers of water molecules, $n \sim 15$. It appears likely that two $GdmH^+$ ions stack parallel to one another, since the hydrated guanidinium ion is nearly planar for n = 6-7, and the charge is delocalized across each $–NH_2$ group. Each of the guanidinium ions is solvated by 6 water molecules, and the remaining ~3 water molecules serve to bridge the $–NH_2$ groups. However, as the number of water molecules increases, the hydrated like-charged complex takes on a number of alternative structures. The enthalpic benefit provided by an H-bonding network bridging the two $GdmH^+$ ions rationalizes how like-charged complexes have been observed between arginine residues and in theoretical studies of guanidinium ion pairs.

The unexpected observation of a heteroion pair involving hydrated H_3O^+ and $GdmH^+$ was also reported. The like-charged $GdmH^+$-$GdmH^+$ ion pair is stabilized by the network of bridging water molecules (H-bonding), quadrupole-quadrupole, hydrophobic,

and van der Waals interactions,[122, 124] whereas the stabilizing interactions for the like-charged $GdmH^+$-$H^+(H_2O)_n$ complex are limited to H-bonding. Thus, the relatively high abundance of the latter is an unexpected result. This suggests that the heteroion pair must receive similar enthalpic benefits from structuring the hydration network, and that this may be the dominant stabilizing interaction. Furthermore, the effects of Coulombic instabilities of the $GdmH^+$-$H^+(H_2O)_n$ complex may be minimized by rapid shuttling of the proton via the Grotthuss mechanism, effectively dispersing the charge density. The diffuse charge distribution and unique water-structuring capability of the $GdmH^+$ ion play key roles in formation of both the homoion and heteroion pairs observed here. These requirements rationalize the absence of like-charge complexes involving point charge species, specifically NH_4^+ and H^+ ions.[131] Lastly, it is important to recognize that the nanodroplet environment is not an accurate model for bulk water; thus the guanidinium ion pairs may be unique to confinement effects of the nanodroplet, or its generation via ESI. The diffuse charge distribution and unique water-structuring capabilities of the $GdmH^+$ ions may be relevant to its actions as a protein denaturant. The structuring observed here in the confined nanodroplet may also have parallels to confinement near the protein surface.[146]

Guanidinium-containing analytes accumulating large numbers of charges is related to ESI. In particular, it is interesting to note that hydrated $GdmH^+$-$GdmH^+$ and $GdmH^+$-H^+ species should be formed via IEM, while hydrated BK^{3+} ions appear to meet the Rayleigh limit criteria of CRM. In the former, it has been shown that $GdmH^+$ forms stacked ion pairs in nanodroplets with a few hundred water molecules. These ion pairs are

likely ejected in the same hydrated droplet when the field strength is sufficiently high and are maintained by an opposing electric field generated by the nearby water network. The new experimental data presented here issues a challenge to MDS: the stabilization of like-charged ion pairs by hydration is no longer in question; instead, how are these highly coulombically charged nanodroplets formed via ESI? The transition for BK^{3+} to BK^{2+} is more unusual, since there is an intermediate region with little to no hydration for BK^{3+}. The formation of BK^{2+} appears to be driven by a charge reduction reaction involving the loss of several water molecules. The formation of dehydrated BK^{3+} with limited hydrated intermediates must occur from the inhibition of this charge reduction reaction. Loss of interconnected waters may begin to occur near the Rayleigh limit due to limited hydration. The protonation sites would become effectively trapped and unable to be deprotonated, especially if the few remaining waters are localized on the arginine groups, competing with the basic guanidinium sites. Although the precise mechanism cannot fully be accounted for by the crude structural information here and will benefit from additional structural characterization, the cryo-IM-MS nonetheless provides an unprecedented experiment to probe late-stage ESI.

3. ACCESSING COLLISSION CROSS SECTION ON THE CRYO-IM-MS TO TRACK THE SOLUTION TO GAS-PHASE STRUCTURAL EVOLUTION OF 4-AMINOBENZOIC ACID*

3.1. Background

The protonated 4-ABAH$^+$ ion is an excellent example of a system where potential charge carrying sites are directly coupled to the local solvent environment. Tian and Kass showed that 4-ABAH$^+$ protomers were dependent on the solvent used during ESI; more protic solvents yielded higher relative abundances of the gas-phase O-protomer, while the solution phase N-protomer was preferred in aprotic solvents.[96] The experimental evidence supports a mechanism where the ionizing proton shifts its location from the solution-favored amine group (N-protomer) to the carboxylic acid in the gas phase (O-protomer). Subsequent studies noted that the N-protomer was observed with as few as 6 water molecules still adducted.[78] This proton transfer mechanism assumes the presence of a solvent bridge, which involves many sequential proton transfers between water molecules, that is, the Grotthuss mechanism.[147] Protic solvents exploit this proton relay system and readily transfer the proton via the water network to the O-protomer upon dehydration.[78, 98, 148]

---

* Reprinted with permission from Hebert, M. J. and Russell, D. H., Tracking the Structural Evolution of 4-Aminobenzoic Acid in the Transition from Solution to the Gas Phase. *J. Phys. Chem. B,* **2020,** *124* (11), 2081-2087. DOI: 10.1021/acs.jpcb.9b10576.

CCS provides valuable information about the size, shape, charge, and relative interaction potentials of analytes with the drift gas. Experimental CCS values are often used to limit the number of candidate structures generated by MDS. Consequently, considerable effort has gone into generating accurate theoretical CCS values and experimental calibrant libraries using a variety of drift gases.[149] However, due to the cryogenic temperatures employed and weakly bound water interactions, structural information obtained with cryo-IM-MS has thus far been limited to analyzing variations in ATD trends in the context of the current literature. Here, the linear relationship between ATD and CCS for a series of hydrated ions (*e.g.* 4-ABAH$^+$$(H_2O)_n$) is used to calibrate for cryo-IM-MS CCS.[150] Theoretical CCSs were used to calibrate experimental ATDs for accurate CCS determination of hydrated gas-phase ions, thereby reducing the number of candidate structures and simplifying structural identification.

Here, cryo-IM-MS is utilized to monitor changes in the conformers that occur upon stepwise desolvation of 4-ABAH$^+$$(H_2O)_n$ ions. It is interesting to consider how separation of the two protonation sites affects hydration, particularly the formation of a water bridge, which may be key for intramolecular proton transfer. Low capillary temperatures and aprotic solvents are reported to inhibit the Grotthuss-type proton transfer;[96, 98] however data reported here are more consistent with a mechanism whereby acetonitrile (ACN) stabilizes the $–NH_3^+$ group, inhibiting proton transfer to the -COOH group. Nitrogen drift gas also inhibits proton transfer, again by stabilizing the $–NH_3^+$ group relative to helium drift gas.

3.2. Methods

3.2.1. Experimental

Acetonitrile, 2-aminobenzoic acid (>98%), 3-aminobenzoic acid (>98%), and 4-aminobenzoic acid (>99%) were purchased from Sigma-Aldrich and used without further purification. Solutions were prepared in 0.1% formic acid by dissolving 4mM ABA in either water or water/ACN (49.9/50%) and 0.1% formic acid. Solutions were nanosprayed from gold-coated borosilicate capillaries (OD < ~5 μM) into a homebuilt cryo-IM-MS, which was described in section **1.3.1**. For the studies described here, either nitrogen or helium drift gases were used (99.999% purity). Experiments employing He drift gas were performed at temperatures of 80 ± 2 K, whereas experiments employing N_2 drift gas were limited to 96 ± 2 K. Drift gases are passed through a gas purifier (Hammond Drierite Co. 27068) to ensure that contaminating water vapor is <5 ppb. Ion mobility ATDs were iteratively smoothed with the Savitzky-Golay filter in MATLAB and fitted to unconstrained Gaussian peaks with peakfit.m v 9.4. ATD versus m/z plots were otherwise generated with Interactive Data Language (IDL) v6.1 by Research Systems Inc.[151] The ion pulse gate width for N_2 drift gas was increased to 36 μs from 24 μs due to low ion signal. An electric field of 9.40 V/cm was applied for both drift gases.

3.2.2. Computational

Monte Carlo Multiple Minimum (MCMM) conformational searches were performed using MacroModel 9.1 (Schodinger, Inc. Portland, OR). A minimum of 2000 conformations were generated per degree of freedom (number of molecules + number of

torsions) for each cluster. An MMFFs force field with explicit water molecules and extended force fields were used. Structures were minimized with 5000 steps to 0.05 threshold convergence. Lowest energy structures were subsequently geometry- and energy-optimized using the 6-311++G** basis set and ωB97X-D functional in Gaussian 16. The ωB97X-D functional was used due to its ability to describe the hydration surrounding 4-ABAH$^+$ and, more generally, systems in which H-bonding plays an important role.[78] Electrostatic potentials were calculated using the Merz-Singh-Kollman scheme in Gaussian 16. Electrostatic potentials are necessary to determine ion-induced dipole effects, which affect the CCSs of ions.

Optimized structures were submitted to MOBCAL at 83 K to determine CCS in helium. The default MOBCAL value for the polarizability constant of helium was used, 0.204956 x 10^{-30} m^3. Standard deviations of the CCS calculations were determined by MOBCAL.[92] The interactions of the drift gas play an important role in CCS calculation. CCSs in N_2 drift gas were not determined.

3.2.3. CCS Calibration in Helium

Typically, 1/V plots are used to determine the time spent outside the drift tube and the exact gas density. These variables can subsequently be plugged into the Mason-Schamp equation to determine CCS. However, the weakly bound water molecules only survive under a small range of drift fields (see **Figure 1.5**).[60] Instead, theoretical CCSs are combined with the Mason-Schamp equation[150] to calibrate simultaneously an unknown gas density and time spent outside of the drift tube (*vide infra)*. These calibrations are

limited to a small range of hydration; that is, separate calibrations for n = 0-6 and larger values of n will be required as the ions experience considerably different size/shape effects.[152-153]

$$K = \frac{L^2}{U(t_{obs} - t_0)} \quad \textbf{(3.1)}$$

The mobility (K) of an ion can be experimentally defined (**equation 3.1**), where L is the length of the drift tube, *U* is the applied voltage drop between the front and back of the drift tube, t_{obs} is the centroid of the observed arrival-time distribution, and t_0 is the time spent outside of the drift tube.

$$K = \frac{3\sqrt{2\pi/\mu k_B T}}{16} Q N^{-1} \Omega^{-1} \quad \textbf{(3.2)}$$

The mobility of an ion can also be described by **equation 3.2**, where μ is the reduced mass of the drift gas and analyte, k_B is the Boltzmann constant, *T* is the temperature, *Q* is the charge of the ion, *N* is the number density of the drift gas, and Ω is the CCS of the ion. Substituting **equation 3.1** into **equation 3.2** and combining the known values into the term *A* yields **equation 3.3**. Using **equation 3.3**, the theoretical CCS are plotted against the experimental ATDs for *n* = 0–5, effectively assigning each ATD to a CCS. A linear regression is then used to extrapolate the *n* = 6 CCS, and the protomer form can subsequently be determined by comparing the theoretical CCS of each protomer with the calibrated CCS from the linear regression at *n* = 6.

$$t_{obs} = NA + t_0 \quad \textbf{(3.3)}$$

Two other useful parameters, the number density, *N*, and time spent outside the drift tube, t_0, are also determined. The uncertainty from a linear least squares calibration

was estimated from the square root of the variance in *A*, var(*A*), given by **equations 3.4 and 3.5**.[154]

$$var(A) = [s(t_{obs})/N]^2 \quad \textbf{(3.4)}$$

Here, $s(t_{obs})$ is the standard deviation (square root of the variance, s_{tobs}, A^2) of $t_{obs}(A)$. The square root of the variability in *A* yields the uncertainty in the calculation, $u(A)$.

$$u(A) = \sqrt{var(A)} \quad \textbf{(3.5)}$$

Notably, there is some uncertainty that must be propagated from the *A* term according to **equation 3.6** when the uncertainty in **equation 3.5** is sufficiently small, less than ~2%. The two uncertainties can then be combined to determine total uncertainty.

$$u(A, A_i) \approx \frac{u(A_i)}{n} = A_i \frac{\sqrt{(0.5\,\frac{u(T)}{T})^2 + (\frac{u(U)}{U})^2 + (\frac{u(slope)}{slope})^2 + (2\frac{u(L)}{L})^2 + (\frac{u(CCS)}{CCS})^2)}}{n} \quad \textbf{(3.6)}$$

Here, *n* represents the number of A_i values used in the calibration.

3.3. Results and Discussion

3.3.1. Hydration of $ABAH^+$

It has been emphasized before that the hydration observed in cryo-IM-MS is the result of dehydration of nanodroplets generated by nESI as they undergo the solution to gas phase transition.[38, 60, 93, 155] The mechanism differs from condensation experiments, in which water vapor is placed in a chamber and condenses onto dehydrated gas-phase ions.[62, 64-68, 94] In this case, if cool conditions are maintained, ideally the transition from the N-protomer to O-protomer can be examined as an ESI phenomenon, rather than the

reverse process that occurs during hydration experiments. Importantly, hydrating water molecules are extremely sensitive to the vacuum and capillary temperature of the ion

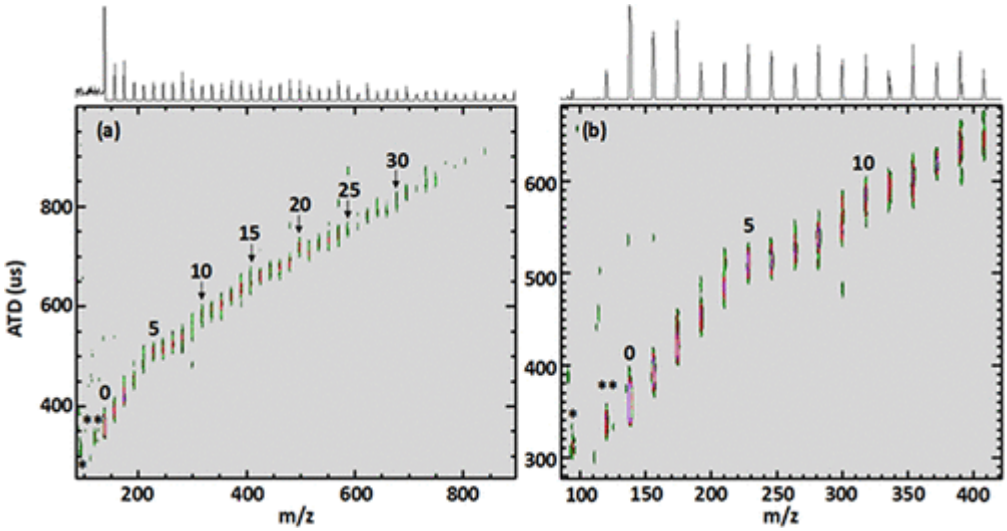

Figure 3.1. ATD vs m/z plots of 4-ABAH$^+$$(H_2O)_n$ sprayed from 0.1% formic acid with helium drift gas at a heated capillary temperature of 330 K. Panel (b) is an expanded plot of panel (a). Asterisk denotes 94 *m/z* (CO_2 loss) and double asterisk denotes 120 *m/z* (H_2O loss) fragments (refs. 78, 96-99, 156). The mass spectrum is located above each plot.

source,[60, 91, 100-101, 155] the electric field strengths in the drift tube,[60] and the drift gas (*vide infra*).

Figure 3.1 contains ATD vs m/z plots of the hydrated 4-ABAH$^+$$(H_2O)_n$ ions formed during nano-ESI-MS. The change in ATD for 4-ABAH$^+$$(H_2O)_n$ decreases monotonically for n ~ 10-30. There appear to be two inflection points, one at n = 20, and another at n ~5-9. The mobility transition for n = 5-9 occurs where the protonation site and hydration structures have been predicted to shift from a more solution-phase-favored, well-hydrated N-protomer ($n \geq 6$) to a more gas-phase-favored, dehydrated O-protomer.[78] For 4-ABAH$^+$$(H_2O)_n$, at n = 20, the ATD is shifted to longer ATDs, which suggests a change in the overall conformation of the hydrated ion cluster, the surrounding water, or

both. Water clusters are known to form magic number cluster structures at n = 20, with the ammonium ion interacting at the surface of the nanodroplet.[86] However, this would

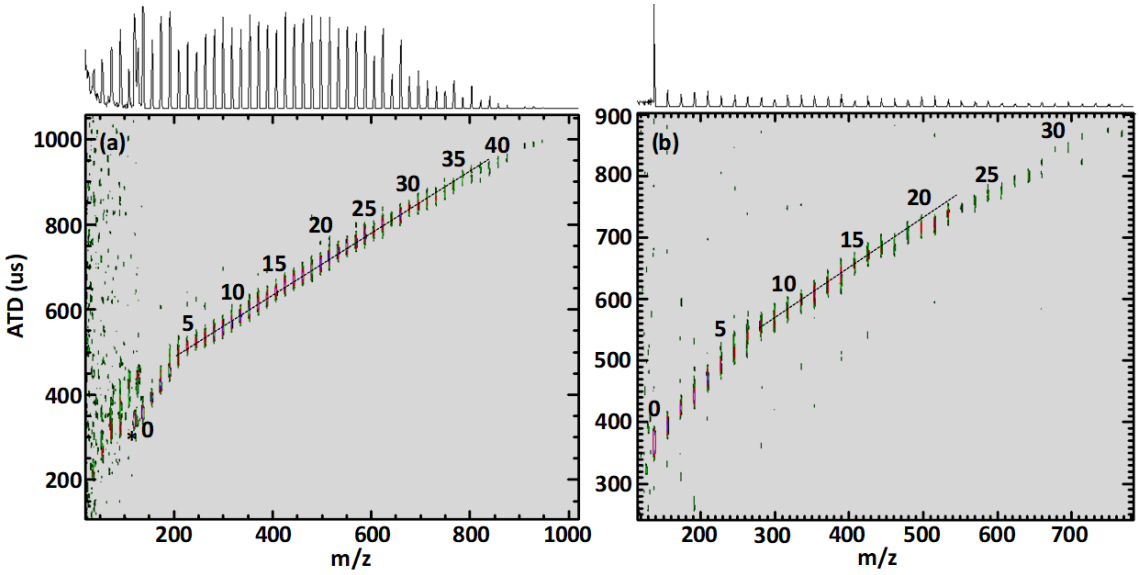

Figure 3.2. ATD vs m/z plots of **(a)** 2-ABAH$^+$(H$_2$O)$_n$ and **(b)** 3-ABAH$^+$(H$_2$O)$_n$ sprayed from 0.1% formic acid with helium drift gas at a heated capillary temperature of 330 and 303 K, respectively. * denotes 94 m/z (CO_2 loss). The mass spectrum is located above each plot. Trendlines drawn on each plot highlight the non-spherical growth of the 2-ABAH$^+$(H$_2$O)$_n$ water clusters. That is, 2-ABAH$^+$(H$_2$O)$_n$ does not form a solvent bridge connecting both ends of the benzene, since the functional groups of 2-ABA are adjacent, resulting in the linear ATD trendline observed in **(a)**. 2-ABA and 3-ABA do not display proton transfer behavior via ATD inflections in the n = 5-9 region but are included here for completeness.

require a significant shift in the hydration network, removing waters that bridge the two polar groups (–COOH and –NH_3^+). The ion plays an active role in specifically structuring the water network at n = ~18-22.

For comparison, cryo-IM-MS plots were obtained for 2- and 3-ABAH$^+$(H$_2$O)$_n$ in **Figure 3.2**. 2-ABAH$^+$ has a striking feature in which the ATDs of n = 5-32 fall on a near linear trend line. Typically hydration events cause spherical growth as the droplet approach the bulk limit, which results in nonlinear ATDs; such trends are clearly presented

in the 4-ABAH$^+$(H$_2$O)$^+$ dataset. However, for 2-ABAH$^+$(H$_2$O)$_n$, there is essentially no need to form a bridged structure, as the water droplet can more readily connect the two protonation sites without bridging over the benzene ring.[156] There is primarily 2-D growth with little hydration surrounding the benzene ring until n > 32 for 2-ABAH$^+$(H$_2$O)$_n$. Conformational searches were performed to test this hypothesis. At n = 10 and 20, very little hydration over the plane of the ion is exhibited in **Figure 3.3**. The interactions involved in protein-target interactions are likely defined by limited hydration, and it is emphasized that the charged and hydrophobic regions define the size and shape of the water networks, as seen here. For completion, it is briefly noted that the spectrum of 3-ABAH$^+$(H$_2$O)$_n$ does not appear to exhibit a proton transfer in the n = 1-6 region, in agreement with previous IR results that suggest no proton transfer occurs.[156]

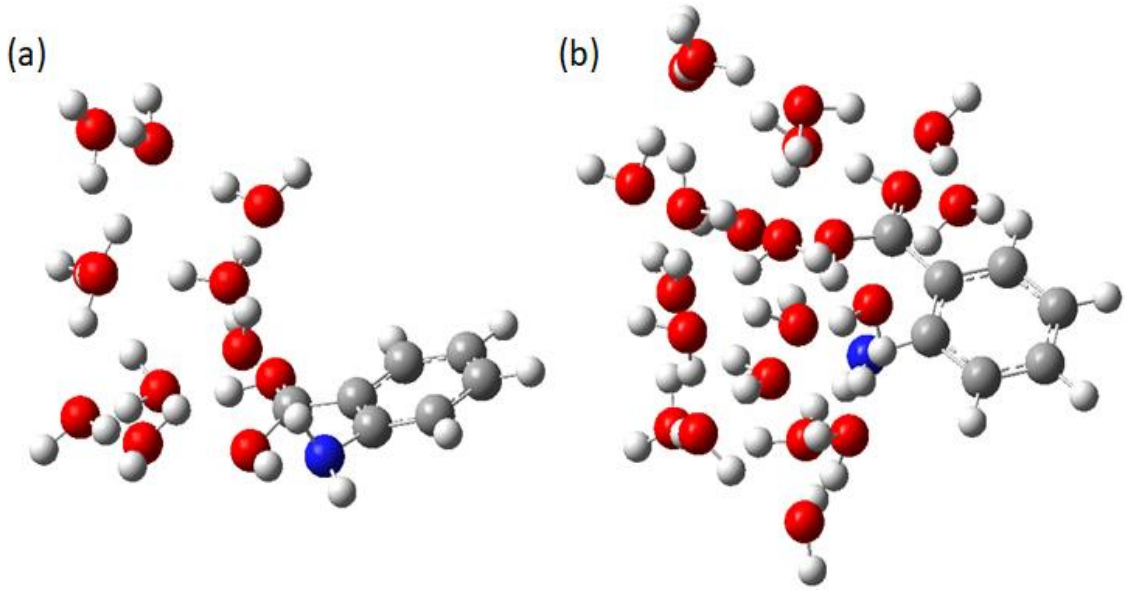

Figure 3.3. MCMM of 2-ABAH$^+$(H$_2$O)$_n$ where (a) n = 10 and (b) n = 20. Note that the proton is located classically on the carboxylic acid in the simulation, but the proton H-bonds with the amine group. Additionally, the hydration does not bridge the rest of the molecule as observed for 3-ABAH$^+$(H$_2$O)$_{10}$ and 4-ABAH$^+$(H$_2$O)$_{10}$, instead preferring to form a droplet surrounding the hydrophilic region.

3.3.2. Effects of Solution and Source Conditions

Patrick *et al.* reported that cooler ionization conditions promote kinetic trapping of the N-protomer,

whereas hotter ionization conditions promote proton transfer.[98] **Figure 3.4** contains ATD vs m/z plots for 4-ABAH$^+$(H$_2$O)$_n$ obtained at different heated capillary temperatures and sprayed from a 1:1 ACN:H$_2$O mixture. However, increasing the capillary temperature from 330 to 371 K did not promote a shorter ATD that would correspond to the O-protomer, suggesting that the two protomers are not resolved here in helium drift gas,[98] or that only a single protomer contributes to each ATD at these

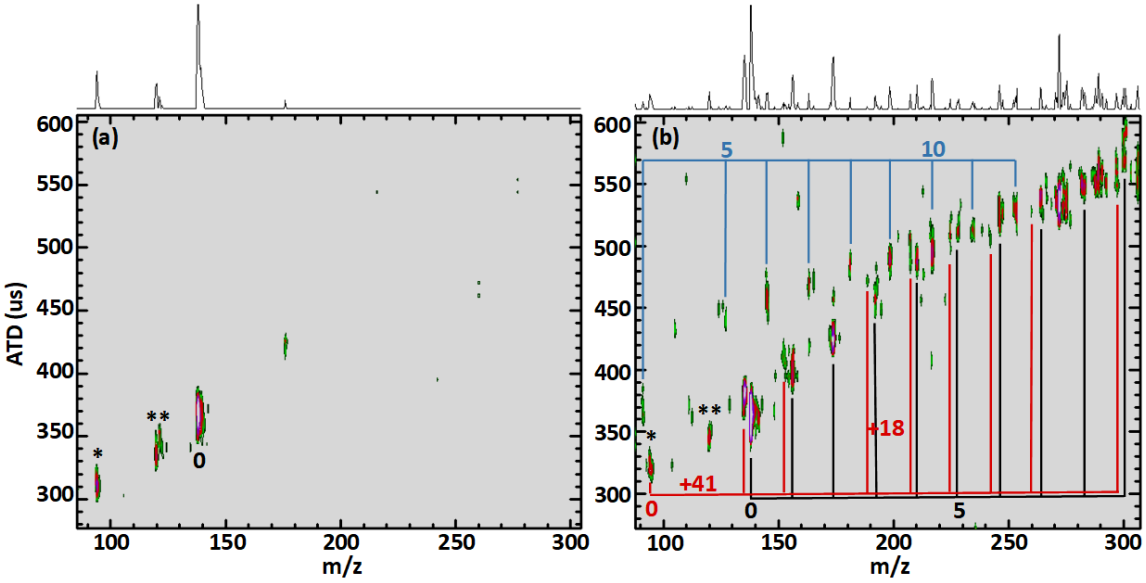

Figure 3.4. ATD vs *m*/*z* plots of 4-ABAH$^+$(H$_2$O)$_n$ at a heated capillary temperature of (a) 371 and (b) 330 K sprayed from 1:1 ACN:H$_2$O solutions with 0.1% formic acid with helium drift gas. H$^+$(H$_2$O)$_n$, 4-ABAH$^+$(H$_2$O)$_n$, and NH$_3^+$C$_6$H$_5$(ACN)$_1$(H$_2$O)$_n$ are labeled in blue, black, and red, respectively. Asterisk denotes 94 *m*/*z* (CO_2 loss), and double asterisk denotes 120 *m*/*z* (H$_2$O loss) fragments. The (4-ABA)$_2$H$^+$(H$_2$O)$_n$ proton-bound dimer and its n = 1 species are observed at 275 and 293 *m*/*z*, respectively. The dimer experiences the same hydrated, ACN-bound adduct as the monomer at 272 and 290 *m*/*z*. The mass spectrum is located above each plot.

temperatures. Inhibiting proton transfer would help differentiate between these two scenarios.

A 1:1 mixture of ACN: H_2O was used as a control to favor the N-protomer upon dehydration as aprotic solvents inhibit proton transfer of 4-ABAH$^+$$(H_2O)_n$.[96, 98-99] **Figure 3.5** shows that nearly identical trends are present for 1:1 ACN:H_2O as in pure H_2O. Notably, the ATD widths, which gauge structural heterogeneity of the ion populations, are very similar, and the two protomers remained unresolved. Interestingly, it appears that the O-protomer is favored for dehydrated 4-ABAH$^+$$(H_2O)_n$ in helium drift gas, regardless of

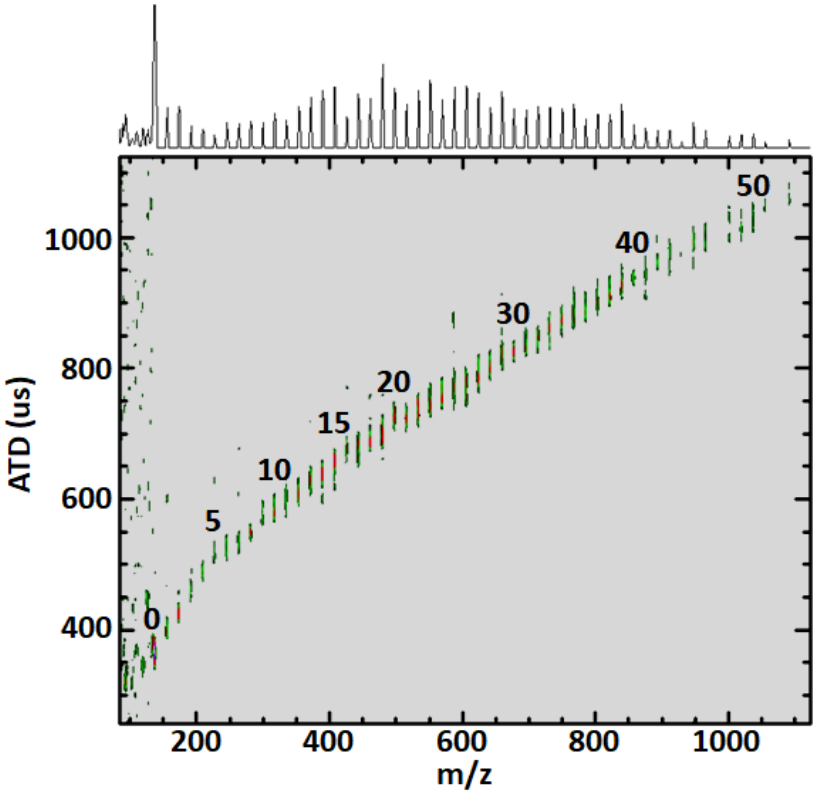

Figure 3.5. ATD vs m/z plot of 4-ABAH$^+$$(H_2O)_n$ with a heated capillary temperature of 330 K sprayed from 1:1 ACN:H_2O solutions with 0.1% formic acid. 4-ABAH$^+$$(H_2O)_n$ peaks display the same behavior (inflections at n = 5-9 and n = 20) as clusters obtained in 0.1% formic acid. See **Figure 3.4** for comparison. The mass spectrum is located above the plot.

solution and ionization conditions. Because it is unclear whether the N- or the O-protomers is isolated in helium, a more polarizable drift gas (N_2) was used for IM separation of the protomers (*vide infra*).

Tian and Kass were the first investigators to note that aprotic solvents increase the relative abundance of the N-protomer by inhibiting the fast proton hopping otherwise available to protic solvents.[96] However, **Figure 3.4b** shows the adduction of ACN to the 94 m/z fragment ion, *and the hydration of this complex* ($NH_3^+C_6H_5(ACN)_1(H_2O)_n$), up to n ~27. ACN adduction to 4-ABAH$^+$ or the 120 m/z fragment is not detected. Nanodroplets maintaining the more volatile solvent (ACN) is unexpected, since rapid and complete evaporation of the more volatile solvent from nanodroplets is typical; the ACN adduct necessarily describes a specific and strong interaction. Without ACN, fragmentation only occurs via an alternative pathway, as evidenced by the lack of hydration of ion fragments from water solutions. ACN molecules provide stabilizing interactions with the $–NH_3^+$ group of 4-ABAH$^+(H_2O)_n$ ions that inhibit proton transfer from the ammonium ion. The stabilization of the N-protomer by ACN is in good agreement with previous experiments, which observe much higher relative abundances of the N-protomer and the 94 m/z fragment ion formed from solutions containing ACN.[96-97, 148, 156]

3.3.3. Effect of N_2 Drift Gas

Polarizable drift gases were previously employed with cryo-IM-MS to increase ion-neutral interactions, that is, Lennard-Jones interaction potentials, and decrease diffusional broadening, which collectively increases ion mobility resolution.[59, 157-163] N_2 drift gas was employed here to enable separation of hydrated protomers.[97, 156, 164] It appears that the same polarizable forces that increase ion-neutral interaction potentials between the drift gas and the ion also serves to stabilize the N-protomer relative to helium drift gas. **Figure 3.6a** contains the ATD vs m/z plot of hydrated 4-ABAH$^+$$(H_2O)_n$ ions with N_2 drift gas. The ATDs of the ions with n = 0, 4, 5, and 6 are plotted in **Figure 3.6b**. At n = 0, there are two prominent peaks, corresponding to the N-protonated (gray) and O-protonated

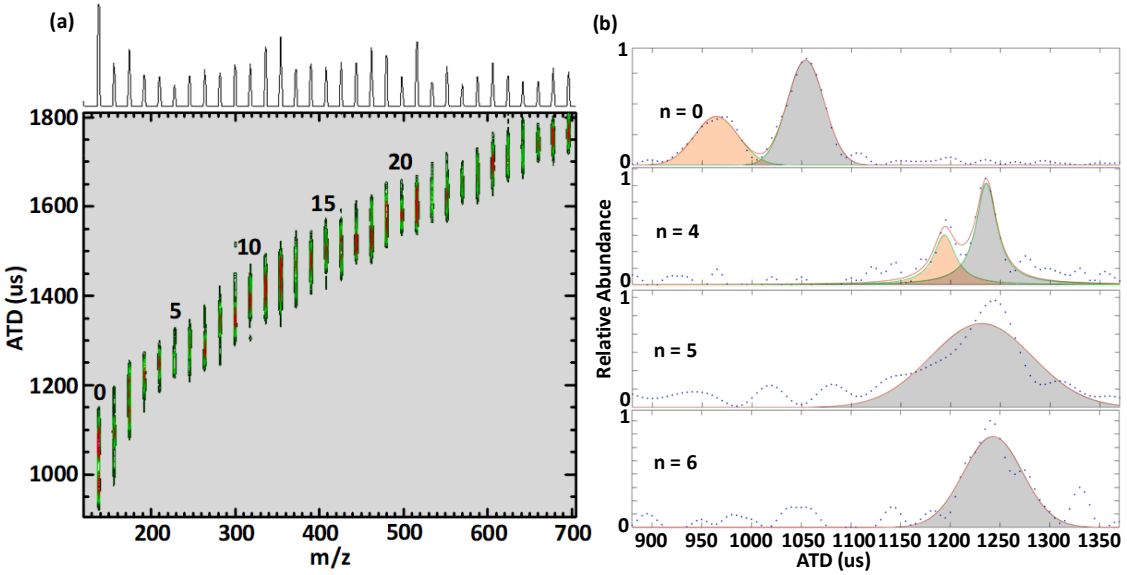

Figure 3.6. (a) ATD vs *m/z* plot of 4-ABAH$^+$$(H_2O)_n$ sprayed from 0.1% formic acid with N_2 drift gas. The mass spectrum is located above the plot. (b) ATDs of 4-ABAH$^+$$(H_2O)_{0,4,5,6}$ are labeled. Gaussian peaks were fit with MATLAB. Blue dots correspond to the unfitted data. Orange peaks indicate the O-protomer, while gray peaks indicate the N-protomer. The drift times are both longer and broader for N_2 drift gas than He drift gas due to the increased size and interaction potential with N_2. The ion gate is also 50% larger (36 μs) for N_2 than for He drift gas (24 μs), which increases the breadth of the peaks.

(orange) species at longer and shorter drift times, respectively.[99, 156] These differences in ATD, relative to helium drift gas, are attributed to the differing interaction potentials with the drift gas by the two protomer states, rather than from significant size deviations in the hydration networks. This trend continues until $n \geq 4$, and the mobility decreases relative to n = 0-4. The relatively high abundance of the N-protomer in protic solvents (water) in this data for $n < 6$ is surprising when compared to previous IM and IR data, which show that, for $n < 6$, the O-protomer is strongly favored.[78, 98] Interestingly, at n = 5, there is a slightly shorter ATD for the N-protomer than expected, at ~1245 μs, probably corresponding to the water-bridge. The stabilization of the water-bridging structure for a smaller water cluster supports the stabilization of the N-protomer by nitrogen drift gas relative to helium drift gas. At n = 5 and 6, two longer ATDs appear that are not present for n = 0-4, at ~1310 and ~1330 μs respectively. These peaks correspond to structures that are larger than the water-bridged N-protomer structure and fall along the n = 0-4 trend line; this suggests that these ATDs correspond to $–NH_3^+$ hydrated (*i.e. unbridged*) structures.

3.3.4. Cryogenic Collisional Cross Section Calibration

Cryo-IM-MS is used as a structural analysis tool by calibrating theoretical CCS values with an experimental arrival time and other constant, measured parameters to determine an experimental CCS.[150] These CCS values, reported in **Table 3.1**Table 3.1. **Trajectory method CCS values and standard deviations of 4-ABAH$^+$(H_2O)$_{0-6}$ in helium at 83 K.**, can be used to identify different protomers, isomers, or peptide and

protein conformational families. It has proven to be challenging to obtain CCS for hydrated ions using cryo-IM-MS, because dehydration occurs at low collision energies (see **Figure 1.5**).[60] This complicates the acquisition of typical 1/V plots used for CCS calibration of pressure and the ion drift time outside the IM. Even if transmission was possible, and the plots were acquired, the sensitivity to the field strength may induce isomerization of water structures (see **Figure 1.5**), affecting the calibration. For the approach used here, CCSs for multiple, hydrated structures were calculated and used to calibrate the drift times to attain CCS for cryo-IM-MS analyses.

Table 3.1. Trajectory method CCS values and standard deviations of 4-ABAH$^+$(H$_2$O)$_{0\text{-}6}$ in helium at 83 K.

n	N-protonated CCS (Å^2)	O-protonated CCS (Å^2)
0	98.30 ± 0.63	92.05 ± 0.74
1	104.9 ± 0.8	100.4 ± 1.1
2	113.0 ± 0.7	107.8 ± 1.0
3	122.5 ± 0.9	117.9 ± 1.1
4	129.0 ± 1.3	126.5 ± 1.6
5	130.0 ± 1.2	135.2 ± 1.3
6	134.0 ± 1.2	141.7 ± 1.4

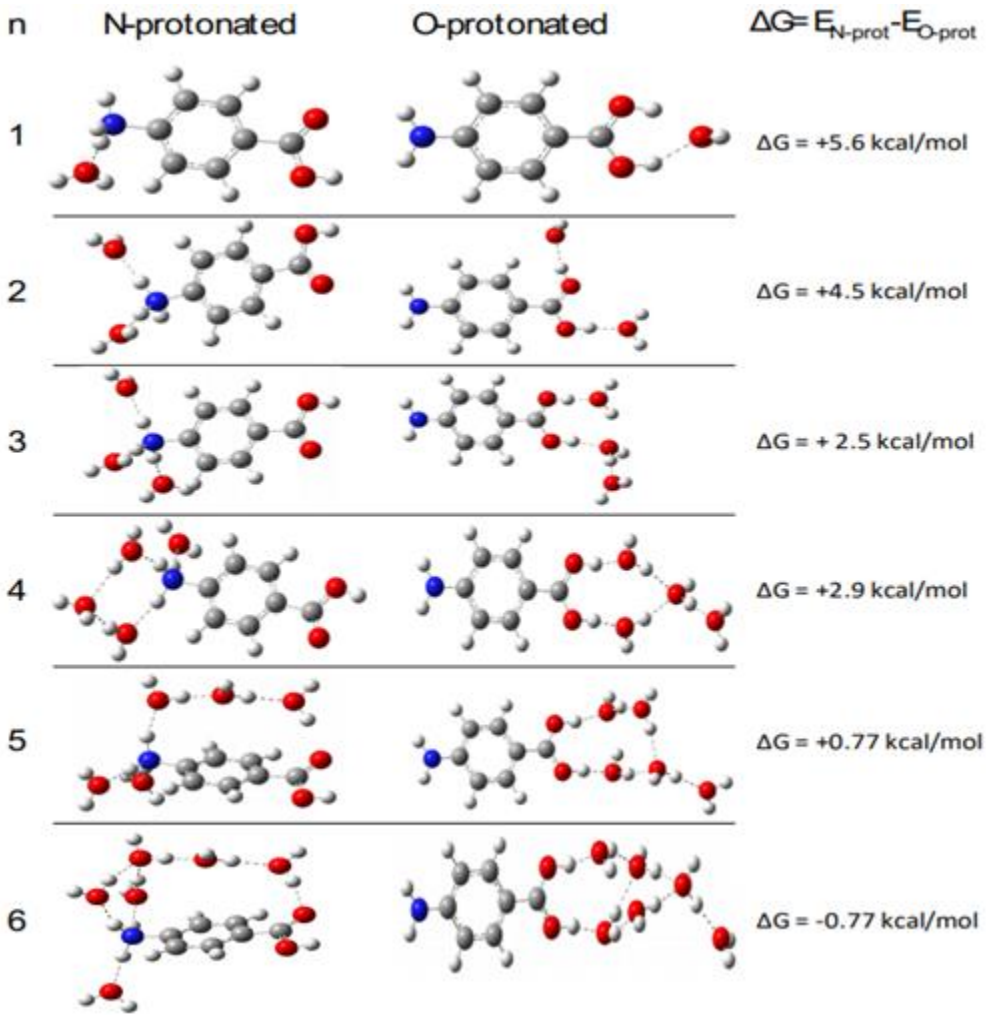

Figure 3.7. Calculated lowest energy structures and relative 83 K Gibbs free energies for 4-ABAH$^+$(H2O)$_{1\text{-}6}$. Relative energies were calculated at the B3LYP/6-311++G** level of theory and ωB97X-D functional in Gaussian 16. The n indicates the numbers of water molecules adducted to 4-ABAH$^+$.

Lowest energy structures were generated for N- and O-protonated 4-ABAH$^+$(H_2O)$_n$ for n = 0-6 (**Figure 3.7**), and MOBCAL trajectory CCS calculations were performed (**Table 3.1**). The theoretical O-protonated CCS structures were plotted against the centroid of the experimental ATDs to generate **Figure 3.8** to obtain a trend line for hydrated ions of n = 0-5. Using this trend line, a CCS of 135.2 ± 1.0 Å^2 was obtained for

n = 6, in agreement with the calculated value of 134.0 ± 1.2 Å^2; the linear relationship is only maintained when the theoretical N-protonated CCS is plotted for n = 6, in agreement with Chang *et al.*[78] Notably, the N-protomer theoretically forms a solvent bridge at n = 5, but no corresponding ATD shift is observed in the mobility until n = 6 (**Figure 3.1b**). Using these structures, similar ATDs at n = 5 and 6 in helium drift gas are interpreted as evidence that the solvent bridge is not retained for smaller water clusters (n < 6). Collapse

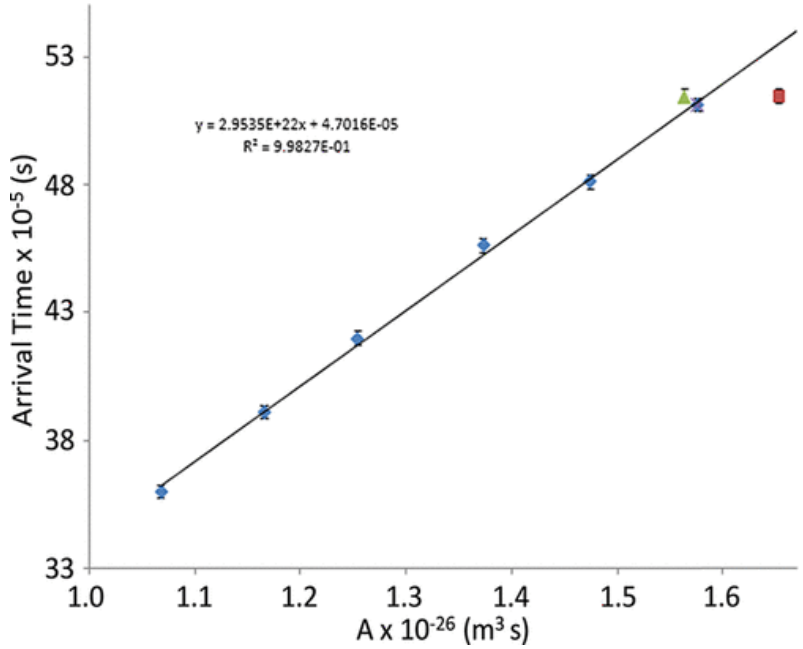

Figure 3.8. Calibration plot of 4-ABAH$^+$(H$_2$O)$_{0–6}$ based on CCS of calculated lowest energy structures in **Figure 3.7**. O-protonated CCSs were used for n = 0-5 (blue diamonds). The N- and O-protonated values for *n* = 6 are denoted by a green triangle and red square, respectively. Error bars represent the standard deviation of the *y* value. The slope of the line corresponds to the gas density in units of parts per m^{-3}, which corresponds to ~0.25 torr at 83 K.

of the solvent bridge and the intracluster proton transfer reaction are supported by the relative energies of the theoretical structures, for which the O-protomer is favored for n = 0-5, but at n = 6, the N-protomer is predicted to be favored by 0.77 kcal/mol. Additionally, dehydrated (n = 0) 4-ABAH$^+$ has a >200 kJ/mol barrier for interconversion between the

protomers;[156] these observations are consistent with a water-mediated proton transfer at n = 6. The linear relationship shown in **Figure 3.8** supports both the theoretical structural assignments in **Figure 3.7** and the proton transfer occurring at n = 6. The head-to-tail alignment of the hydrogen bonding network for n = 6 strongly suggests that proton transfer involves the water bridge; that is, a Grotthuss mechanism seems most plausible. Alternative mechanisms that involve proton transfer to individual water molecules followed by rearrangement reactions would be observable by IM, as the rearrangement would increase the size of the hydrated ion. The relatively narrow ATDs for n = 5-6 hydrated ions suggest a single protomer and structural population for each in the helium drift gas data. The CCS calibration further suggests that only the N-protomer is observed at n = 6. Additional theoretical and IR spectroscopy studies may provide further insights on the precise mechanism of intracluster proton transfer reactions. Nonetheless, CCS calculations for the hydrated ions provide strong evidence for the proposed structures involved in the proton transfer at n = 6.

The n = 2 structure of 4-ABAH$^+$$(H_2O)_n$ also exhibited two nearly isoenergetic theoretical structures for the O-protonated form. Notably, these two structures differ in the cis/trans configuration of the –COHOH group. The theoretical CCS of the trans configuration is 107.6 ± 1.0 Å^2 best fits the expected trendline value of ~107.5 ± 0.8 Å^2. Notably, it is better to separately H-bond with each H_2O rather than for the –COHOH to share two H-bonds with one water molecule (see **Figure 3.9**). However, this dynamic

changes rapidly upon hydration, shifting towards the cis conformation to enable extra H-bonding opportunities within the growing water cluster. When there is a single water

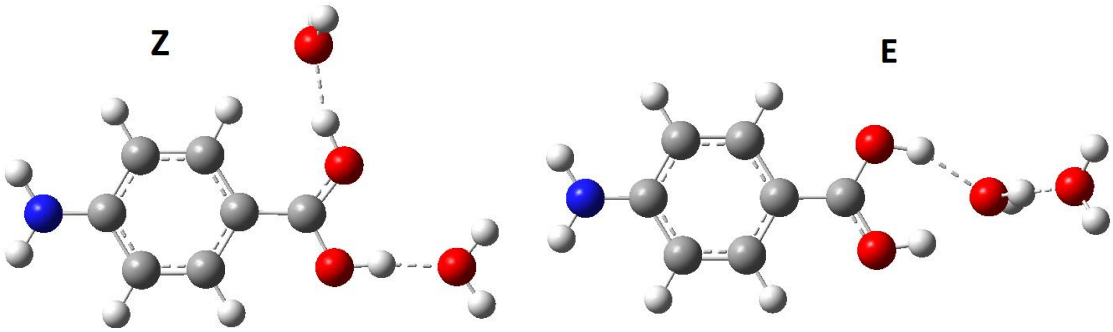

Figure 3.9. The trans (Z) and cis (E) forms of 4-ABAH$^+$$(H_2O)_2$ are shown. The trans structure is favored by only 0.27 kcal/mol.

molecule left, it is more energetically favorable to share the H-bonding opportunities via the cis form. The trans conformation may play an important role in initiating proton transfer when the molecule is being hydrated by shortening the distance between proton transfer sites.

3.4. Conclusions

Cryo-IM-MS was used to investigate the hydration of 4-ABAH$^+$ $(H_2O)_n$ clusters. A proton transfer from the solution-phase N-protomer to the gas-phase O-protomer at n = 6 is supported by a structural shift observe by cryo-IM-MS at n = 6, in which the ATD remains constant. A water-bridged n = 6 structure would have a smaller CCS than a water structure that only hydrated the –COOH group. A water network rearrangement at n = 20 was also briefly investigated and is the subject of the next chapter. Briefly, a large increase in ATD at n = 20 relative to n = 19 and 21 suggests that the water network undergoes a rearrangement to a larger, magic number structure, similar to other amine-containing

molecules. Notably, these structural trends can be carefully interpreted by cryo-IM-MS, and have been in all the previous work, but they remain ambiguous without CCS.

Cryo-IM-MS CCS values were calibrated using the ATDs of 4-$ABAH^+(H_2O)_n$ which removes ambiguity in the structural assignments of 4-$ABAH^+(H_2O)_n$ clusters. The calibrated CCS for n = 6 agrees well with the calculated N-protomer CCS, while the n = 5 CCS agrees well with the calculated O-protomer, supporting the N-to-O-protomer transition at n = 6. The observed water-bridged structure at n = 6 becomes unstable and forms the O-protomer for n < 6. Furthermore, the head-to-tail nature of the waters forming the bridge suggests a proton shuttling/Grotthuss mechanism, since no rearrangement structures were observed. However, theoretical work on the exact molecular/electronic mechanism of the determined structures will be necessary. The proton transfer of 4-$ABAH^+(H_2O)_n$ is interesting in the context of confined environments. During the final desolvation stages of ESI, transporting protons away from their solution-phase locations can fundamentally alter the structural integrity of polar molecules. Proton transfer may negatively impact the formation of native-like structures (via different potential salt-bridges, hydration structures, and intramolecular charge solvation) formed by ESI and alters gas-phase structures.[62, 94, 165] Such structural shifts must be avoided if gas-phase structures observed via IM are to be compared to their solution-phase structures.[166] It should be noted that the CCS calibration method used here is general and can be applied to other studies exploring structural effects of so-called biological water; ideally, these studies will expand to hydrated peptide and protein structures.

The inhibition of proton transfer by acetonitrile and N_2 drift gas was investigated. For solutions containing ACN, the inhibition is attributed to stabilizing interactions of ACN with the $–NH_3^+$ group. Typically, drift gases and drift gas dopants are chosen to alter the selectivity of the separation due to differences in separation based on the reduced mass of the analyte and drift gas, compound classes, and polarizability, as was done here.[59, 157-163] However, proton transfer was also partially inhibited when using N_2 drift gas; even though the helium drift gas results confirm that proton transfer artifacts can result from desolvation during late-stage ESI, these drift gas studies imply that interactions with polarizable gases and counterions may be exploited to inhibit late-stage ESI proton transfer reactions.[139, 144] These results draw attention to the kinetic trapping that can occur as a result of different solution conditions and drift gases.[56]

4. HYDRATION OF AMMONIUM IONS: WATER STRUCTURES FLUCTUATE BASED ON THE POLAR ENVIRONMENT

4.1. Background

The interplay between polar molecules and water molecules is described in section **1.3.4**. In **Chapter 3**, the effects of water molecules on the nature and location of the charged polar structure were described. Here, the effects of polar molecules on the structure of water are considered. The structure of a magic number cluster is dependent on the solvated ion. For instance, in $H_3O^+(H_2O)_{20}$ the H_3O^+ ion is located on the surface of the clathrate cage, whereas it is more energetically favorable for Cs^+, K^+, Rb^+, and NH_4^+ to reside in the interior of the $(H_2O)_{20}$ cage.[85, 167] However, ammonium ions often exist not as an independent ion but as the functional group of lysine or ornithine. Infrared photodissociation (IRPD) spectroscopy evidence from Chang *et al.* supports the location of protonated amines on the surface of magic number clusters when sterically hindered from the center of the cluster (*e.g.* methylammonium, n-heptylammonium, tert-butylammonium, *etc.*).[86] Lysine- and ornithine-containing peptides are also known to form magic number clusters,[38, 60, 93] so investigations on the formation of ammonium-containing magic number clusters will provide insight into the poorly understood magic number clusters observed for peptides. In particular, these peptides boast many hydrophilic and charged regions, whereas magic number cluster structural studies have classically investigated singly charged ions or point charges. There is also little emphasis on droplets of similar size even though the solvent shells that ions exist in are dynamic.

Here, cryo-IM-MS is used to monitor the structural water for polar ions containing 19-21 waters. The structural waters for amine-containing analytes with one to two hydrophilic regions are compared: 4-aminobenzoic acid, anilinium, and heptylammonium.

The polar ions selected, anilinium, heptylammonium, and 4-aminobenzoic acid, represent a range of interactions of interest in larger biomolecules, including hydrophobic, hydrophilic, charged, and van der Waals interactions. Anilinium contains an ammonium group and a rigid, apolar region, which should primarily hydrate the ammonium group at low water cluster numbers. Heptylammonium has an ammonium group and an apolar, flexible chain. 4-ABAH$^+$ provides an interesting case in which there are two hydrophilic regions, separated by a hydrophobic region. This scenario may better resemble a peptide with more than one hydrophobic region. Each ion selected here also has an ammonium group that forms a magic number cluster at n = 20.

4.2. Methods

4.2.1. Experimental

4-aminobenzoic acid, aniline, and heptylamine (>99%) were purchased from Sigma-Aldrich and used without further purification. Solutions were prepared in 0.1% formic acid by dissolving 4 mM ABA in 18.2 MΩ water. Solutions were nano-sprayed from gold-coated borosilicate capillaries (OD <~5 μm) into a home-built cryo-IM-MS.

4.2.2. Computational

The computational methods are the same as in section **3.2.2**, with two major differences. There are now two categories of starting configurations, which are referred to in the text as "biased" and "unbiased" water networks. In the unbiased configuration, waters were placed randomly around the entire molecule of interest prior to MCMM calculations. In the biased configuration, ions were preferentially placed surrounding the ammonium ion prior to MCMM calculations. These configurations help the MCMM sample regions of conformation space that are otherwise inaccessible to the calculation. Second, these calculations have been performed at a lower level of theory, 6-311** due to their increased size making the water calculations prohibitive at higher levels of theory.

4.3. Results and Discussion

4.3.1. Comparison of Hydrated Ammonium-Containing Molecule Structures

There is a clear increase in the CCS of the water network of 4-ABAH$^+$$(H_2O)_{20}$ according to the ATD in **Figure 4.1**, and a similar n = 20 increase is apparent in the mobility of hydrated heptylamine.[102, 104] In both instances, the ATD decreases again after the anomalous increase in ATD at n = 20. Anilinium also undergoes an increase in ATD in this region, but the water clusters maintain the n = 20 structural family for larger water clusters, rather than shifting back to lower ATDs for n > 20. To determine what structural deviations cause these results, MDS were used to determine likely lowest energy structures, and the structures were used in the CCS calibration method described in **3.2.1**.

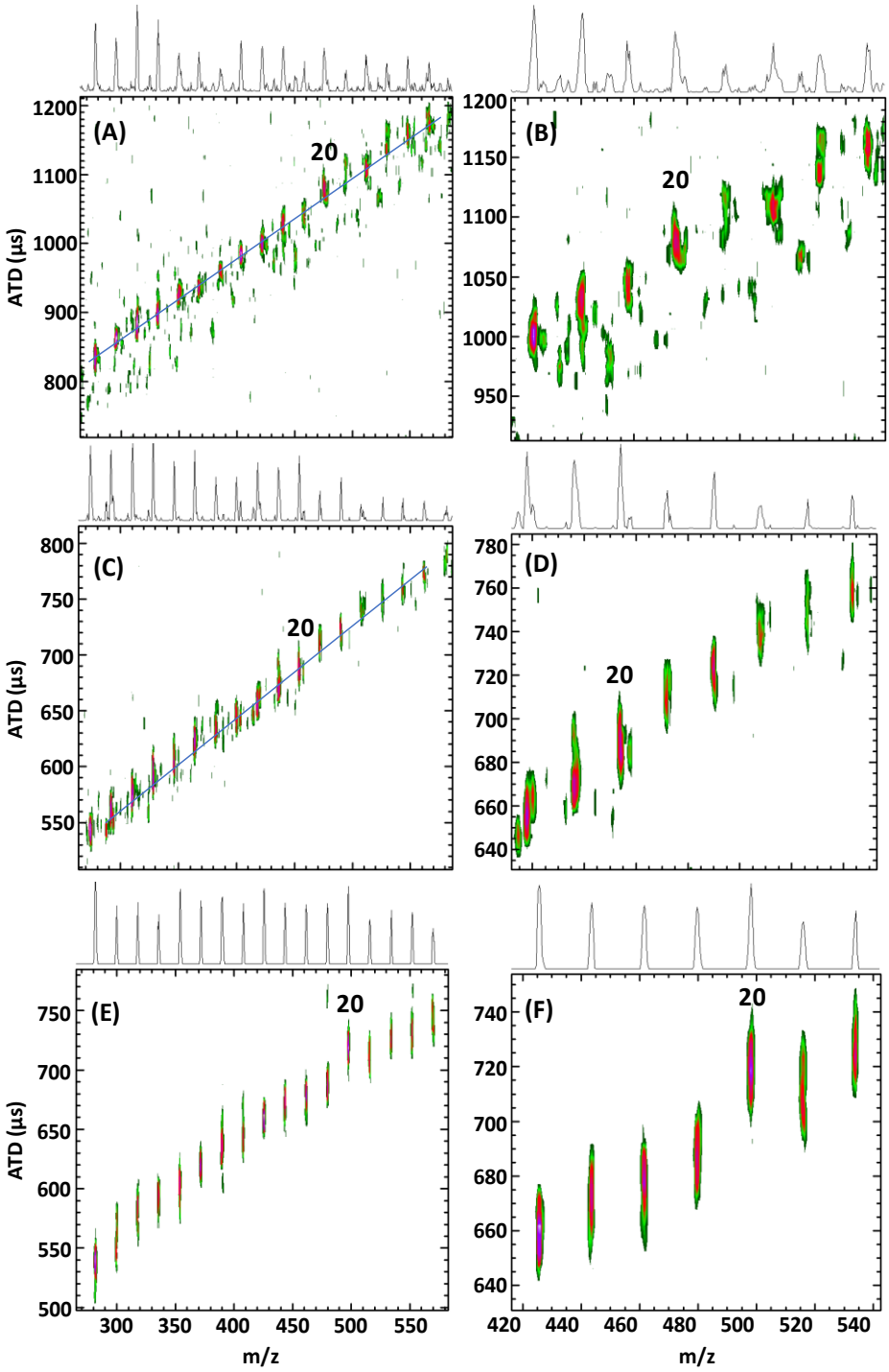

Figure 4.1. ATD vs m/z plots of (A-B) heptylammonium$^{+}(H_2O)_n$, (C-D) anilinium$^{+}(H_2O)_n$, and (E-F) 4-ABAH$^{+}(H_2O)_n$ sprayed from 0.1% formic acid. The mass spectrum is located above each plot. Lines are shown only to guide the eye and do not necessarily represent linearity of the ATDs.

Biased and unbiased water networks, and their relative energies, are shown at n = 20 of 4-ABAH$^+$(H$_2$O)$_{20}$, heptylammonium$^+$(H$_2$O)$_{20}$, anilinium$^+$(H$_2$O)$_{20}$ in **Figure 4.2**. In the case of anilinium$^+$(H$_2$O)$_{20}$, the water surrounds the hydrophilic ammonium group, with no hydration of the inflexible, hydrophobic benzene ring regardless of the bias. For heptylammonium$^+$(H$_2$O)$_{20}$, although the waters cluster around the ammonium group, the flexible, hydrophobic side chain can exploit van der Waals interactions with the water clusters, regardless of the bias selected. Some slightly higher energy structures (~1.4 kcal/mol) in which there is little to no hydrophobic hydration were also formed; all the hydrating water molecules surround the ammonium ion, making this structure larger. Despite the decreased relative stability of the latter structure type, IM data shows that a larger structure is present at n = 20, relative to n = 19 and 21. Similarly, an increased ATD at 4-ABAH$^+$(H$_2$O)$_{20}$ suggests a larger structure, whereby the water preferentially hydrates *only the ammonium ion*. For 4-ABAH$^+$(H$_2$O)$_{20}$, hydrating waters bridge the two polar groups in the unbiased simulation but preferentially hydrate the ammonium ion in the biased calculations. Structures hydrating the ammonium ion in 4-ABAH$^+$(H$_2$O)$_{20}$ are preferred by ~5.8 kcal/mol over those that form a water bridge to the carboxylic acid.

4.3.2. Collisional Cross Section of the 4-ABAH$^+$ Magic Number Cluster

CCSs were determined for the lowest energy structures of 4-ABAH$^+$(H$_2$O)$_n$. At n = 20, a CCS of 204.8 ± 2.1 Å^2 agrees well with the theoretical calculation of 205.0 ± 1.4 Å^2 for the biased water network. This structure is 7.3% larger than the water structure that bridges the two hydrophilic regions, which occurs for n = 19 and n = 21. The ammonium

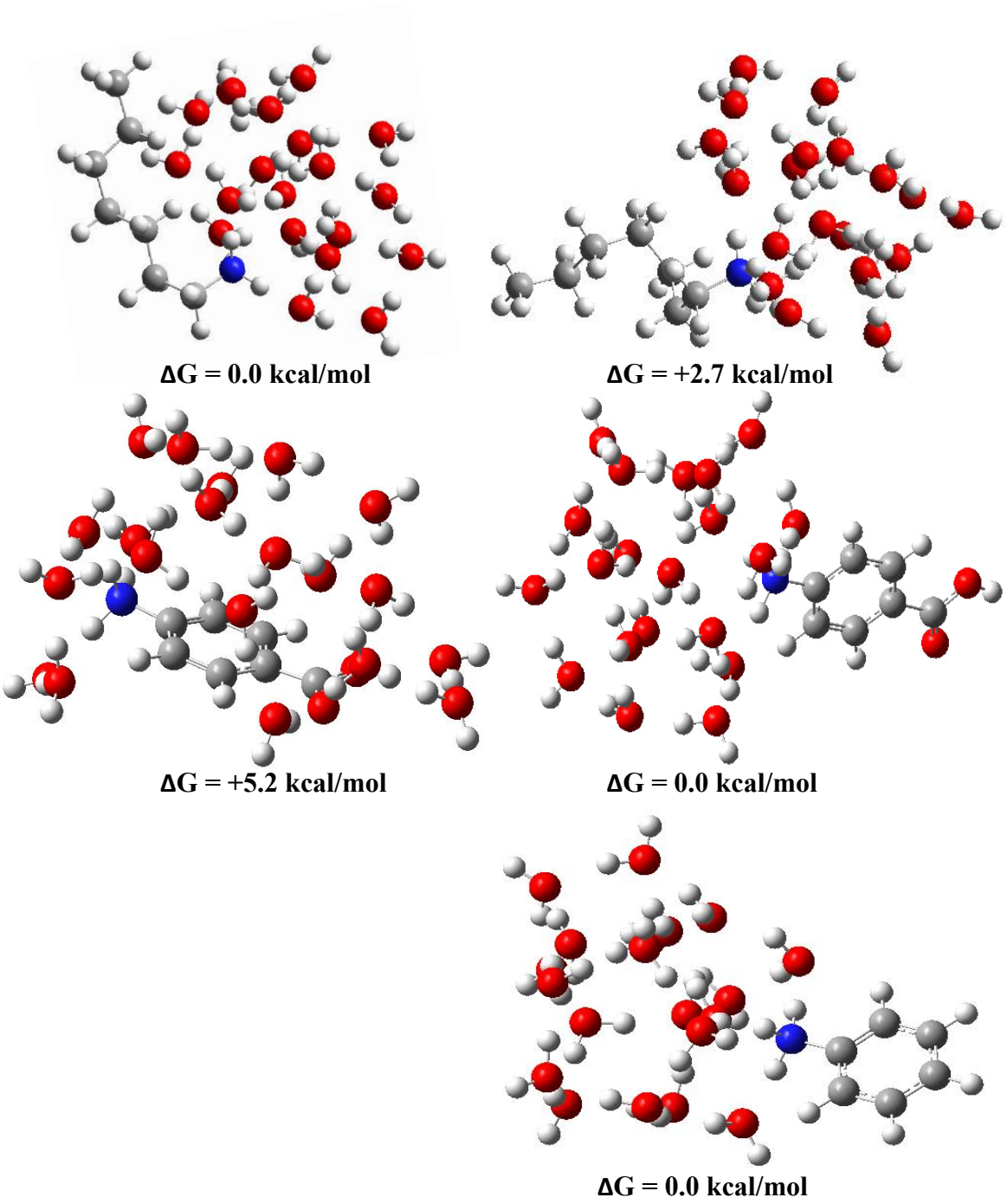

Figure 4.2. Representative lowest energy structures of (top) Heptylammonium$^{+}(H_2O)_{20}$, (middle) 4-ABAH^{+}(H2O)$_{20}$, and (bottom) anilinium$(H_2O)_{20}$. Hydration favoring primarily the $–NH_3^{+}$ (right) are compared to more compact structures that do not favor hydration of only the $–NH_3^{+}$ (left). Relative energy values are labelled. The hydrophobic hydration was calculated to be favored by ~2.72 kcal/mol.

ion sits on the edge of the water cluster, since the ammonium ion cannot easily access the center of the water cluster.[167] Hydration studies have previously noted the hydrophobic nature of the benzene ring and hydrophilic nature of the two functional groups,[168] but this IM data shows the hydrating waters are shifted away from the carboxylic acid group at n = 20. When magic number clusters are observed, the n + 1 clathrate structure is usually preferentially dehydrated due to instability while the n = 20 is retained longer due to enhanced stability specific to the geometry of the pentagonal dodecahedral clathrate structure, as can be seen in anilinium and hepytlammonium. However, the simplicity of this model is not maintained in the case of 4-ABAH$^+$$(H_2O)_{20}$, in which the polar ion alters the dominant water-bridging structure specifically at n = 20.

4.3.3. Hydration Dynamics of Dehydrating Droplets

The n = 20 hydration structural transitions involved in both 4-ABAH$^+$$(H_2O)_n$ and heptylamine$^+$$(H_2O)_n$ provide an interesting description of the final stages of desolvation and hydration preferences. In section **3.3.4**, it was shown that a water bridge persists between the ammonium and carboxylic acid groups of 4-ABAH$^+$$(H_2O)_n$ as low as n = 6. Here it is shown that the water bridge is ruptured at larger values of n in favor of a more stable conformation, before returning to the water bridge structure. Specific structural responses to the number of water molecules within an ion-water cluster raises an important point: hydrated structures are not dehydrated in a static manner; dehydrating water molecules can rapidly equilibrate to form new structures after an evaporative event. Such dynamics may be operative only for each evaporative event, whereas each cluster size

itself may not be dynamic. In the case of 4-ABAH$^+$(H$_2$O)$_{20}$, this would explain why there is not a broad range of IM values corresponding to both the bridged and unbridged structures; dehydrating water molecules can rapidly equilibrate to form new structures when there is sufficient energy available for an evaporative event. Furthermore, peptides and proteins with magic number clusters may not form structural families that resemble those of similarly sized water clusters. Consider, for example, that the magic number cluster n = 11 for the peptide gramicidin S is not necessarily similar to the non-magic number clusters n = 10 or 12. Indeed, given the highly variable ATDs observed for GS^{2+}(H$_2$O)$_n$ where n = ~1-20,[60] it is likely that the structures change rapidly in this hydration region. The water structure may entirely re-arrange to accommodate other hydrophilic, charged, and even hydrophobic residues for non-magic number structures, contrasting with the sequential dodecahedral clathrate structures formed by smaller H$_3$O$^+$(H$_2$O)$_n$ water clusters for instance. In the case of larger molecules with regional hydrophilicity, water appears to maintain a dynamic role in the hydration of nanoclusters containing polar molecules.

4.4. Conclusions

The extension of determining CCS via MDS is shown here for water clusters in the size range of ~430-520 Da. It is also briefly noted that structural deviations in the size of the water cluster must be present to correctly assign CCS values and structures. These MDS are already quite computationally expensive and further expansion of cryo-IM-MS CCS determinations into the size regime of peptides and proteins will require the use of

less computationally expensive force fields, such as CHARMM,[169] AMBER,[170-171] or GROMACS.[172]

The water structures of hydrated anilinium, heptylammonium, and 4-aminobenzoic acid are compared here. Although all three ions share similar magic number cluster numbers, water clusters similar in size are dependent on the nature of the polar ion. Of particular interest is that hydrophobic hydration in heptylammonium is preferred over the formation of clusters surrounding the ammonium group as is the case for anilinium. The hydrophobic hydration induces a more compact structure for the flexible chain within the droplet. For peptides and proteins that contain flexible, hydrophobic regions, the hydrophobic hydration of the waters surrounding $–NH_4^+$ ions is more energetically favorable than the hydration of only the charged region.

Water structures can be finely tuned to the number of water molecules in these hydration shells here, as indicated by the ATD shift in 4-aminobenzoic acid. In particular, since these hydrated clusters are dehydrated in a sequential manner, the shift from a bridged water cluster at n = 21 to a magic number cluster at n = 20 back to a bridged water cluster at n = 19 showcases the sensitivity of the water network to the numbers of water molecules and the polar molecule.[60]

5. FUTURE DIRECTIONS, SUMMARY, AND OUTLOOK

5.1. Increasing Mass Resolution and IM Duty Cycle

There are two major figures of merit that block the expansion of in-depth cryo-IM-MS studies past simple small molecule systems: mass resolution and the IM duty cycle. First, the mass resolution for small peptides and proteins is limited to ~500. Second, the duty cycle of the IM drift cell is about 1% causing experimental timeframes of ~hours. Notably, this timeframe is unsustainable, because the cryo-IM-MS instrumentation is susceptible to icing over time, causing complete loss of ion transmission.

One of the major benefits of increased mass resolution is the simplified identification of unknown ions. Lower resolution is generally sufficient for simple solutions containing known amounts of small peptides or proteins used in the cryo-IM-MS experiments. However, since large numbers of water molecules are observed for each charge state, the mass spectra of different charge states begin to overlap. Despite relatively simple solution conditions, analysis of cryo-IM-MS species is quickly complexified due to the overlapping of hydrated charge states. If the charge states are separated in the mobility space, then higher resolution is not generally required. However, as biomolecules increase in size, it is often the case that these charge states overlap, as in the case of substance P (~1348 Da). This trend has also been observed for cytochrome c (~12 kDa) and hydrated ubiquitin dimers (~17.2 kDa) (*vide infra*). A 3-D rendering of the new R. M. Jordan time-of-flight (ToF) is shown in **Figure 5.1**. The increase in mass resolution to

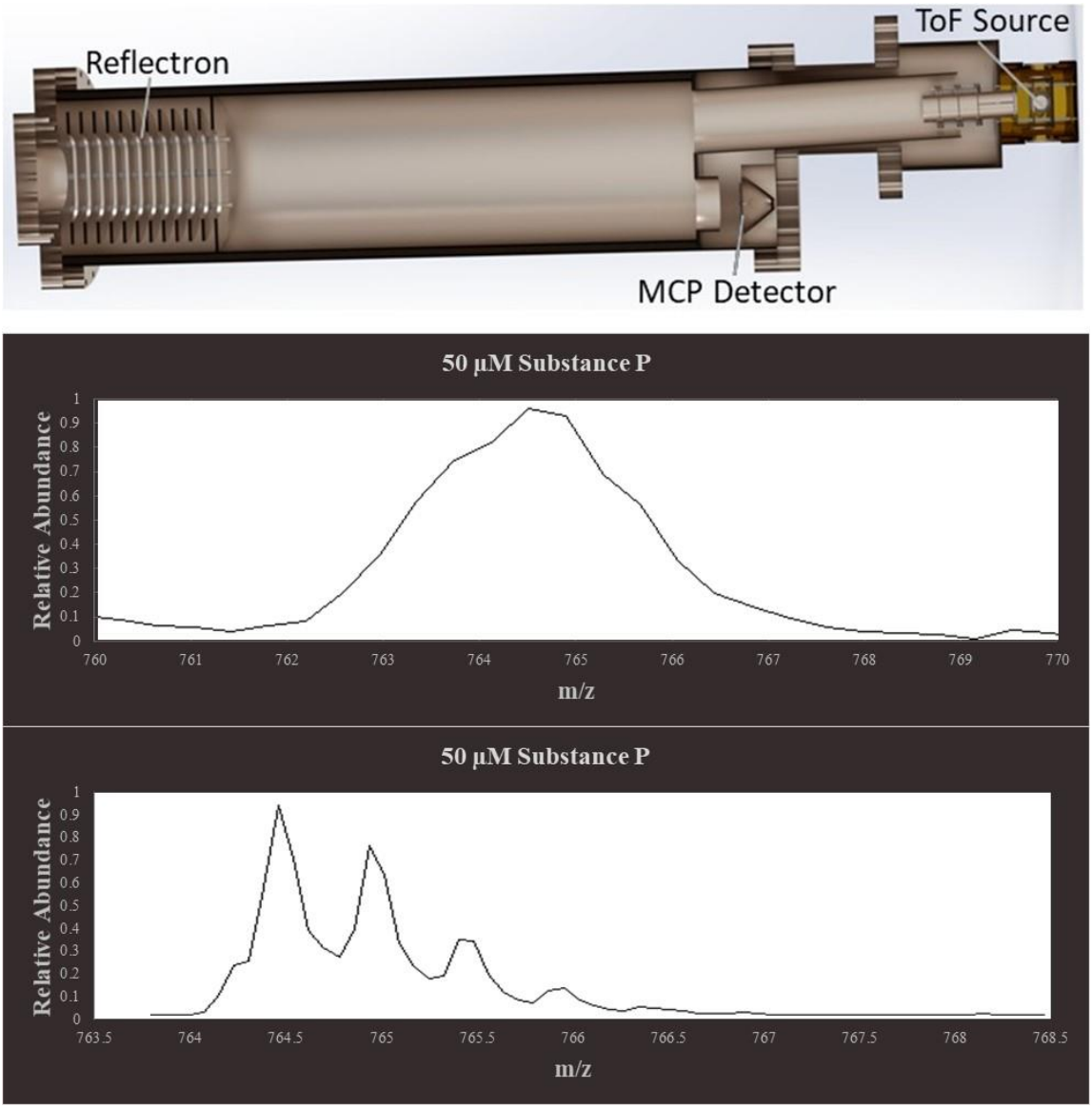

Figure 5.1. (top) A 3-D rendering of the R. M Jordan ToF. Comparison of the isotopic mass spectra of SP^{2+} from (middle) the first generation ToF with ~500 mass resolution and (bottom) the R. M. Jordan ToF with ~3500 mass resolution.

~3500 of the R. M. Jordan ToF is also shown. This increased resolution has already been used to correct previous $SP_M^{3+}(H_2O)_n$ and $SP^{3+}(H_2O)_n$ assignments;[173] a faster ATD peak than the SP_M^{2+} peak was previously interpreted as an $[SP_M + 2H]^{2+}$ ion that had flown through the drift tube as an $[SP_M + 3H]^{3+}(H_2O)_n$ ion where n = 0, 3, or 6. More recent data

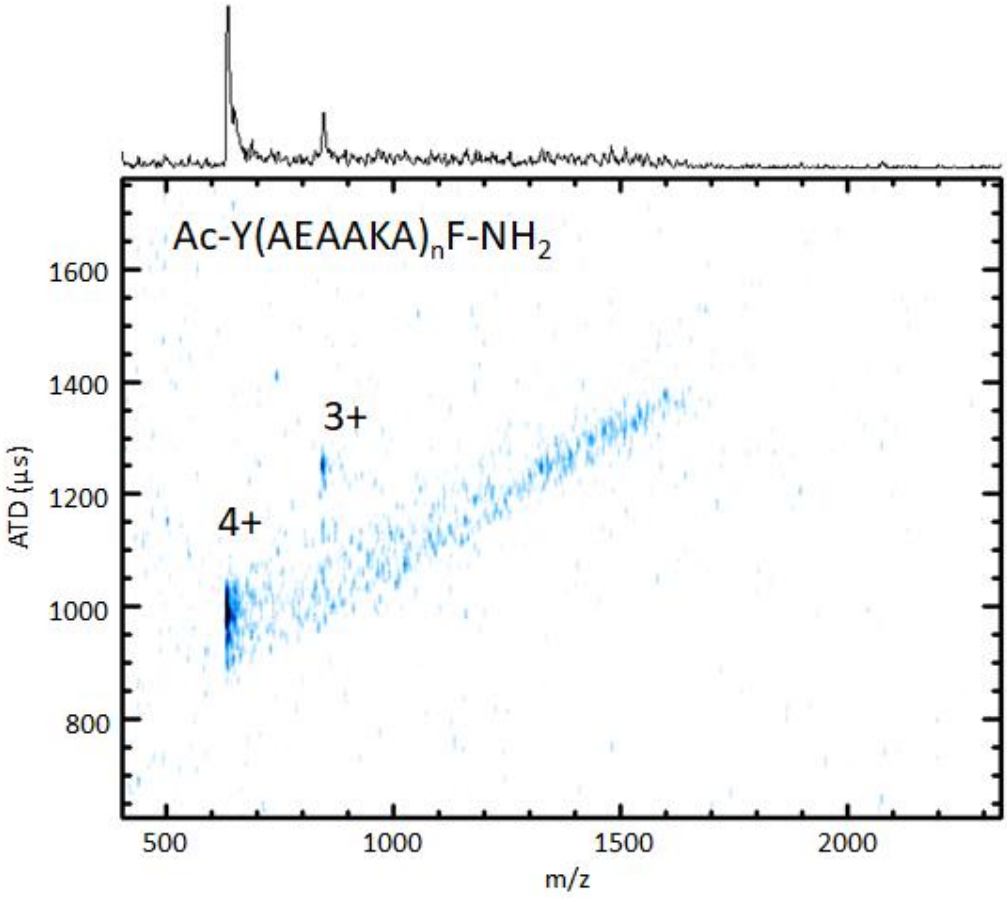

Figure 5.2. Hydration of the peptide 10 µM AEK_4 in 0.1% FA. Hydration of only the more highly charged peptide indicates that the lower charge state is formed after nearly complete dehydration of the $AEK_4^{4+}(H_2O)_n$ ion.

of peptides with multiple charge states, but only one hydrated charge state, suggests late stage proton transfers likely do occur late in the ESI process (n ~ 1-10), but not as previously described by Servage *et al.;* the increasing proton affinity of smaller water clusters likely plays a role in deprotonating highly charged peptides that are nearly completely dehydrated.[173-174] This characteristic hydration pattern is shown briefly for the peptide Ac-Y(AEAAKA)$_n$F-NH_2 (AEK_n), where n = 4, in **Figure 5.2**. In **Figure 5.3**, water clusters leading to the peak labelled as the dimer ($2SP^{4+}$) have 4.5 m/z spacing

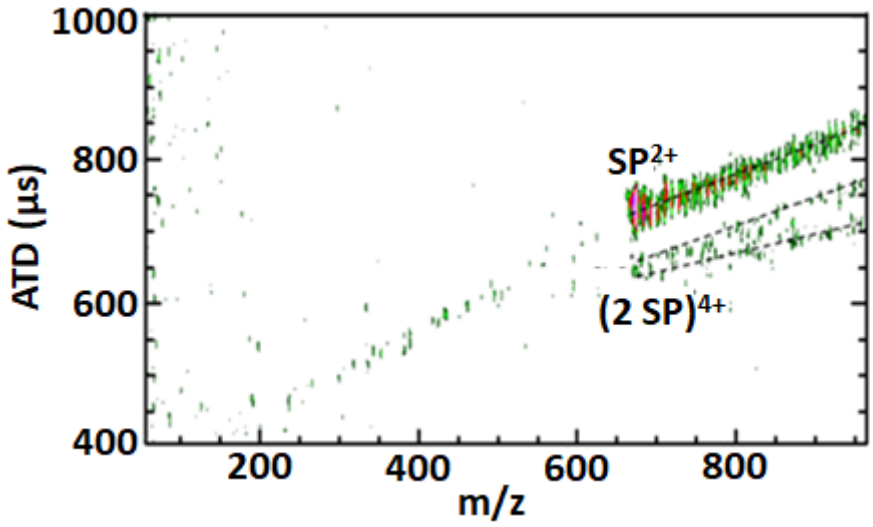

Figure 5.3. ATD vs m/z plot of 50 µM SP in 1 µM trimethylammonium oxide and water reveals hydrated $2SP^{4+}$ ions.

corresponding to 4^{+} water molecules. Interestingly, the isotope pattern of the main peak is that of SP^{2+}, indicating that the dehydrated dimer dissociates to form the monomer. This may resemble the dissociation of noncovalently bound ubiquitin dimers when they are nearly dehydrated.[101]

Previous work by Servage *et al.* suggested that the ubiquitin D^{14+} charge state is well-hydrated, whereas the M^{7+} is formed from near complete dehydration of the dimer.[101] The D^{14+} hydration extended to ~285 water molecules, but there is some overlap where the D^{12+} peak and its hydrates would be expected. With no apparent M^{6+} peak formed from dehydration, it was reasonable to assume that there was not a significant population of D^{12+} ions. **Figure 5.4** contains an ATD vs m/z plot of 100 µM ubiquitin under similar conditions described by Servage *et al.*[101] Here, oligomerization occurs at several reduced charge states. There is significant overlap between the hydrated dimer ions, and there may also be hydrated trimer ions in low relative abundances. Increased MS resolution will

simplify the identification of these species, but more interestingly, it will allow for identification of specific structural trends as a function of numbers of water molecules bound. The advantages of such studies have been expanded upon in this work for small, hydrated ions. Studies of larger biomolecules will isolate kinetically trapped biomolecules and their interactions with local water molecules, ions, *etc*.

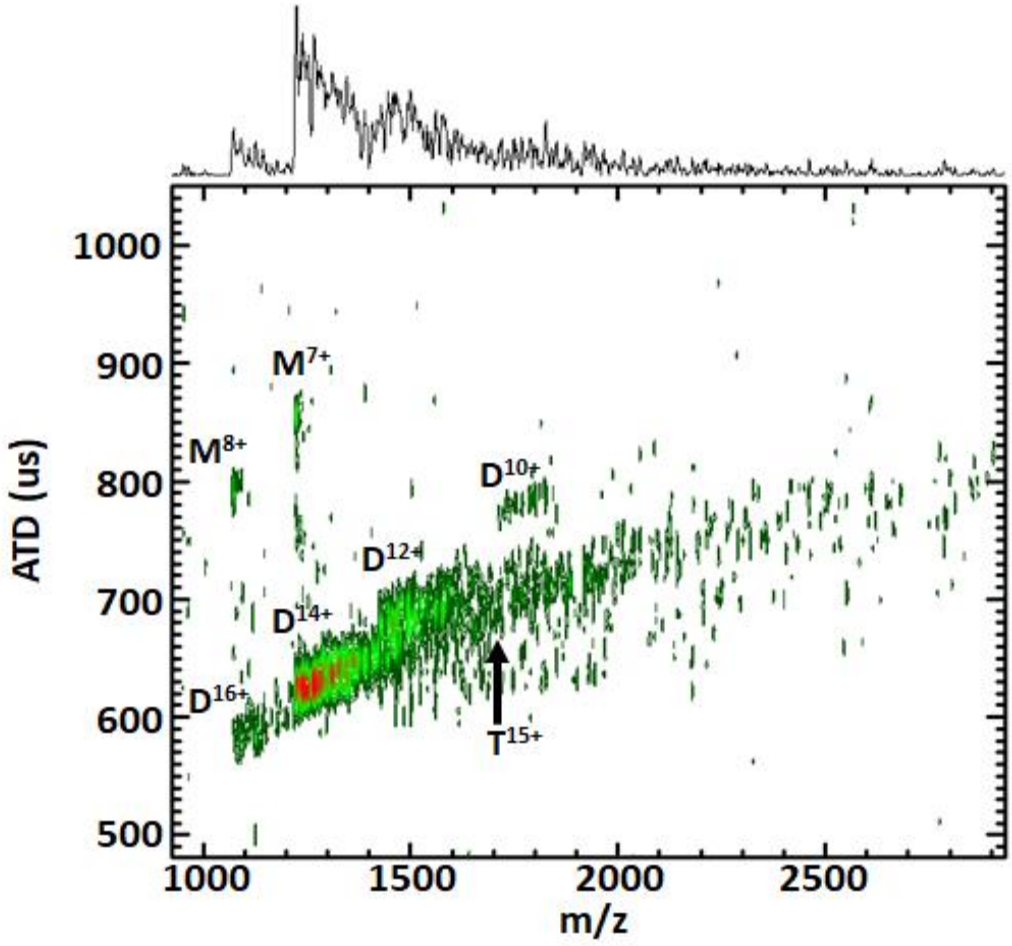

Figure 5.4. ATD vs m/z plot of 100 µM ubiquitin in 0.1% FA, sprayed at a heated capillary temperature of 355 K. This spectrum shows the dehydration of dimers that dissociate to form monomers (M^{7+}/M^{8+}), but also reveals other overlapping hydrated charge states. A potential hydrated 15^{+} trimer (T^{15+}) is labelled.

Another example of the need for increased mass resolution is shown by the ATD vs m/z plot of 30 µM cytochrome c in **Figure 5.5**. The $M^{8+}(H_2O)_n$ ATD peak widths oscillate as a function of numbers of water molecules bound indicating structure dynamics of cytochrome c are dependent on the water network. There is also a notable increase in the ATDs at ~130 H_2O, followed by shorter ATDs until ~150. With the current resolution, it is unclear if this is a well-defined transition over the course of 1-2 water molecules, or if the transition occurs over many cluster sizes. Addressing the solution- to the gas-phase

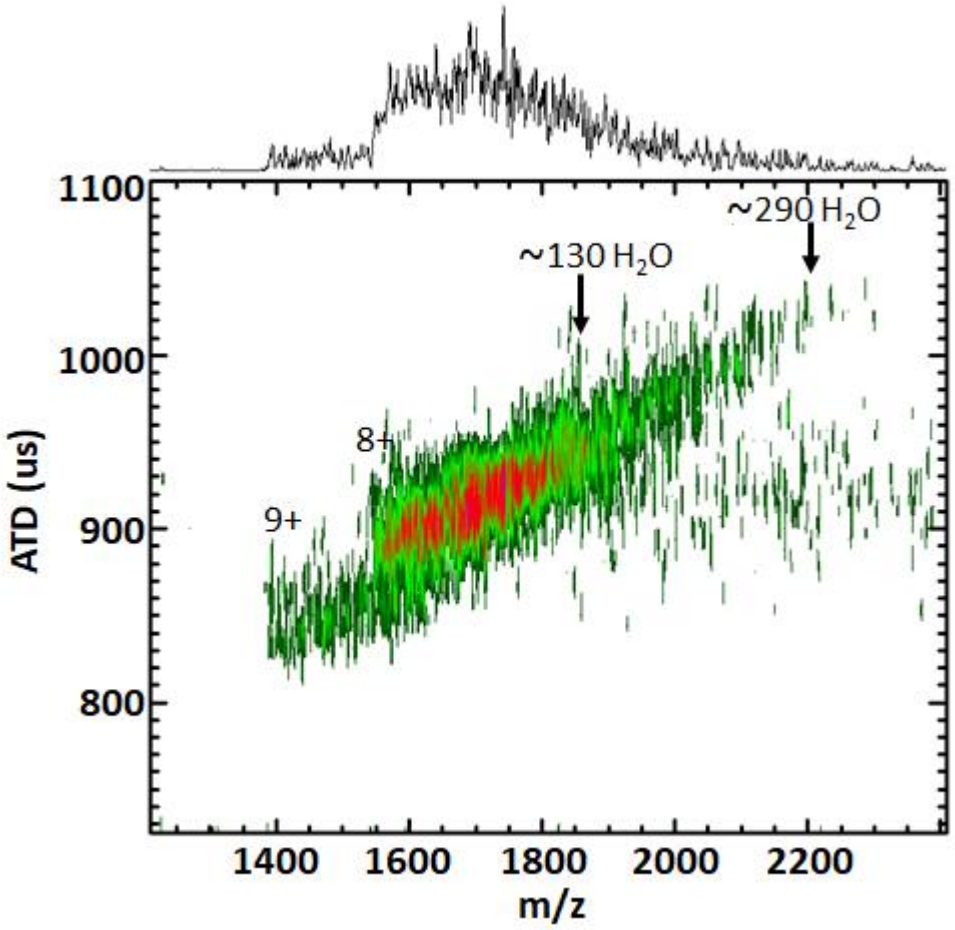

Figure 5.5. ATD vs m/z plot of 30 µM cytochrome c in 18.2 MΩ H_2O. The charge state is marked above each hydration trendline. The number of water molecules adducted to the 8^+ charge state are labelled.

transitions of peptides and proteins at these large (n >100) water cluster sizes will certainly be a considerable leap in answering the question of "for how long, under what conditions, and to what extent, can solution structure be retained without solvent?"[166, 175]

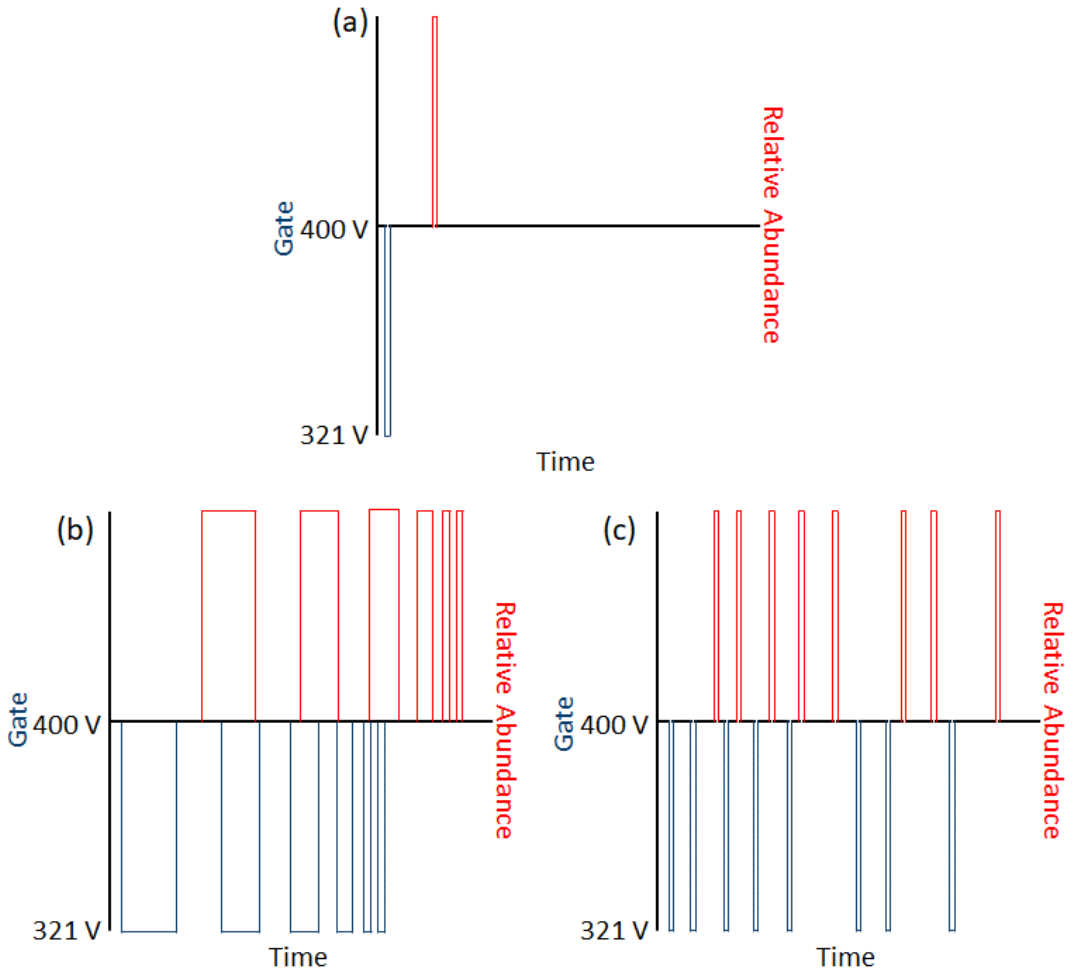

Figure 5.6. (a) A typical IM gating (blue) and signal collection (red) event are compared to two multiplexing methods, (b) a correlation IMS method that opens the gate with increasing frequency and (c) a Hadamard Transform that opens the gate many times per cycle. The two multiplexing methods result in many signal outputs that must be deconvoluted. The gate is open at 321 V and closed at 400 V.

Multiplexing is being employed more frequently to solve the low duty cycle problem inherent to signal averaging for IM-MS. Two multiplexing methods, correlation and Hadamard, have been attempted thus far. **Figure 5.6a** shows the low duty cycle

inherent to the signal averaging method for IM. By increasing the number of gating events, as shown in the Hadamard transform method **Figure 5.6b**, the duty cycle can be increased to ~25-50%. The Hadamard transform method uses a pseudo-random binary sequence to vary the on-off gate voltage. The correlation method, shown in **Figure 5.6c** uses an on-off square waveform that slowly increases in frequency and decreases in gate-width.[176] However, software limitations used for the current home-built instrumentation prevent data acquisition times greater than one second, and the correlation method requires ~8 seconds to allow for enough time-points across each square wave to produce reasonable data. This problem is described by the failure to meet the Nyquist-Shannon sampling theorem, which requires at least 3 points across each square-wave.[177] The Hadamard transform method should be unaffected by these limitations and is currently being investigated for use with cryo-IM-MS. Although simplified in **Figure 5.6**, the resulting

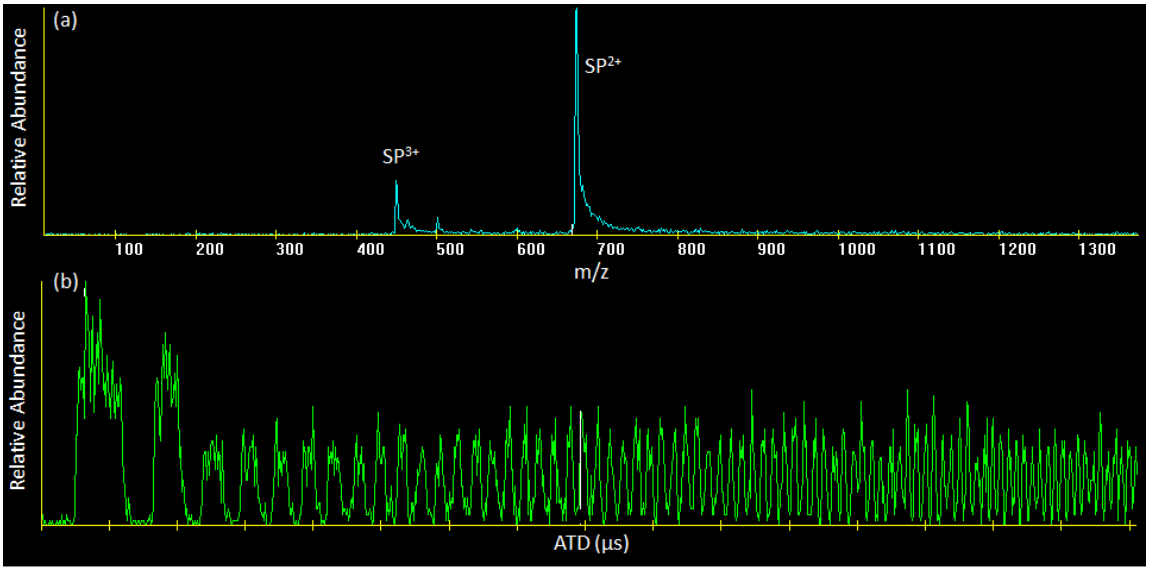

Figure 5.7. (a) Mass spectrum of SP and (b) ATD of SP accumulated under a 1 second correlation multiplexed gate. Note the increasing frequency of the observed signal.

IM data is quite convoluted, as shown from the correlation IMS data obtained in **Figure 5.7**. Signal processing methods are required to correlate the gate opening times with the signal arrival times. Nonetheless, improving the duty cycle 25- to 50-fold will decrease data acquisition timeframe of hours to minutes for an experiment in which the signal is sensitive to time.

5.2. Charge Carrier Effects on ESI

The studies in section **3.3.4** reveal a dependence of the charge carrier on the hydrated ion structures observed, in agreement with previous results.[78, 83, 86, 131, 178] Silveira *et al.* previously suggested that nonspecific hydration provided structural stability for BK ions, whereas GS ions formed specific hydrated ion structures, *i.e.* via the formation of magic number clusters.[60] However, it was shown here that BK^{3+} ions are stabilized when well-hydrated ($n > 40$) and that like-charged ions may be stabilized by water bridges. Furthermore, the analysis of the guanidinium ions shows that $GdmH^{+}$ is capable of supporting an additional charge within the droplet by forming like-charged ion pairs, in agreement with the ability of BK^{3+} to be stable in the presence of excess hydration.

Mutation studies for BK examining the effects of lysine on the charged droplet will determine how late-stage ESI depends on the charge-carrier. Ideally, R1K, R9K, and R1,9K mutations would maintain the same charge locations while only differentiating the charge carrier. Furthermore, these studies could differentiate between the formation of like-charged ion pairs between the two arginine residues, which may enable higher charge states to be investigated in larger droplets. Similarly, a series of SP mutants and truncated SP analogues will be good: RPKP, RPKPQQ, RPKPEE, K3R, R1K. Hydration studies of

RPKP will examine the effects of concentrating the charge, since the $Q^5Q^6F^7F^8$ residues of SP were shown to provide important charge stabilizing interactions.[173] The SP mutants (K3R, R1K) will provide another system to confirm the like-charged ion pair interacts described earlier and may also provide insight into the SP dimer formation shown in the previous section.

Experiments with polyarginine and polylysine have reported different affinities for guanidinium For example, tetra-arginine (R_4) has been reported to form binding interactions with $GdmH^+$, while K_4 does not.[120, 131] IM experiments would be excellent for further examination of guanidinium pairing with peptides and proteins, (*i.e.* $GdmH^+$-$ArgH^+$). However, these peptides will also be excellent candidates to test late-stage ESI processes by extending the hydration as much as possible, as shown for $GdmH^+$-$GdmH^+(H_2O)_n$ and $BK^{3+}(H_2O)_n$, to attempt to observe the hydration leading to droplets with more charge than basic sites, *e.g.* $R_n^{(n+1)+}$. These systems will offer an unprecedented observation of charge states and hydration states that are still be undergoing late-stage evaporative processes, making the nuanced charge differences between $–NH_3^+$ and $–GdmH^+$ charge carriers of considerable interest. Attempting similar studies on larger polyarginine and polylysine peptides may also lead to understanding differences between late stage CRM and IEM, which are generally considered to be size-dependent phenomena.

5.3. Osmolyte Effects on Peptide/Protein Structure

Nanodroplet chemistry in native-MS often lacks the typical complexities of a cell, *e.g.* salts, metabolites, osmolytes, and lipids. Control over solution conditions does offer some recompense to study specific interactions, especially where additives may be "freeze-dried" within a confined nanocluster. Studying these stabilizing osmolyte interactions in the transition from the solution- to the gas-phase will allow for their use in manipulating peptide/protein structure during ESI. The behavior of osmolytes is often dependent upon the protein, and additional osmolytes (*e.g.* betaine, sorbitol, trehalose, and amino acids) will be more reasonable after studying the specific effects of a single osmolyte on several different peptides/proteins.

It is well-supported that osmolytes, such as trimethylammonium N-oxide (TMAO) and urea can act to stabilize or destabilize proteins, but the mechanisms of osmolytes are debated. The recurring question of hydrated mechanisms of interaction has become stylistic of cryo-IM-MS studies: do osmolytes directly interact with proteins or can they affect the nearby environment, *e.g.* causing solvent exclusion to affect stabilization/destabilization? Cryo-IM-MS, which can obtain information about structural waters, can inform on this mechanistic question, especially with its convenient control over solution conditions, including pH, temperature, ionic strength, and osmolyte strengths.

TMAO and urea are well-researched and offer an interesting two-osmolyte system. Urea is known to denature proteins in solution. TMAO is known to stabilize proteins and is used by marine animals that have high concentrations of urea or other destabilizing

factors, such as high pressure.[179] Yancey and Somero reported that TMAO can counteract the high concentration effects of urea,[180] and Canchi *et al.* provided evidence that a 2:1 TMAO:urea ratio was sufficient to counter the denaturing effects of urea.[181] It has been proposed that TMAO H-bonds directly with urea, effectively eliminating urea's deleterious effects.[182] Alternatively, it has been proposed that the hydrophobic trimethyl region creates a solvent excluded volume that would entropically disfavor solvation of the protein backbone, since urea interacts with that region.[183-184] With higher mass resolution, experiments of model proteins in osmolyte solutions are recommended, *e.g.* ubiquitin has well-described activation and unfolding based on well-known solution conditions. Additionally, TMAO is predicted to promote aggregation of amyloidogenic intrinsically disordered peptides (IDPs).[179] While these peptides are generally thought to be intrinsically disordered, the Russell laboratory has shown promising results that their order is, at least partially, conditional on their environments;[185-188] cryo-IM-MS will offer the opportunity to observe the influence of water and osmolytes on IDPs. For now, substance P (SP) was chosen as a model peptide to examine how it interacts with TMAO and urea, since it has two identified structural families, **A** and **B**, which correspond to a well-hydrated solution-phase structure and an unfolded gas-phase structure, respectively shown previously in **Figure 1.8**.

Figure 5.8a shows a typical SP spectrum, which contains $SP^{3+}(H_2O)_n$ and $SP^{2+}(H_2O)_n$. This includes the compact solution-phase and extended gas-phase conformational families of SP^{3+} at ~550 µs and ~600 µs, respectively. The addition of TMAO in **Figure 5.8b** reveals a strong trendline below that of SP^{2+} and SP^{3+} that corresponds to noncovalently bound SP ($2SP^{4+}$). Hydrated $2SP^{4+}$ clusters are supported by the 4.5 m/z separation between peaks, resolved by the increased mass resolution of the

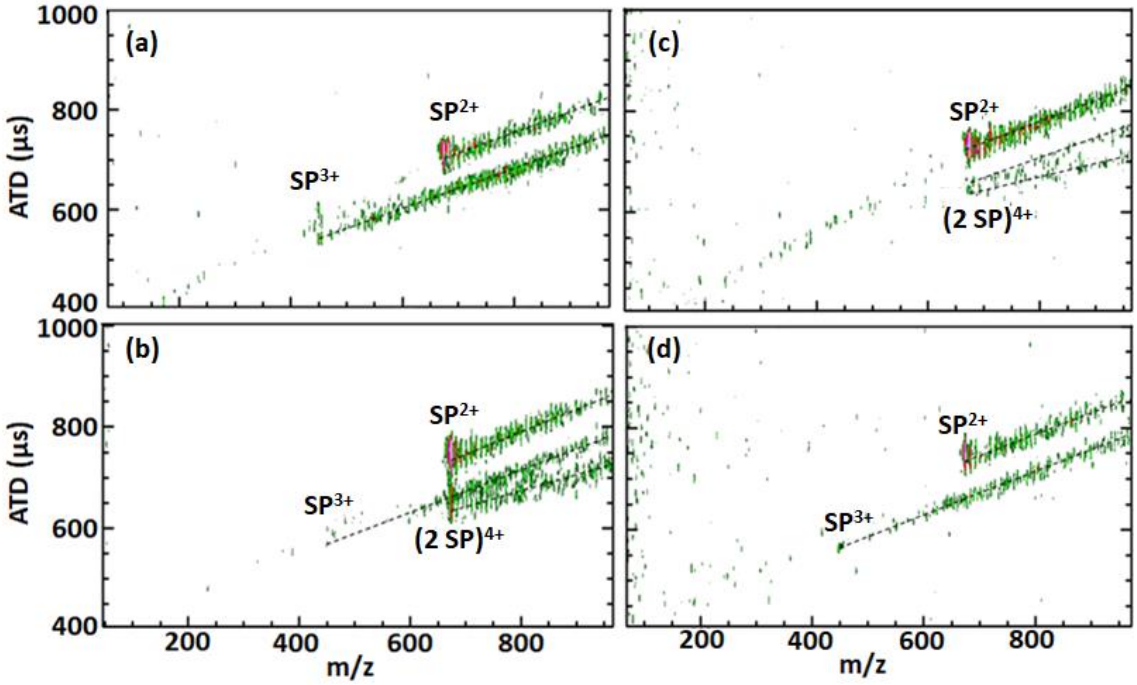

Figure 5.8. ATD vs m/z plots of SP water clusters. Sprayed solutions contain (a) 50 µM SP in water, (b) 50 µM SP in 1 µM TMAO, (c) 50 µM SP in 1 µM TMAO and 1 µM urea, and (d) 50 µM SP in 50 µM urea. Dashed lines show the hydration trendlines of different charge states.

Jordan ToF. The addition of urea seems to decrease the dimerization effect in small 1 µM concentrations of each osmolyte (**Figure 5.8c**) and dimers are not present at all in the presence of only urea (**Figure 5.8d**). The counteracting force urea has on dimer formation supports TMAO-induced dimer formation, but by which mechanism? Some of the

observed dimers contain a single TMAO adduct but are not well hydrated. There are also two other observations worth noting. First, TMAO typically acts as a charge reducer, and the SP^{3+} relative abundance is certainly decreased in the experiments with TMAO present. MDS reported by Bennion and Daggett suggest that TMAO increased H-bonding strengths with H_2O;[184] increased numbers of urea-H_2O and protein-H_2O bonds result from the protectant TMAO. Whether TMAO is acting as a protectant, thereby lowering the solvent accessible surface area (SASA) and charge or by some other charge reduction mechanism is currently unclear. SP-TMAO hydrates were not highly abundant, which may support an indirect mechanism of interaction by TMAO. The concentrations used in this preliminary study are very low, but it will be interesting to use higher concentrations to determine how hydrated SP-TMAO complexes are formed and dissociate. Second, no TMAO-urea complexes were observed, which is surprising considering the theorized TMAO-urea interaction. This indicates that urea is not sequestered by TMAO,[184] but higher concentration studies may be necessary to observe this hydrated ion complex.

Counteraction of the destabilizing effects of urea by the addition of other typically denaturing osmolytes will provide better insight into the intricate interactions between different osmolytes and between osmolytes and water. GdmHCl will be an excellent model system to study since it has been investigated by cryo-IM-MS here.[95] Ganguly *et al*. recently showed a stabilizing interaction upon addition of urea and GdmHCl with MDS for the helical region of a Trp cage protein, whereas individually, either osmolyte is denaturing.[189] The counteracting effects on the water network interacting with the helical region is expected to stabilize the helical structure; the model helical peptides AK_n (Ac-

$(AAKAA)_nY\text{-}NH_2$) have well-described helical content and modelling that would make these peptides an interesting starting point to study counteracting osmolyte-water interactions.[165]

5.4. Hydration of Insulin

Insulin is a highly conserved doubly disulfide bound protein consisting of a 21 amino acid A chain and a 30 amino acid B chain. Insulin has been studied considerably since its discovery as it plays a vital regulatory role in human and animal metabolism. The active form of insulin, the protomer, exists between 57-400 pm in the blood. The protomer is stored as a trimer of dimers, centered around 2 Zn^{2+} ions.[190] The diprotomer, $(AB)_2$, and hexaprotomer, $((AB)_2)_3$, forms are used for long term storage, as they are bulkier, more difficult to transport, and much less active than the monomeric forms. The active form of insulin exists in the body and self-aggregates at such low concentrations that the active form is difficult to study by typical NMR and crystallographic techniques. Although mutants and various solution conditions have been employed previously to study insulin using these methods, there is no simple method with which to study the protomer in its native state.[191-194]

Mass spectrometry has been used previously to determine a k_D of 100 μM for insulin diprotomer.[195] At higher concentrations of insulin, the same study found artifacts from ESI: higher order oligomers up to 12-mers were formed.[195] Generally, as long as low concentrations are maintained, these artifacts can be avoided. Despite this shortcoming, MS offers a significant advantage when analyzing the insulin protomer due to the tendency for insulin to aggregate at low concentrations. Cryo-IM-MS is able to study the structural

dependencies of the protomer and diprotomer on water, analogous to the dissociation of the noncovalent ubiquitin dimer only after near complete dehydration.[101]

There is an asymmetric diprotomer, D^{7+} that can be unambiguously identified in **Figure 5.9a**. The D^{7+} ion has a single major distribution of conformational states. The M^{4+} and M^{3+} charge states each have two major distributions, corresponding to a protomer and diprotomer. The M^{5+} distribution does not appear to follow the diprotomer trendline, and instead the second distribution that arrives at longer ATDs (~1250-1350 µs) is indicative

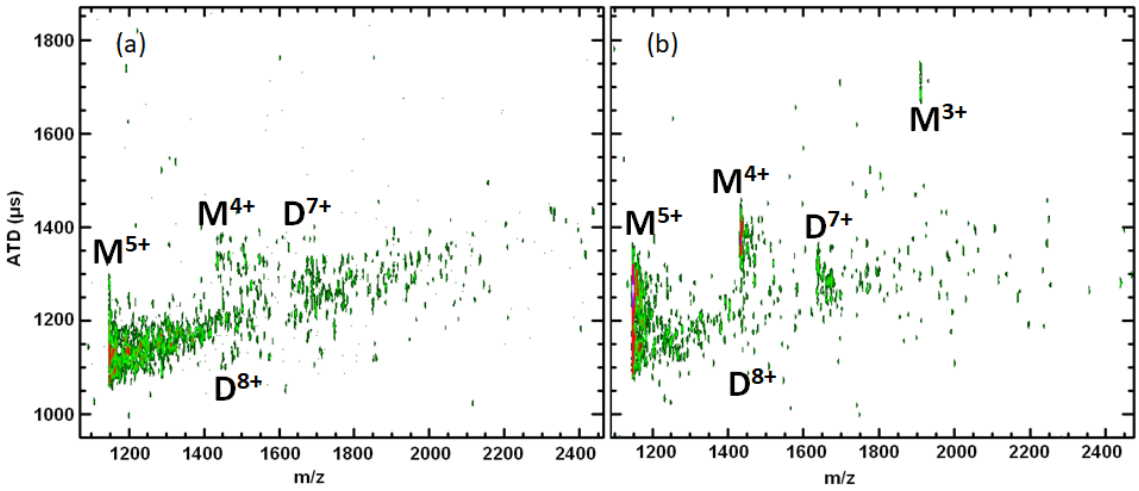

Figure 5.9. ATD vs m/z plots of 25 µM bovine insulin electrosprayed at a heated inlet temperature of (a) 349 K and (B) 355 K. Dehydrated protomer (M^{z+}), diprotomer (D^{z+}), and triprotomer (T^{z+}) ions are labelled.

of unfolding of the M^{5+} ions. Insulin diprotomers do show dissociation upon dehydration. However, the protomer and diprotomer are both hydrated, suggesting that both forms are present in solution. Activation of the diprotomer via increased heated capillary temperatures population leads to the very similar ATDs (~1300-1430 µs) as the evaporative process leads to, suggesting that both light activation and evaporation of the nanodroplet lead to the same conformational families. Alternatively, this may mean that

the evaporating protomer droplet and dissociated diprotomer equilibrate to the same stable gas-phase structure; concern that the promoted protomer state is a stable gas-phase ion, rather than a native-like protomer is reasonable, since dissociation occurs in the gas-phase. However, given the gentle instrument conditions that lead to the formation of the evaporated droplet, it is unlikely that the hydrated protomer trendline leads to a stable gas-phase protomer. Furthermore, formation of a stable gas-phase structure from the dissociated diprotomer would require the loss of hydrophobic binding and electrostatic interactions and require the refolding of the ion all to occur within a μs timescale. Streaking occurs from the D^{8+} to M^{4+} ATD, indicating that the dissociation occurs near the end of ESI, and the observed step-by-step dehydration suggests sequential states are differentiated by small amounts of energy. Thus cryo-IM-MS not only agrees well with the formation of native-like proteins via ESI, but also shows that the same native-like protomer can be obtained via dissociation of a diprotomer.[196] MDS studies are a necessary next step to determining structural characteristics of protomeric and diprotomeric insulin obtained via cryo-IM-MS.

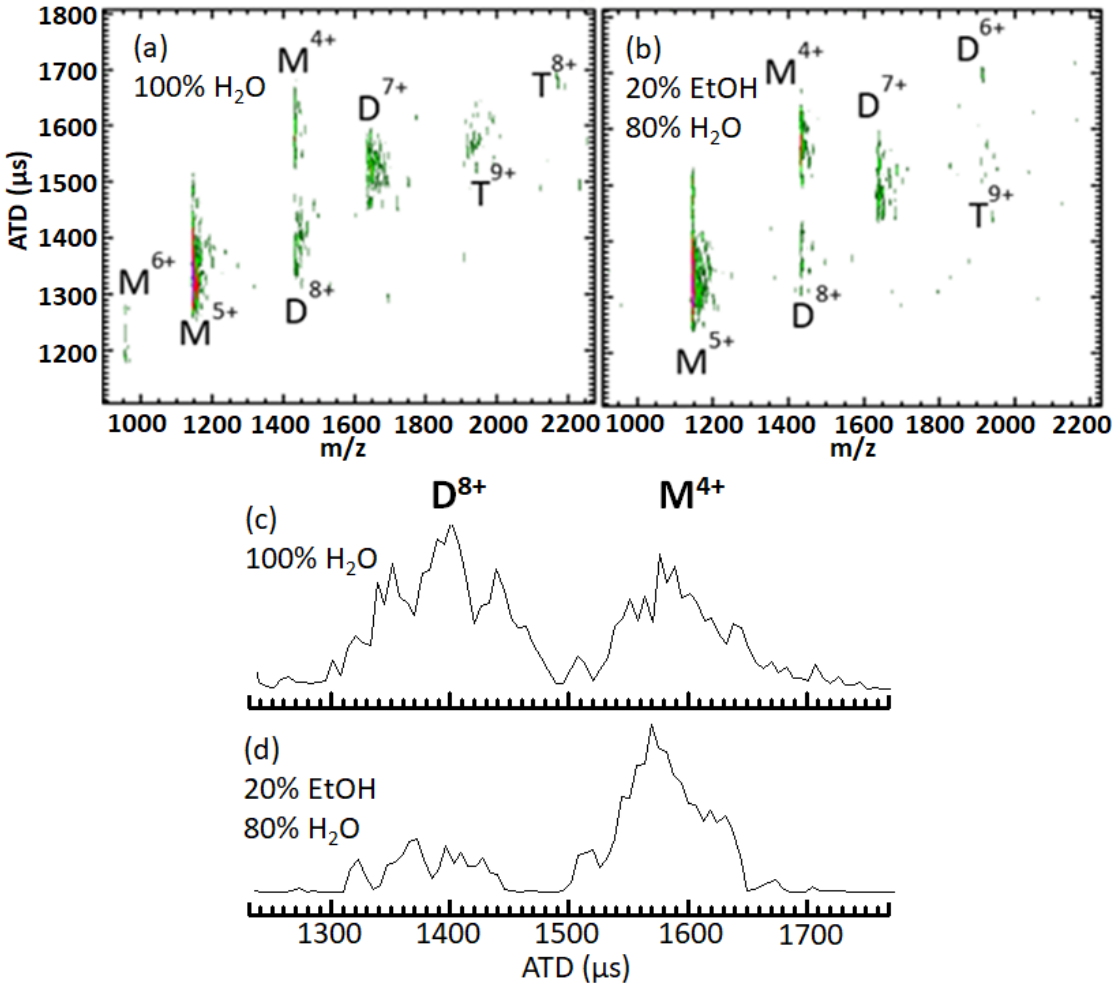

Figure 5.10. (a and b) ATD vs m/z plots of 100 µM bovine insulin in (a) 100% H_2O and (b) 20% ethanol and 80% H_2O. (c and d) ATD of the 1434 m/z peak showing the diprotomer (D^{8+}) and protomer (M^{4+}) IM peaks. The diprotomer is abundant in (c) 100% H_2O solutions and diminished in (d) 20% ethanol 80% H_2O.

Previous studies in water/nonpolar mixtures have shown that the structure of insulin remains mostly intact, but the protomeric state is greatly stabilized (*i.e.* k_D increases).[192-194] The self-association of insulin is driven by close-packed hydrophobic interactions, so this result stems from the ability for insulin protomers to be stabilized by interactions with an apolar solvent, effectively burying its highly nonpolar diprotomer-forming surface area.[197] The results shown in **Figure 5.10** generally agree with this

observation; **Figure 5.10a** and **Figure 5.10b** show a decrease in abundance of the oligomers T^{9+}, T^{8+}, D^{8+}, and D^{7+}. There is a small shift towards protomeric insulin, but it is not the 100 fold increase in k_D predicted by 2D IR studies.[193] The effect on k_D may be decreased due to stabilization of the protomer state that already occurs during droplet formation, since surface of electrosprayed nanodroplets have a readily available nonpolar interface for the diprotomer-forming surface to interact with. Infrared-visible sum frequency generation spectroscopy (SFG) experiments have previously determined that protomers segregate and are the primary form of insulin at the water-air interface, supporting this hypothesis.[198] **Figure 5.10c** and **Figure 5.10d** show little change in drift times of the D^{8+} and M^{4+} peaks, suggesting there is no unfolding when switching from 100% H_2O to 80% H_2O/20% EtOH (v/v). Notably, when unfolding is induced for proteins, ATD differences of more than >100 μs for each charge state are common.

The addition of Zn^{2+} to solution leads to the formation of the hexaprotomer. Time course studies with the addition of Zn^{2+} will lead to a better understanding of the formation of the storage oligomer. Performing these studies will also show the role water plays in the formation of larger oligomers. The observation of hydrated protomer and diprotomer species is suggestive of both states being present in the solution-phase; does the hexaprotomer exist in equilibrium also or is it the dominant structure? Lastly, Mukherjee *et al.* recently determined 10 highly conserved water molecules stabilize the hexamer cavity using MDS,[199] which could likely be retained by utilizing cryo-IM-MS. Confirming the coordination of a number of water clusters in higher relative abundance and performing MDS to determine CCS/structural candidates will provide insight into how

proteins functionally coordinate water in their structures. Although outside the capabilities of the current generation of cryo-IM-MS, these studies may lay the groundwork for very large oligomers, such as GroEL, which can fill its internal cavity with water.[200-201] MDS show that protein folding and refolding within these water-filled cavities can even be accelerated.[201-202] Part of the challenge associated with CCS of proteins requires preventing gas-phase collapse of the protein.[203] Cavities inside the protein are particularly susceptive to collapse and it is unknown to what extent a protein cavity remains intact or collapses as it enters the gas-phase.[204] Extension of CCS onto small proteins and protein complexes, like insulin here, would provide an interesting way to study the extent of gas-phase compaction as a function of the number of hydrating water molecules.

5.5. Project Summary and Outlook

Cryo-IM-MS studies have thus far focused on broad structural details to gain insight into late stage ESI and the formation of gas-phase structures of biological molecules. The studies here have provided an overview of some of the important stabilizing forces in the small water clusters observed. Capturing the transition from solution-phase to gas-phase structures has been supported here by the addition of CCS to the cryo-IM-MS; extending the ability to confirm experimental structures with CCS will continue to enable cryo-IM-MS to provide in-depth analyses on the role of confined water on biological structures. The roles water molecules play in biological systems are vast and complex. With the addition of structural characterization through CCS, an improved duty

cycle, and improved MS resolution, there is great potential for cryo-IM-MS analyses on these hydrated systems.

REFERENCES

1. Thomson, J. J.; Rutherford, E., XL. On the passage of electricity through gases exposed to Röntgen rays. *The London, Edinburgh, and Dublin Philosophical Magazine and Journal of Science* **1896,** *42* (258), 392-407.

2. Zeleny, J., VI. On the ratio of the velocities of the two ions produced in gases by Röntgen radiation; and on some related phenomena. *The London, Edinburgh, and Dublin Philosophical Magazine and Journal of Science* **1898,** *46* (278), 120-154.

3. Tyndall, A. M.; Powell, C. F.; Chattock, A. P., The mobility of ions in pure gases. *Proceedings of the Royal Society of London. Series A, Containing Papers of a Mathematical and Physical Character* **1930,** *129* (809), 162-180.

4. Ewing, R. G.; Atkinson, D. A.; Eiceman, G. A.; Ewing, G. J., A critical review of ion mobility spectrometry for the detection of explosives and explosive related compounds. *Talanta* **2001,** *54* (3), 515-529.

5. Mäkinen, M.; Nousiainen, M.; Sillanpää, M., Ion spectrometric detection technologies for ultra-traces of explosives: A review. *Mass Spectrometry Reviews* **2011,** *30* (5), 940-973.

6. Räsänen, R.-M.; Nousiainen, M.; Peräkorpi, K.; Sillanpää, M.; Polari, L.; Anttalainen, O.; Utriainen, M., Determination of gas phase triacetone triperoxide with aspiration ion mobility spectrometry and gas chromatography–mass spectrometry. *Analytica Chimica Acta* **2008,** *623* (1), 59-65.

7. Verkouteren, J. R.; Staymates, J. L., Reliability of ion mobility spectrometry for qualitative analysis of complex, multicomponent illicit drug samples. *Forensic Science International* **2011,** *206* (1), 190-196.

8. Barnes, W. S.; Martin, D. W.; McDaniel, E. W., Mass Spectrographic Identification of the Ion Observed in Hydrogen Mobility Experiments. *Phys. Rev. Lett.* **1961,** *6* (3), 110-111.

9. McDaniel, E. W.; Martin, D. W.; Barnes, W. S., Drift Tube-Mass Spectrometer for Studies of Low-Energy Ion-Molecule Reactions. *Rev. Sci. Instrum.* **1962,** *33* (1), 2-7.

10. McAfee, K. B.; Edelson, D., Identification and Mobility of Ions in a Townsend Discharge by Time-resolved Mass Spectrometry. *Proceedings of the Physical Society* **1963,** *81* (2), 382-384.

11. Dwivedi, P.; Wu, C.; Matz, L. M.; Clowers, B. H.; Siems, W. F.; Hill, H. H., Gas-Phase Chiral Separations by Ion Mobility Spectrometry. *Anal. Chem.* **2006,** *78* (24), 8200-8206.

12. Clemmer, D. E.; Hudgins, R. R.; Jarrold, M. F., Naked Protein Conformations: Cytochrome c in the Gas Phase. *J. Am. Chem. Soc.* **1995,** *117* (40), 10141-10142.

13. May, J. C.; McLean, J. A., Ion Mobility-Mass Spectrometry: Time-Dispersive Instrumentation. *Anal. Chem.* **2015,** *87* (3), 1422-1436.

14. Poltash, M. L.; McCabe, J. W.; Shirzadeh, M.; Laganowsky, A.; Clowers, B. H.; Russell, D. H., Fourier Transform-Ion Mobility-Orbitrap Mass Spectrometer: A Next-Generation Instrument for Native Mass Spectrometry. *Anal. Chem.* **2018,** *90* (17), 10472-10478.

15. Quintyn, R. S.; Harvey, S. R.; Wysocki, V. H., Illustration of SID-IM-SID (surface-induced dissociation-ion mobility-SID) mass spectrometry: homo and hetero model protein complexes. *Analyst* **2015,** *140* (20), 7012-7019.

16. Yang, Y.; Liu, F.; Franc, V.; Halim, L. A.; Schellekens, H.; Heck, A. J. R., Hybrid mass spectrometry approaches in glycoprotein analysis and their usage in scoring biosimilarity. *Nature Communications* **2016,** *7* (1), 13397.

17. Franc, V.; Zhu, J.; Heck, A. J. R., Comprehensive Proteoform Characterization of Plasma Complement Component C8αβγ by Hybrid Mass Spectrometry Approaches. *J. Am. Soc. Mass Spectrom.* **2018,** *29* (6), 1099-1110.

18. Poltash, M. L.; McCabe, J. W.; Shirzadeh, M.; Laganowsky, A.; Russell, D. H., Native IM-Orbitrap MS: Resolving what was hidden. *TrAC Trends in Analytical Chemistry* **2020,** *124*, 115533.

19. Poltash, M. L.; Shirzadeh, M.; McCabe, J. W.; Moghadamchargari, Z.; Laganowsky, A.; Russell, D. H., New insights into the metal-induced oxidative degradation pathways of transthyretin. *Chemical Communications* **2019,** *55* (28), 4091-4094.

20. Poltash, M. L.; McCabe, J. W.; Patrick, J. W.; Laganowsky, A.; Russell, D. H., Development and Evaluation of a Reverse-Entry Ion Source Orbitrap Mass Spectrometer. *J. Am. Soc. Mass Spectrom.* **2019,** *30* (1), 192-198.

21. Laganowsky, A.; Reading, E.; Hopper, J. T. S.; Robinson, C. V., Mass spectrometry of intact membrane protein complexes. *Nature Protocols* **2013,** *8* (4), 639-651.

22. Gault, J.; Donlan, J. A. C.; Liko, I.; Hopper, J. T. S.; Gupta, K.; Housden, N. G.; Struwe, W. B.; Marty, M. T.; Mize, T.; Bechara, C.; Zhu, Y.; Wu, B.; Kleanthous, C.; Belov, M.; Damoc, E.; Makarov, A.; Robinson, C. V., High-resolution mass spectrometry of small molecules bound to membrane proteins. *Nature Methods* **2016,** *13* (4), 333-336.

23. Patrick, J. W.; Boone, C. D.; Liu, W.; Conover, G. M.; Liu, Y.; Cong, X.; Laganowsky, A., Allostery revealed within lipid binding events to membrane proteins. *Proc. Natl. Acad. Sci. U.S.A.* **2018,** *115* (12), 2976-2981.

24. Cong, X.; Liu, Y.; Liu, W.; Liang, X.; Russell, D. H.; Laganowsky, A., Determining Membrane Protein–Lipid Binding Thermodynamics Using Native Mass Spectrometry. *J. Am. Chem. Soc.* **2016,** *138* (13), 4346-4349.

25. Karas, M.; Hillenkamp, F., Laser desorption ionization of proteins with molecular masses exceeding 10,000 daltons. *Anal. Chem.* **1988,** *60* (20), 2299-2301.

26. Tanaka, K.; Waki, H.; Ido, Y.; Akita, S.; Yoshida, Y.; Yoshida, T.; Matsuo, T., Protein and polymer analyses up to m/z 100 000 by laser ionization time-of-flight mass spectrometry. *Rapid Communications in Mass Spectrometry* **1988,** *2* (8), 151-153.

27. Yamashita, M.; Fenn, J. B., Electrospray ion source. Another variation on the free-jet theme. *J. Phys. Chem.* **1984,** *88* (20), 4451-4459.

28. Dole, M.; Mack, L. L.; Hines, R. L.; Mobley, R. C.; Ferguson, L. D.; Alice, M. B., Molecular Beams of Macroions. *The Journal of Chemical Physics* **1968,** *49* (5), 2240-2249.

29. Mack, L. L.; Kralik, P.; Rheude, A.; Dole, M., Molecular Beams of Macroions. II *J. Chem. Phys.* **1970,** *52*, 4977-4986.

30. Katta, V.; Rockwood, A. L.; Vestal, M. L., Field limit for ion evaporation from charged thermospray droplets. *International Journal of Mass Spectrometry and Ion Processes* **1991,** *103* (2), 129-148.

31. Ganem, B.; Li, Y. T.; Henion, J. D., Detection of noncovalent receptor-ligand complexes by mass spectrometry. *J. Am. Chem. Soc.* **1991,** *113* (16), 6294-6296.

32. Camilleri, P.; Haskins, N. J., Investigating the non-covalent interaction of cytidylic acids, with Ribonuclease A by electrospray mass spectrometry. *Rapid Communications in Mass Spectrometry* **1993,** *7* (7), 603-604.

33. Iribarne, J. V.; Thomson, B. A., On the evaporation of small ions from charged droplets. *The Journal of Chemical Physics* **1976,** *64* (6), 2287-2294.

34. Thomson, B. A.; Iribarne, J. V., Field induced ion evaporation from liquid surfaces at atmospheric pressure. *The Journal of Chemical Physics* **1979,** *71* (11), 4451-4463.

35. Kebarle, P.; Verkerk, U. H., Electrospray: From ions in solution to ions in the gas phase, what we know now. *Mass Spectrometry Reviews* **2009,** *28* (6), 898-917.

36. Mack, L. L.; Kralik, P.; Rheude, A.; Dole, M., Molecular Beams of Macroions. II. *The Journal of Chemical Physics* **1970,** *52* (10), 4977-4986.

37. Fernandez de la Mora, J., Electrospray ionization of large multiply charged species proceeds via Dole's charged residue mechanism. *Anal. Chim. Acta* **2000,** *406* (1), 93-104.

38. Lee, S.-W.; Freivogel, P.; Schindler, T.; Beauchamp, J. L., Freeze-Dried Biomolecules: FT-ICR Studies of the Specific Solvation of Functional Groups and Clathrate Formation Observed by the Slow Evaporation of Water from Hydrated Peptides and Model Compounds in the Gas Phase. *J. Am. Chem. Soc.* **1998,** *120* (45), 11758-11765.

39. Iavarone, A. T.; Williams, E. R., Mechanism of Charging and Supercharging Molecules in Electrospray Ionization. *J. Am. Chem. Soc.* **2003,** *125* (8), 2319-2327.

40. Nguyen, S.; Fenn, J. B., Gas-phase ions of solute species from charged droplets of solutions. *Proc. Natl. Acad. Sci. U.S.A.* **2007,** *104* (4), 1111-1117.

41. Konermann, L.; McAllister, R. G.; Metwally, H., Molecular Dynamics Simulations of the Electrospray Process: Formation of NaCl Clusters via the Charged Residue Mechanism. *J. Phys. Chem. B* **2014,** *118* (41), 12025-12033.

42. Meng, C. K.; Fenn, J. B., Formation of charged clusters during electrospray ionization of organic solute species. *Organic Mass Spectrometry* **1991,** *26* (6), 542-549.

43. Juraschek, R.; Dülcks, T.; Karas, M., Nanoelectrospray—More than just a minimized-flow electrospray ionization source. *J. Am. Soc. Mass Spectrom.* **1999,** *10* (4), 300-308.

44. Wang, G.; Cole, R. B., Solvation Energy and Gas-Phase Stability Influences on Alkali Metal Cluster Ion Formation in Electrospray Ionization Mass Spectrometry. *Anal. Chem.* **1998,** *70* (5), 873-881.

45. Wang, G.; Cole, R. B., Charged residue versus ion evaporation for formation of alkali metal halide cluster ions in ESI. *Anal. Chim. Acta* **2000,** *406* (1), 53-65.

46. Hogan, C. J.; Carroll, J. A.; Rohrs, H. W.; Biswas, P.; Gross, M. L., Charge Carrier Field Emission Determines the Number of Charges on Native State Proteins in Electrospray Ionization. *J. Am. Chem. Soc.* **2008,** *130* (22), 6926-6927.

47. Hogan, C. J.; Carroll, J. A.; Rohrs, H. W.; Biswas, P.; Gross, M. L., Combined Charged Residue-Field Emission Model of Macromolecular Electrospray Ionization. *Anal. Chem.* **2009,** *81* (1), 369-377.

48. Ahadi, E.; Konermann, L., Modeling the Behavior of Coarse-Grained Polymer Chains in Charged Water Droplets: Implications for the Mechanism of Electrospray Ionization. *The Journal of Physical Chemistry B* **2012,** *116* (1), 104-112.

49. Konermann, L.; Rodriguez, A. D.; Liu, J., On the Formation of Highly Charged Gaseous Ions from Unfolded Proteins by Electrospray Ionization. *Analytical Chemistry* **2012,** *84* (15), 6798-6804.

50. Konermann, L.; Ahadi, E.; Rodriguez, A. D.; Vahidi, S., Unraveling the Mechanism of Electrospray Ionization. *Analytical Chemistry* **2013,** *85* (1), 2-9.

51. Ahadi, E.; Konermann, L., Ejection of Solvated Ions from Electrosprayed Methanol/Water Nanodroplets Studied by Molecular Dynamics Simulations. *J. Am. Chem. Soc.* **2011,** *133* (24), 9354-9363.

52. Consta, S., Fragmentation reactions of charged aqueous clusters. *Journal of Molecular Structure: THEOCHEM* **2002,** *591* (1), 131-140.

53. Consta, S., Manifestation of Rayleigh Instability in Droplets Containing Multiply Charged Macroions. *J. Phys. Chem. B* **2010,** *114* (16), 5263-5268.

54. Consta, S.; Malevanets, A., Manifestations of Charge Induced Instability in Droplets Effected by Charged Macromolecules. *Phys. Rev. Lett.* **2012,** *109* (14), 148301.

55. Consta, S.; Oh, M. I.; Malevanets, A., New mechanisms of macroion-induced disintegration of charged droplets. *Chem. Phys. Lett.* **2016,** *663* (Supplement C), 1-12.

56. Oh, M. I.; Consta, S., What factors determine the stability of a weak protein–protein interaction in a charged aqueous droplet? *Physical Chemistry Chemical Physics* **2017,** *19* (47), 31965-31981.

57. Sharawy, M.; Consta, S., Characterization of "Star" Droplet Morphologies Induced by Charged Macromolecules. *J. Phys. Chem. A* **2016,** *120* (44), 8871-8880.

58. Ichiki, K.; Consta, S., Disintegration Mechanisms of Charged Aqueous Nanodroplets Studied by Simulations and Analytical Models. *J. Phys. Chem. B* **2006,** *110* (39), 19168-19175.

59. May, J.; Russell, D., A Mass-Selective Variable-Temperature Drift Tube Ion Mobility-Mass Spectrometer for Temperature Dependent Ion Mobility Studies. *J. Am. Soc. Mass Spectrom.* **2011,** *22* (7), 1134-1145.

60. Silveira, J. A.; Servage, K. A.; Gamage, C. M.; Russell, D. H., Cryogenic Ion Mobility-Mass Spectrometry Captures Hydrated Ions Produced During Electrospray Ionization. *J. Phys. Chem. A* **2013,** *117* (5), 953-961.

61. Lee, S.-W.; Freivogel, P.; Schindler, T.; Beauchamp, J. L., Freeze-Dried Biomolecules: FT-ICR Studies of the Specific Solvation of Functional Groups and Clathrate Formation Observed by the Slow Evaporation of Water from Hydrated Peptides and Model Compounds in the Gas Phase. *Journal of the American Chemical Society* **1998,** *120* (45), 11758-11765.

62. Wyttenbach, T.; Bowers, M. T., Hydration of biomolecules. *Chem. Phys. Lett.* **2009,** *480* (1–3), 1-16.

63. Wyttenbach, T.; Liu, D.; Bowers, M. T., Hydration of small peptides. *International Journal of Mass Spectrometry* **2005,** *240* (3), 221-232.

64. Fye, J. L.; Woenckhaus, J.; Jarrold, M. F., Hydration of Folded and Unfolded Gas-Phase Proteins: Saturation of Cytochrome c and Apomyoglobin. *J. Am. Chem. Soc.* **1998,** *120* (6), 1327-1328.

65. Voss, J. M.; Fischer, K. C.; Garand, E., Accessing the Vibrational Signatures of Amino Acid Ions Embedded in Water Clusters. *The Journal of Physical Chemistry Letters* **2018,** *9* (9), 2246-2250.

66. Kwantwi-Barima, P.; Hogan, C. J.; Clowers, B. H., Deducing Proton-Bound Heterodimer Association Energies from Shifts in Ion Mobility Arrival Time Distributions. *The Journal of Physical Chemistry A* **2019,** *123* (13), 2957-2965.

67. Thomas, J. M.; He, S.; Larriba-Andaluz, C.; DePalma, J. W.; Johnston, M. V.; Hogan Jr, C. J., Ion mobility spectrometry-mass spectrometry examination of the structures, stabilities, and extents of hydration of dimethylamine–sulfuric acid clusters. *Physical Chemistry Chemical Physics* **2016,** *18* (33), 22962-22972.

68. Ahonen, L.; Li, C.; Kubečka, J.; Iyer, S.; Vehkamäki, H.; Petäjä, T.; Kulmala, M.; Hogan Jr, C. J., Ion Mobility-Mass Spectrometry of Iodine Pentoxide–Iodic Acid Hybrid Cluster Anions in Dry and Humidified Atmospheres. *The Journal of Physical Chemistry Letters* **2019,** *10* (8), 1935-1941.

69. Fournier, J. A.; Wolke, C. T.; Johnson, C. J.; Johnson, M. A.; Heine, N.; Gewinner, S.; Schöllkopf, W.; Esser, T. K.; Fagiani, M. R.; Knorke, H.; Asmis, K. R., Site-specific vibrational spectral signatures of water molecules in the magic H₃O⁺(H₂O)₂₀ and Cs⁺(H₂O)₂₀ clusters. *Proc. Natl. Acad. Sci. U.S.A.* **2014,** *111* (51), 18132-18137.

70. Singh, N. J.; Park, M.; Min, S. K.; Suh, S. B.; Kim, K. S., Magic and Antimagic Protonated Water Clusters: Exotic Structures with Unusual Dynamic Effects. *Angew. Chem. Int. Ed.* **2006,** *45* (23), 3795-3800.

71. Mizuse, K.; Fujii, A., Structural Origin of the Antimagic Number in Protonated Water Clusters H+(H2O)n: Spectroscopic Observation of the “Missing” Water Molecule in the Outermost Hydration Shell. *J. Phys. Chem. Lett.* **2011,** *2* (17), 2130-2134.

72. Diken, E. G.; Hammer, N. I.; Johnson, M. A.; Christie, R. A.; Jordan, K. D., Mid-infrared characterization of the NH4+·(H2O)n clusters in the neighborhood of the n=20 “magic” number. *J. Chem. Phys.* **2005,** *123* (16), 164309.

73. Miyazaki, M.; Fujii, A.; Ebata, T.; Mikami, N., Infrared Spectroscopic Evidence for Protonated Water Clusters Forming Nanoscale Cages. *Science* **2004,** *304* (5674), 1134-1137.

74. Bush, M. F.; Saykally, R. J.; Williams, E. R., Hydration of the Calcium Dication: Direct Evidence for Second Shell Formation from Infrared Spectroscopy. *ChemPhysChem* **2007,** *8* (15), 2245-2253.

75. Shin, J.-W.; Hammer, N. I.; Diken, E. G.; Johnson, M. A.; Walters, R. S.; Jaeger, T. D.; Duncan, M. A.; Christie, R. A.; Jordan, K. D., Infrared Signature of Structures Associated with the H+(H2O)n (n = 6 to 27) Clusters. *Science* **2004,** *304* (5674), 1137-1140.

76. Jiang, J.-C.; Wang, Y.-S.; Chang, H.-C.; Lin, S. H.; Lee, Y. T.; Niedner-Schatteburg, G.; Chang, H.-C., Infrared Spectra of H+(H2O)5-8 Clusters: Evidence for Symmetric Proton Hydration. *J. Am. Chem. Soc.* **2000,** *122* (7), 1398-1410.

77. Cooper, R. J.; Heiles, S.; DiTucci, M. J.; Williams, E. R., Hydration of Guanidinium: Second Shell Formation at Small Cluster Size. *J. Phys. Chem. A* **2014,** *118* (30), 5657-5666.

78. Chang, T. M.; Prell, J. S.; Warrick, E. R.; Williams, E. R., Where's the Charge? Protonation Sites in Gaseous Ions Change with Hydration. *J. Am. Chem. Soc.* **2012,** *134* (38), 15805-15813.

79. Demireva, M.; O'Brien, J. T.; Williams, E. R., Water-Induced Folding of 1,7-Diammoniumheptane. *J. Am. Chem. Soc.* **2012,** *134* (27), 11216-11224.

80. Bush, M. F.; Prell, J. S.; Saykally, R. J.; Williams, E. R., One Water Molecule Stabilizes the Cationized Arginine Zwitterion. *J. Am. Chem. Soc.* **2007,** *129* (44), 13544-13553.

81. Forbes, M. W.; Bush, M. F.; Polfer, N. C.; Oomens, J.; Dunbar, R. C.; Williams, E. R.; Jockusch, R. A., Infrared Spectroscopy of Arginine Cation Complexes: Direct Observation of Gas-Phase Zwitterions. *J. Phys. Chem. A* **2007,** *111* (46), 11759-11770.

82. Ling, S.; Yu, W.; Huang, Z.; Lin, Z.; Harañczyk, M.; Gutowski, M., Gaseous Arginine Conformers and Their Unique Intramolecular Interactions. *J. Phys. Chem. A* **2006,** *110* (44), 12282-12291.

83. Lee, N.; Keesee, R. G.; Castleman Jr, A. W., On the correlation of total and partial enthalpies of ion solvation and the relationship to the energy barrier to nucleation. *Journal of Colloid and Interface Science* **1980,** *75* (2), 555-565.

84. Khan, A., Theoretical studies of large water clusters: (H2O)(28), (H2O)(29), (H2O)(30), and (H2O)(31) hexakaidecahedral structures. *J. Chem. Phys.* **1997,** *106* (13), 5537-5540.

85. Cooper, R. J.; Chang, T. M.; Williams, E. R., Hydrated Alkali Metal Ions: Spectroscopic Evidence for Clathrates. *J. Phys. Chem. A* **2013,** *117* (30), 6571-6579.

86. Chang, T. M.; Cooper, R. J.; Williams, E. R., Locating Protonated Amines in Clathrates. *J. Am. Chem. Soc.* **2013,** *135* (Copyright (C) 2013 American Chemical Society (ACS). All Rights Reserved.), 14821-14830.

87. Lin, C.-K.; Wu, C.-C.; Wang, Y.-S.; Lee, Y. T.; Chang, H.-C.; Kuo, J.-L.; Klein, M. L., Vibrational predissociation spectra and hydrogen-bond topologies of H+(H2O)9–11. *Physical Chemistry Chemical Physics* **2005,** *7* (5), 938-944.

88. Wong, R. L.; Paech, K.; Williams, E. R., Blackbody infrared radiative dissociation at low temperature: hydration of X2+(H2O)n, for X = Mg, Ca. *Int. J. Mass Spectrom.* **2004,** *232* (1), 59-66.

89. Mizuse, K.; Fujii, A., Tuning of the Internal Energy and Isomer Distribution in Small Protonated Water Clusters H+(H2O)4–8: An Application of the Inert Gas Messenger Technique. *J. Phys. Chem. A* **2012,** *116* (20), 4868-4877.

90. Mizuse, K.; Fujii, A., Infrared photodissociation spectroscopy of H+(H2O)6·Mm (M = Ne, Ar, Kr, Xe, H2, N2, and CH4): messenger-dependent balance between H3O+ and H5O2+ core isomers. *Physical Chemistry Chemical Physics* **2011,** *13* (15), 7129-7135.

91. Servage, K. A.; Silveira, J. A.; Fort, K. L.; Russell, D. H., Evolution of Hydrogen-Bond Networks in Protonated Water Clusters H+(H2O)n (n = 1 to 120) Studied by Cryogenic Ion Mobility-Mass Spectrometry. *J. Phys. Chem. Lett.* **2014,** *5* (11), 1825-1830.

92. Mesleh, M. F.; Hunter, J. M.; Shvartsburg, A. A.; Schatz, G. C.; Jarrold, M. F., Structural Information from Ion Mobility Measurements: Effects of the Long-Range Potential. *J. Phys. Chem.* **1996,** *100* (40), 16082-16086.

93. Rodriguez-Cruz, S. E.; Klassen, J. S.; Williams, E. R., Hydration of Gas-Phase Gramicidin S (M + 2H)2+ Ions Formed by Electrospray: The Transition From Solution to Gas-Phase Structure. *J. Am. Soc. Mass Spectrom.* **1997,** *8* (5), 565-568.

94. Wyttenbach, T.; Liu, D.; Bowers, M. T., Hydration of small peptides. *Int. J. Mass Spectrom.* **2005,** *240* (3), 221-232.

95. Hebert, M. J.; Russell, D. H., Hydration of Guanidinium Ions: An Experimental Search for Like-Charged Ion Pairs. *J. Phys. Chem. Lett.* **2019,** *10* (6), 1349-1354.

96. Tian, Z.; Kass, S. R., Gas-Phase versus Liquid-Phase Structures by Electrospray Ionization Mass Spectrometry. *Angew. Chem. Int. Ed.* **2009,** *48* (7), 1321-1323.

97. Campbell, J. L.; Le Blanc, J. C. Y.; Schneider, B. B., Probing Electrospray Ionization Dynamics Using Differential Mobility Spectrometry: The Curious Case of 4-Aminobenzoic Acid. *Anal. Chem.* **2012,** *84* (18), 7857-7864.

98. Patrick, A. L.; Cismesia, A. P.; Tesler, L. F.; Polfer, N. C., Effects of ESI conditions on kinetic trapping of the solution-phase protonation isomer of p-aminobenzoic acid in the gas phase. *Int. J. Mass Spectrom.* **2017,** *418*, 148-155.

99. Cismesia, A. P.; Nicholls, G. R.; Polfer, N. C., Amine vs. carboxylic acid protonation in ortho-, meta-, and para-aminobenzoic acid: An IRMPD spectroscopy study. *Journal of Molecular Spectroscopy* **2017,** *332*, 79-85.

100. Silveira, J. A.; Fort, K. L.; Kim, D.; Servage, K. A.; Pierson, N. A.; Clemmer, D. E.; Russell, D. H., From Solution to the Gas Phase: Stepwise Dehydration and Kinetic Trapping of Substance P Reveals the Origin of Peptide Conformations. *J. Am. Chem. Soc.* **2013,** *135* (51), 19147-19153.

101. Servage, K. A.; Silveira, J. A.; Fort, K. L.; Clemmer, D. E.; Russell, D. H., Water-Mediated Dimerization of Ubiquitin Ions Captured by Cryogenic Ion Mobility-Mass Spectrometry. *J. Phys. Chem. Lett.* **2015,** *6* (24), 4947-4951.

102. Nagornova, N. S.; Rizzo, T. R.; Boyarkin, O. V., Interplay of Intra- and Intermolecular H-Bonding in a Progressively Solvated Macrocyclic Peptide. *Science* **2012,** *336* (6079), 320-323.

103. Searcy, J. Q.; Fenn, J. B., Clustering of water on hydrated protons in a supersonic free jet expansion. *J. Chem. Phys.* **1974,** *61*, 5282-5288.

104. Servage, K. A.; Fort, K. L.; Silveira, J. A.; Shi, L.; Clemmer, D. E.; Russell, D. H., Unfolding of Hydrated Alkyl Diammonium Cations Revealed by Cryogenic Ion Mobility-Mass Spectrometry. *J. Am. Chem. Soc.* **2015,** *137* (28), 8916-8919.

105. Liu, Z.; Zhang, W.-P.; Xing, Q.; Ren, X.; Liu, M.; Tang, C., Noncovalent Dimerization of Ubiquitin. *Angew. Chem. Int. Ed.* **2012,** *51* (2), 469-472.

106. Wagner, N. D.; Russell, D. H., Defining Noncovalent Ubiquitin Homodimer Interfacial Interactions through Comparisons with Covalently Linked Diubiquitin. *J. Am. Chem. Soc.* **2016,** *138* (51), 16588-16591.

107. Wagner, N. D.; Clemmer, D. E.; Russell, D. H., ESI-IM-MS and Collision-Induced Unfolding That Provide Insight into the Linkage-Dependent Interfacial Interactions of Covalently Linked Diubiquitin. *Anal. Chem.* **2017,** *89* (18), 10094-10103.

108. Pratt, L. R.; Chandler, D., Theory of the hydrophobic effect. *J. Chem. Phys.* **1977,** *67* (8), 3683-3704.

109. Lum, K.; Chandler, D.; Weeks, J. D., Hydrophobicity at Small and Large Length Scales. *J. Phys. Chem. B* **1999,** *103* (22), 4570-4577.

110. Chandler, D., Hydrophobicity: Two faces of water. *Nature* **2002,** *417* (6888), 491-491.

111. Chothia, C., Structural invariants in protein folding. *Nature* **1975,** *254*, 304.

112. O'Brien, E. P.; Dima, R. I.; Brooks, B.; Thirumalai, D., Interactions between Hydrophobic and Ionic Solutes in Aqueous Guanidinium Chloride and Urea Solutions: Lessons for Protein Denaturation Mechanism. *J. Am. Chem. Soc.* **2007,** *129* (23), 7346-7353.

113. Mason, P. E.; Brady, J. W.; Neilson, G. W.; Dempsey, C. E., The Interaction of Guanidinium Ions with a Model Peptide. *Biophys. J.* **2007,** *93* (1), L04-L06.

114. Dempsey, C. E.; Piggot, T. J.; Mason, P. E., Dissecting Contributions to the Denaturant Sensitivities of Proteins. *Biochemistry* **2005,** *44* (2), 775-781.

115. Mason, P. E.; Dempsey, C. E.; Neilson, G. W.; Kline, S. R.; Brady, J. W., Preferential Interactions of Guanidinum Ions with Aromatic Groups over Aliphatic Groups. *J. Am. Chem. Soc.* **2009,** *131* (46), 16689-16696.

116. Magalhaes, A.; Maigret, B.; Hoflack, J.; Gomes, J. N. F.; Scheraga, H. A., Contribution of unusual Arginine-Arginine short-range interactions to stabilization and recognition in proteins. *J. Prot. Chem.* **1994,** *13* (2), 195-215.

117. No, K. T.; Nam, K.-Y.; Scheraga, H. A., Stability of Like and Oppositely Charged Organic Ion Pairs in Aqueous Solution. *J. Am. Chem. Soc.* **1997,** *119* (52), 12917-12922.

118. Allolio, C.; Baxova, K.; Vazdar, M.; Jungwirth, P., Guanidinium Pairing Facilitates Membrane Translocation. *J. Phys. Chem. B* **2016,** *120* (1), 143-153.

119. Li, L.; Vorobyov, I.; Allen, T. W., The Different Interactions of Lysine and Arginine Side Chains with Lipid Membranes. *J. Phys. Chem. B* **2013,** *117* (40), 11906-11920.

120. Vazdar, M.; Heyda, J.; Mason, P. E.; Tesei, G.; Allolio, C.; Lund, M.; Jungwirth, P., Arginine "Magic": Guanidinium Like-Charge Ion Pairing from Aqueous Salts to Cell Penetrating Peptides. *Accounts of Chemical Research* **2018,** *51* (6), 1455-1464.

121. Boudon, S.; Wipff, G.; Maigret, B., Monte Carlo simulations on the like-charged guanidinium-guanidinium ion pair in water. *J. Phys. Chem.* **1990,** *94* (15), 6056-6061.

122. Shih, O.; England, A. H.; Dallinger, G. C.; Smith, J. W.; Duffey, K. C.; Cohen, R. C.; Prendergast, D.; Saykally, R. J., Cation-cation contact pairing in water: Guanidinium. *J. Chem. Phys.* **2013,** *139* (3), 035104.

123. Vazdar, M.; Vymětal, J.; Heyda, J.; Vondrášek, J.; Jungwirth, P., Like-Charge Guanidinium Pairing from Molecular Dynamics and Ab Initio Calculations. *J. Phys. Chem. A* **2011,** *115* (41), 11193-11201.

124. Vazdar, M.; Uhlig, F.; Jungwirth, P., Like-Charge Ion Pairing in Water: An Ab Initio Molecular Dynamics Study of Aqueous Guanidinium Cations. *J. Phys. Chem. Lett.* **2012,** *3* (15), 2021-2024.

125. Wernersson, E.; Heyda, J.; Vazdar, M.; Lund, M.; Mason, P. E.; Jungwirth, P., Orientational Dependence of the Affinity of Guanidinium Ions to the Water Surface. *J. Phys. Chem. B* **2011,** *115* (Copyright (C) 2013 American Chemical Society (ACS). All Rights Reserved.), 12521-12526.

126. Dang, L. X.; Pettitt, B. M., Chloride ion pairs in water. *Journal of the American Chemical Society* **1987,** *109* (18), 5531-5532.

127. Dang, L. X.; Pettitt, B. M., Solvated chloride ions at contact. *The Journal of Chemical Physics* **1987,** *86* (11), 6560-6561.

128. Pettitt, B. M.; Rossky, P. J., Alkali halides in water: Ion–solvent correlations and ion–ion potentials of mean force at infinite dilution. *The Journal of Chemical Physics* **1986,** *84* (10), 5836-5844.

129. Tabushi, I.; Kiyosuke, Y.; Yamamura, K., A novel mode of protein-protein interaction. Water bridged cation-cation interaction in trypsin-inhibitor complex. *Journal of the American Chemical Society* **1981,** *103* (17), 5255-5257.

130. Brünger, A. T.; Brooks, C. L.; Karplus, M., Active site dynamics of ribonuclease. *Proc. Natl. Acad. Sci. U.S.A.* **1985,** *82* (24), 8458-8462.

131. Kubíčková, A.; Křížek, T.; Coufal, P.; Wernersson, E.; Heyda, J.; Jungwirth, P., Guanidinium Cations Pair with Positively Charged Arginine Side Chains in Water. *J. Phys. Chem. Lett.* **2011,** *2* (12), 1387-1389.

132. Neese, F., The ORCA program system. *Wiley Interdisciplinary Reviews: Computational Molecular Science* **2012,** *2* (1), 73-78.

133. Chai, J.-D.; Head-Gordon, M., Systematic optimization of long-range corrected hybrid density functionals. *The Journal of Chemical Physics* **2008,** *128* (8), 084106.

134. Weigend, F.; Ahlrichs, R., Balanced basis sets of split valence, triple zeta valence and quadruple zeta valence quality for H to Rn: Design and assessment of accuracy. *Physical Chemistry Chemical Physics* **2005,** *7* (18), 3297-3305.

135. Neese, F.; Wennmohs, F.; Hansen, A.; Becker, U., Efficient, approximate and parallel Hartree–Fock and hybrid DFT calculations. A 'chain-of-spheres' algorithm for the Hartree–Fock exchange. *Chemical Physics* **2009,** *356* (1), 98-109.

136. Kruse, H.; Grimme, S., A geometrical correction for the inter- and intra-molecular basis set superposition error in Hartree-Fock and density functional theory calculations for large systems. *The Journal of Chemical Physics* **2012,** *136* (15), 154101.

137. Humphrey, W.; Dalke, A.; Schulten, K., VMD: Visual molecular dynamics. *Journal of Molecular Graphics* **1996,** *14* (1), 33-38.

138. Contreras-García, J.; Johnson, E. R.; Keinan, S.; Chaudret, R.; Piquemal, J.-P.; Beratan, D. N.; Yang, W., NCIPLOT: A Program for Plotting Noncovalent Interaction Regions. *Journal of Chemical Theory and Computation* **2011,** *7* (3), 625-632.

139. Kim, D.; Wagner, N.; Wooding, K.; Clemmer, D. E.; Russell, D. H., Ions from Solution to the Gas Phase: A Molecular Dynamics Simulation of the Structural Evolution of Substance P during Desolvation of Charged Nanodroplets Generated by Electrospray Ionization. *J. Am. Chem. Soc.* **2017,** *139* (8), 2981-2988.

140. Gao, B.; Wyttenbach, T.; Bowers, M. T., Protonated Arginine and Protonated Lysine: Hydration and Its Effect on the Stability of Salt-Bridge Structures. *The Journal of Physical Chemistry B* **2009,** *113* (29), 9995-10000.

141. Vanzi, F.; Madan, B.; Sharp, K., Effect of the Protein Denaturants Urea and Guanidinium on Water Structure: A Structural and Thermodynamic Study. *J. Am. Chem. Soc.* **1998,** *120* (41), 10748-10753.

142. Heiles, S.; Cooper, R. J.; DiTucci, M. J.; Williams, E. R., Hydration of guanidinium depends on its local environment. *Chemical Science* **2015,** *6* (6), 3420-3429.

143. Mason, P. E.; Neilson, G. W.; Enderby, J. E.; Saboungi, M.-L.; Dempsey, C. E.; MacKerell, A. D.; Brady, J. W., The Structure of Aqueous Guanidinium Chloride Solutions. *J. Am. Chem. Soc.* **2004,** *126* (37), 11462-11470.

144. Wagner, N. D.; Kim, D.; Russell, D. H., Increasing Ubiquitin Ion Resistance to Unfolding in the Gas Phase Using Chloride Adduction: Preserving More "Native-Like" Conformations Despite Collisional Activation. *Anal. Chem.* **2016,** *88* (11), 5934-5940.

145. Brugé, F.; Bernasconi, M.; Parrinello, M., Ab Initio Simulation of Rotational Dynamics of Solvated Ammonium Ion in Water. *Journal of the American Chemical Society* **1999,** *121* (47), 10883-10888.

146. Parui, S.; Jana, B., Factors Promoting the Formation of Clathrate-Like Ordering of Water in Biomolecular Structure at Ambient Temperature and Pressure. *J. Phys. Chem. B* **2019,** *123* (4), 811-824.

147. de Grotthuss, C. J. T., Sur la décomposition de l'eau et des corps qu'elle tient en dissolution à l'aide de l'électricité galvanique. *Ann. Chim.* **1806,** *LVIII*, 54–74.

148. Campbell, J. L.; Yang, A. M.-C.; Melo, L. R.; Hopkins, W. S., Studying Gas-Phase Interconversion of Tautomers Using Differential Mobility Spectrometry. *J. Am. Soc. Mass Spectrom.* **2016,** *27* (7), 1277-1284.

149. May, J. C.; Morris, C. B.; McLean, J. A., Ion Mobility Collision Cross Section Compendium. *Anal. Chem.* **2017,** *89* (2), 1032-1044.

150. Mason, E. A.; Schamp, H. W., Mobility of gaseous lons in weak electric fields. *Annals of Physics* **1958,** *4* (3), 233-270.

151. Matlab/Octave Peak Fitters. 2019. A Pragmatic Introduction to Signal Processing. https://terpconnect.umd.edu/~toh/spectrum/InteractivePeakFitter.htm.

152. Fenn, L. S.; Kliman, M.; Mahsut, A.; Zhao, S. R.; McLean, J. A., Characterizing ion mobility-mass spectrometry conformation space for the analysis of complex biological samples. *Analytical and Bioanalytical Chemistry* **2009,** *394* (1), 235-244.

153. Bleiholder, C.; Wyttenbach, T.; Bowers, M. T., A novel projection approximation algorithm for the fast and accurate computation of molecular collision cross sections (I). Method. *Int. J. Mass Spectrom.* **2011,** *308* (1), 1-10.

154. EURACHEM/CITAC. 2012. QUAM: 2012.P1: Quantifying Uncertainty in Analytical Measurement. https://www.eurachem.org/images/stories/Guides/pdf/QUAM2012_P1.pdf.

155. Servage, K. A.; Silveira, J. A.; Fort, K. L.; Russell, D. H., Cryogenic Ion Mobility-Mass Spectrometry: Tracking Ion Structure from Solution to the Gas Phase. *Acc. Chem. Res.* **2016,** *49* (7), 1421-1428.

156. Seo, J.; Warnke, S.; Gewinner, S.; Schöllkopf, W.; Bowers, M. T.; Pagel, K.; von Helden, G., The impact of environment and resonance effects on the site of protonation of aminobenzoic acid derivatives. *Physical Chemistry Chemical Physics* **2016,** *18* (36), 25474-25482.

157. Asbury, G. R.; Hill, H. H., Using Different Drift Gases To Change Separation Factors (α) in Ion Mobility Spectrometry. *Anal. Chem.* **2000,** *72* (3), 580-584.

158. Matz, L. M.; Hill, H. H.; Beegle, L. W.; Kanik, I., Investigation of drift gas selectivity in high resolution ion mobility spectrometry with mass spectrometry detection. *J. Am. Soc. Mass Spectrom.* **2002,** *13* (4), 300-307.

159. Jurneczko, E.; Kalapothakis, J.; Campuzano, I. D. G.; Morris, M.; Barran, P. E., Effects of Drift Gas on Collision Cross Sections of a Protein Standard in Linear Drift Tube and Traveling Wave Ion Mobility Mass Spectrometry. *Anal. Chem.* **2012,** *84* (20), 8524-8531.

160. Ruotolo, B. T.; McLean, J. A.; Gillig, K. J.; Russell, D. H., Peak capacity of ion mobility mass spectrometry: the utility of varying drift gas polarizability for the separation of tryptic peptides. *J. Mass Spectrom.* **2004,** *39* (4), 361-367.

161. Rusyniak, M.; Ibrahim, Y.; Alsharaeh, E.; Meot, N.; El-Shall, M. S., Mass-Selected Ion Mobility Studies of the Isomerization of the Benzene Radical Cation and Binding Energy of the Benzene Dimer Cation. Separation of Isomeric Ions by Dimer Formation. *J. Phys. Chem. A* **2003,** *107* (38), 7656-7666.

162. Verbeck, G. F.; Gillig, K. J.; Russell, D. H., Variable-temperature ion mobility time-of-flight mass spectrometry studies of electronic isomers of Kr2+ and CH3OH*+ radical cations. *Eur. J. Mass Spectrom.* **2003,** *9* (6), 579-587.

163. Ujma, J.; Giles, K.; Morris, M.; Barran, P. E., New High Resolution Ion Mobility Mass Spectrometer Capable of Measurements of Collision Cross Sections from 150 to 520 K. *Anal. Chem.* **2016,** *88* (19), 9469-9478.

164. Karpas, Z.; Berant, Z.; Stimac, R. M., An ion mobility spectrometry/mass spectrometry (IMS/MS) study of the site of protonation in anilines. *Structural Chemistry* **1990,** *1* (2), 201-204.

165. Xiao, C.; Pérez, L. M.; Russell, D. H., Effects of charge states, charge sites and side chain interactions on conformational preferences of a series of model peptide ions. *Analyst* **2015,** *140* (20), 6933-6944.

166. Breuker, K.; McLafferty, F. W., Stepwise evolution of protein native structure with electrospray into the gas phase, 10−12 to 102 s. *Proc. Natl. Acad. Sci. U.S.A.* **2008,** *105* (47), 18145-18152.

167. Chang, T. M.; Cooper, R. J.; Williams, E. R., Locating Protonated Amines in Clathrates. *J. Am. Chem. Soc.* **2013,** *135* (39), 14821-14830.

168. Fedotova, M. V.; Kruchinin, S. E., Hydration of para-aminobenzoic acid (PABA) and its anion—The view from statistical mechanics. *Journal of Molecular Liquids* **2013,** *186*, 90-97.

169. Brooks, B. R.; Brooks III, C. L.; Mackerell Jr., A. D.; Nilsson, L.; Petrella, R. J.; Roux, B.; Won, Y.; Archontis, G.; Bartels, C.; Boresch, S.; Caflisch, A.; Caves, L.; Cui, Q.; Dinner, A. R.; Feig, M.; Fischer, S.; Gao, J.; Hodoscek, M.; Im, W.; Kuczera, K.; Lazaridis, T.; Ma, J.; Ovchinnikov, V.; Paci, E.; Pastor, R. W.; Post, C. B.; Pu, J. Z.; Schaefer, M.; Tidor, B.; Venable, R. M.; Woodcock, H. L.; Wu, X.; Yang, W.; York, D. M.; Karplus, M., CHARMM: The biomolecular simulation program. *Journal of Computational Chemistry* **2009,** *30* (10), 1545-1614.

170. Dupradeau, F.-Y.; Pigache, A.; Zaffran, T.; Savineau, C.; Lelong, R.; Grivel, N.; Lelong, D.; Rosanski, W.; Cieplak, P., The R.E.D. tools: advances in RESP and ESP charge derivation and force field library building. *Phys. Chem. Chem. Phys.* **2010,** *12*

(Copyright (C) 2013 American Chemical Society (ACS). All Rights Reserved.), 7821-7839.

171. Case, D. A.; Cheatham III, T. E.; Darden, T.; Gohlke, H.; Luo, R.; Merz Jr., K. M.; Onufriev, A.; Simmerling, C.; Wang, B.; Woods, R. J., The Amber biomolecular simulation programs. *Journal of Computational Chemistry* **2005,** *26* (16), 1668-1688.

172. Abraham, M. J.; Murtola, T.; Schulz, R.; Páll, S.; Smith, J. C.; Hess, B.; Lindahl, E., GROMACS: High performance molecular simulations through multi-level parallelism from laptops to supercomputers. *SoftwareX* **2015,** *1-2*, 19-25.

173. Servage, K. A.; Silveira, J. A.; Fort, K. L.; Russell, D. H., From Solution to Gas Phase: The Implications of Intramolecular Interactions on the Evaporative Dynamics of Substance P During Electrospray Ionization. *J. Phys. Chem. B* **2015,** *119* (13), 4693-4698.

174. Sterner, J. L.; Johnston, M. V.; Nicol, G. R.; Ridge, D. P., Apparent proton affinities of highly charged peptide ions. *J. Am. Soc. Mass Spectrom.* **1999,** *10* (6), 483-491.

175. Loo, J. A., Studying noncovalent protein complexes by electrospray ionization mass spectrometry. *Mass Spectrometry Reviews* **1997,** *16* (1), 1-23.

176. Davis, A. L.; Liu, W.; Siems, W. F.; Clowers, B. H., Correlation ion mobility spectrometry. *Analyst* **2017,** *142* (2), 292-301.

177. Jerri, A. J., The Shannon sampling theorem—Its various extensions and applications: A tutorial review. *Proceedings of the IEEE* **1977,** *65* (11), 1565-1596.

178. Hebert, M. J.; Russell, D. H., Tracking the Structural Evolution of 4-Aminobenzoic Acid in the Transition from Solution to the Gas Phase. *J. Phys. Chem. B* **2020,** *124* (11), 2081-2087.

179. Hong, J.; Xiong, S., TMAO-Protein Preferential Interaction Profile Determines TMAO's Conditional In Vivo Compatibility. *Biophys. J.* **2016,** *111* (9), 1866-1875.

180. Yancey, P. H.; Somero, G. N., Counteraction of urea destabilization of protein structure by methylamine osmoregulatory compounds of elasmobranch fishes. *Biochemical Journal* **1979,** *183* (2), 317-323.

181. Canchi, D. R.; Jayasimha, P.; Rau, D. C.; Makhatadze, G. I.; Garcia, A. E., Molecular Mechanism for the Preferential Exclusion of TMAO from Protein Surfaces. *J. Phys. Chem. B* **2012,** *116* (40), 12095-12104.

182. Meersman, F.; Bowron, D.; Soper, A. K.; Koch, M. H. J., Counteraction of Urea by Trimethylamine N-Oxide Is Due to Direct Interaction. *Biophys. J.* **2009,** *97* (9), 2559-2566.

183. Frank, H. S.; Franks, F., Structural Approach to the Solvent Power of Water for Hydrocarbons; Urea as a Structure Breaker. *J. Chem. Phys.* **1968,** *48* (10), 4746-4757.

184. Bennion, B. J.; Daggett, V., Counteraction of urea-induced protein denaturation by trimethylamine N-oxide: A chemical chaperone at atomic resolution. *Proceedings of the National Academy of Sciences of the United States of America* **2004,** *101* (17), 6433-6438.

185. Dong, S.; Wagner, N. D.; Russell, D. H., Collision-Induced Unfolding of Partially Metalated Metallothionein-2A: Tracking Unfolding Reactions of Gas-Phase Ions. *Anal. Chem.* **2018,** *90* (20), 11856-11862.

186. Chen, S.-H.; Russell, W. K.; Russell, D. H., Combining Chemical Labeling, Bottom-Up and Top-Down Ion-Mobility Mass Spectrometry To Identify Metal-Binding Sites of Partially Metalated Metallothionein. *Anal. Chem.* **2013,** *85* (6), 3229-3237.

187. Chen, S.-H.; Russell, D. H., Reaction of Human Cd7metallothionein and N-Ethylmaleimide: Kinetic and Structural Insights from Electrospray Ionization Mass Spectrometry. *Biochemistry* **2015,** *54* (39), 6021-6028.

188. Chen, S.-H.; Russell, D. H., How Closely Related Are Conformations of Protein Ions Sampled by IM-MS to Native Solution Structures? *J. Am. Soc. Mass Spectrom.* **2015,** *26* (9), 1433-1443.

189. Ganguly, P.; Shea, J.-E., Distinct and Nonadditive Effects of Urea and Guanidinium Chloride on Peptide Solvation. *J. Phys. Chem. Lett.* **2019,** *10* (23), 7406-7413.

190. Iwase, H.; Kobayashi, M.; Nakajima, M.; Takatori, T., The ratio of insulin to C-peptide can be used to make a forensic diagnosis of exogenous insulin overdosage. *Forensic Science International* **2001,** *115* (1), 123-127.

191. Weiss, M. A.; Hua, Q. X.; Lynch, C. S.; Frank, B. H.; Shoelson, S. E., Heteronuclear 2D NMR studies of an engineered insulin monomer: assignment and characterization of the receptor-binding surface by selective deuterium and carbon-13 labeling with application to protein design. *Biochemistry* **1991,** *30* (30), 7373-7389.

192. Bocian, W.; Sitkowski, J.; Bednarek, E.; Tarnowska, A.; Kawęcki, R.; Kozerski, L., Structure of human insulin monomer in water/acetonitrile solution. *Journal of Biomolecular NMR* **2008,** *40* (1), 55-64.

193. Ganim, Z.; Jones, K. C.; Tokmakoff, A., Insulin dimer dissociation and unfolding revealed by amide I two-dimensional infrared spectroscopy. *Physical Chemistry Chemical Physics* **2010,** *12* (14), 3579-3588.

194. Millican, R. L.; Brems, D. N., Equilibrium Intermediates in the Denaturation of Human Insulin and Two Monomeric Insulin Analogs. *Biochemistry* **1994,** *33* (5), 1116-1124.

195. Nettleton, E. J.; Tito, P.; Sunde, M.; Bouchard, M.; Dobson, C. M.; Robinson, C. V., Characterization of the Oligomeric States of Insulin in Self-Assembly and Amyloid Fibril Formation by Mass Spectrometry. *Biophys. J.* **2000,** *79* (2), 1053-1065.

196. Gillig, K. J., Gas-phase protein conformation/multimer ion formation by electrospray ion mobility-mass spectrometry: bovine insulin and ubiquitin. *Philosophical Transactions of the Royal Society A: Mathematical, Physical and Engineering Sciences* **2016,** *374* (2079).

197. Chothia, C.; Janin, J., Principles of protein-protein recognition. *Nature* **1975,** *256* (5520), 705-708.

198. Mauri, S.; Weidner, T.; Arnolds, H., The structure of insulin at the air/water interface: monomers or dimers? *Physical Chemistry Chemical Physics* **2014,** *16* (48), 26722-26724.

199. Mukherjee, S.; Mondal, S.; Deshmukh, A. A.; Gopal, B.; Bagchi, B., What Gives an Insulin Hexamer Its Unique Shape and Stability? Role of Ten Confined Water Molecules. *J. Phys. Chem. B* **2018,** *122* (5), 1631-1637.

200. Tang, Y.-C.; Chang, H.-C.; Roeben, A.; Wischnewski, D.; Wischnewski, N.; Kerner, M. J.; Hartl, F. U.; Hayer-Hartl, M., Structural Features of the GroEL-GroES Nano-Cage Required for Rapid Folding of Encapsulated Protein. *Cell* **2006,** *125* (5), 903-914.

201. England, J. L.; Lucent, D.; Pande, V. S., A Role for Confined Water in Chaperonin Function. *J. Am. Chem. Soc.* **2008,** *130* (36), 11838-11839.

202. Piana, S.; Shaw, D. E., Atomic-Level Description of Protein Folding inside the GroEL Cavity. *J. Phys. Chem. B* **2018,** *122* (49), 11440-11449.

203. Jurneczko, E.; Barran, P. E., How useful is ion mobility mass spectrometry for structural biology? The relationship between protein crystal structures and their collision cross sections in the gas phase. *Analyst* **2011,** *136* (1), 20-28.

204. Rolland, A. D.; Prell, J. S., Computational insights into compaction of gas-phase protein and protein complex ions in native ion mobility-mass spectrometry. *TrAC Trends in Analytical Chemistry* **2019,** *116*, 282-291.